TESI DI DOTTORATO

UNIVERSITÀ DEGLI STUDI DI CAGLIARI

DIPARTIMENTO DI INGEGNERIA ELETTRICA ED ELETTRONICA

SCUOLA DI DOTTORATO IN INGEGNERIA DELL'INFORMAZIONE

DOTTORATO DI RICERCA IN INGEGNERIA ELETTRONICA E INFORMATICA

CICLO XIX – SSD: ING-INF/02 CAMPI ELETTROMAGNETICI

OIL SPILL DETECTION BY MEANS OF SYNTHETIC APERTURE RADAR

ATTILIO GAMBARDELLA

Coordinatore del Corso
Prof. Alessandro Giua

Tutore: Prof. Giuseppe Mazzarella
Co-Tutore: Prof. Maurizio Migliaccio

Marzo 2007

Acknowledgements

I wish to thank many people who helped me during my PhD research.

First of all, I am grateful to my tutors Prof. Giuseppe Mazzarella and Prof. Maurizio Migliaccio who have supported me for all the time of my PhD.

Furthermore, I whish to say thanks to all my colleagues from DIEE at Università di Cagliari and from DiT at Università di Napoli Parthenope for their friendship, support and help.

Special thanks are due to Giorgio Giacinto from DIEE and Andrea Montali for the fruitful collaboration. Words of thanks go to Prof. Sebastiano Seatzu and Daniela Theis from DMI at Università di Cagliari for the suggestions and the stimulating discussions.

Thanks are also due to the European Space Agency (ESA), the NASA's Jet Propulsion Laboratory (JPL), the Deutsche Forschungsanstalt fur Luft- and Raumfahrt e. V. (DLR), the Joint Research Centre (JRC), the Telaer consortium and Telespazio S.p.A. for providing the SAR data used in the studies.

Finally, I have to thank to my family and to Raffaella: without their support all this would have never been possible.

Index

Introduction

Sea oil pollution can be originated by major disasters, such as oil-tankers sinking, but also chronic, and more frequent, smaller spills associated to routine tanker operations and marine traffic in general (e.g., tank cleaning or bilge pumping), offshore oil extraction, and damaged underwater pipelines (Delilah, 2002). Moreover, a large quantity of oil comes from civil and industrial discharges, and from natural hydrocarbon seeps (Delilah, 2002). Oil pollution causes marine ecological disasters that damage the quality and productivity of the marine environment, and produce severe financial consequences associated both to clear-up operations, and to the decrease of coastal tourism and the related economy (Fukuyama *et al.*, 1998). In fact, the long-term effects of this chronic pollution are undoubtedly more harmful to the coastal environment than any single, large-scale accident (Fukuyama *et al.*, 1998). Potential damages, and the difficulty to restore these habitats and biological natural resources, stimulated a public awareness in order to protect sea trustee (Delilah, 2002; Fukuyama *et al.*, 1998). Therefore, stricter national and international laws have been established.

Remote sensing can be of great help in oil spill observation (Brekke and Solberg, 2005; Delilah, 2002; Girard-Arduin *et al.*, 2003; Migliaccio and Tranfaglia, 2004). In fact, the use of Earth Observation (EO) data from satellite in conjunction with standard observation techniques is an efficient tool to ensure synoptic oil spill monitoring. In particular, satellite-based EO systems provide an effective way of monitoring chronic sea oil pollution (Brekke and Solberg, 2005). Two of the major advantages of using EO data are: their moderate cost if compared to aircraft monitoring, and the large area coverage per satellite pass. Among the many different sensors, Synthetic Aperture Radar (SAR) has been shown to be the most useful for the detection of sea oil pollution (Brekke and Solberg, 2005; Delilah, 2002; Girard-Arduin *et al.*, 2003; Migliaccio and Tranfaglia, 2004). Due to its ability to uniquely provide high resolution information about the observed scene it is a useful tool for oceanographic applications (Jackson and Apel, 2004). In fact, SAR is an active, coherent, band-limited microwave high-resolution remote sensing sensor that can provide valuable measurements both during daylight, and during the night. In addition SAR measurements are almost independent from atmospheric conditions (Jackson and Apel, 2004). Thus SAR data make it possible to discover illegal discharges that are made most frequently during the night. In addition, SAR data allows surveying storm areas, where the risk of accidents is obviously increased. The spatial resolution of space-borne SARs typically ranges between a few meters and more than hundred meters. Accordingly, the spatial coverage varies between approximately 100x100 km up to 500x500 km (Jackson and Apel, 2004). Unfortunately, as any remote sensing technique, the observables, i.e. the measurements accomplished by the sensor, are not simply related to the geophysical parameters of interest. This is due to two major facts: the presence of noise and the nature of the physical interactions between the electromagnetic wave and the scene that is generally non-linear and partly unknown. Therefore, the main effort and the overall cost are determined by the ability to infer the geophysical parameters of interest.

Physically, the phenomenon allowing oil spill detection from SAR measurements can be described as follows. Radar backscatter is due to the roughness of the ocean surface, where roughness is determined by the directional spectrum of the waves sampled at of Bragg wavelength (Espedal and Wahl, 1999). In the case of SAR sensors, typical waves are gravity and capillary waves with wavelengths of few centimeters. Physically oil spill detection is possible since oil slicks damp such short waves (Delilah, 2002; Brekke and Solberg, 2005).

As a consequence, an oil spill appears as a dark patch in SAR images (Brekke and Solberg, 2005). Unfortunately, several natural and atmospheric phenomena produce dark areas in SAR images similar to oil spills. These dark areas are usually referred to as look-alikes, whose presence makes the detection of oil spills a challenging task (Delilah, 2002). Phenomena giving rise to look-alikes may include biogenic films, areas of low wind ($<3 ms^{-1}$), areas of wind-shadow near coasts, rain cells, zones of upwelling, internal waves and oceanic or atmospheric fronts (Espedal and Wahl, 1999). Nevertheless, the contrast between a spill and the surrounding water depends both on the amount and type of oil, and on environmental factors such as wind speed, wave height, and current (Espedal and Wahl, 1999). Environmental factors also determine spreading, drift and weathering of spilt oil and should be taken into account (Delilah, 2002). Moreover, there is also a maximum wind speed above which oil films become undetectable. At high wind speed the damping effect can disappear in the background noise of wind-generated waves and at because of the oil is washed down by breaking waves (Espedal and Wahl, 1999). Depending on the type of the oil and the thickness of the oil film, oil films become undetectable at wind speeds between 10 ms^{-1} and 14 ms^{-1} (Brekke and Solberg, 2005).

Following the above discussion, oil spill detection from SAR images not only requires the detection of dark patches in the image, but also post-processing techniques aimed at discriminating oil spills from look-alikes. Usually, oil spill detection is framed into three fundamental phases (see Fig. I.1): dark patch detection, features extraction, and oil spill/look-alike classification (Brekke and Solberg, 2005). Moreover, in order to enhance the ability to distinguish oil spills and look-alikes it is nowadays recognized the usefulness of additional external data, e.g. the local wind field (Girard-Arduin *et al.*, 2003; Migliaccio and Tranfaglia, 2004).

Dark patch detection algorithms are based on filtering techniques, which require the use of a suitable threshold (Brekke and Solberg, 2005). The value of the threshold is usually estimated using damping physical models such as the Marangoni theory (Gade *et al.*, 1998), or it is empirically selected. However, the choice of the value of the threshold typically does not take into account the environmental sea conditions (Brekke and Solberg, 2005). Recently, a new approach has been proposed to incorporate the local wind speed into the damping model (Migliaccio *et al.*, 2005).

While dark patch detection algorithms yield the patch location and the segmentation of suspected polluted areas, feature extraction is necessary to perform slick classification aimed to distinguish oil spills from look-alikes. The vast majority of features are based on geometrical properties, as well as on radiometric measures and textures (Migliaccio and Tranfaglia, 2004). A detailed state-of-the-art of oil spill detection from SAR images is reported in (Brekke and Solberg, 2005; Girard-Arduin *et al.*, 2003; Migliaccio and Tranfaglia, 2004).

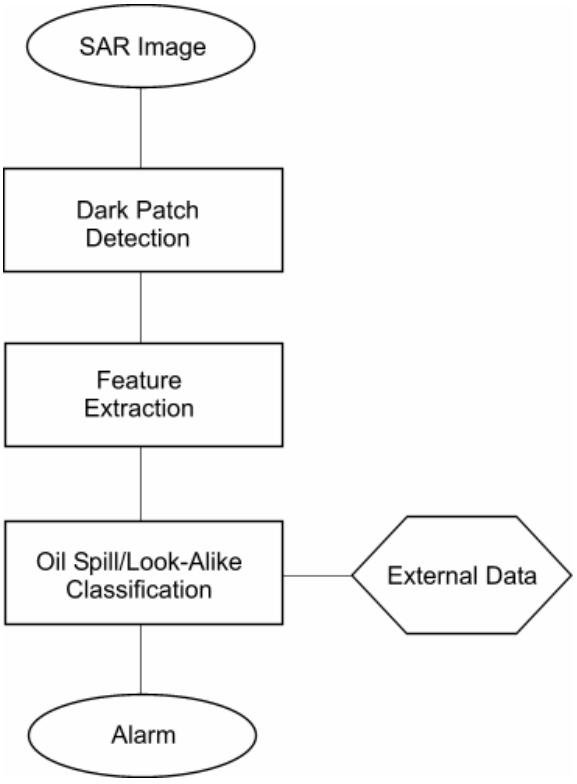

Fig. I.1: Oil Spill detection scheme.

As a matter of fact, oil spills detection over SAR images is a very complicated task and it is nowadays on of the main research topic of the scientists working on remote sensing. In this thesis work all the issues related to the problem have been taken in care. The first aspect to be considered is the capability of increasing the accuracy of the detection methods, e.g. a better threshold value selection procedure for the filter-based dark patch detection algorithms. This could be done by means of an enhancement of the understanding of the physical process

governing the radar backscatter. This is possible combining an electromagnetic backscattering model and a damping model which adequately describes the behavior of the radar backscatter from sea surface with and without oil films. In this thesis work, to describe the scattering of electromagnetic waves by random rough surfaces and the observable damping, reference is made on two classical analytical approaches, namely the Kirchhoff approximation (KA) and the small perturbation method (SPM) (Beckmann and Spizzichino, 1963; Tsang *et al.*, 1985; Ulaby *et al.*, 1982), and on a new damping model, presented in (Migliaccio *et al.*, 2005). These models have been considered as reference for all the studies presented hereafter.

A second issue concerns how a dynamic scene, such as sea surface, is imaged by SAR system. In fact, according to Bragg theory only sea waves whose wavelengths are the same order of the incidence electromagnetic one are "seen" by SAR, but these latter are "modulated" by the longer ones (Brüning *et al.*, 1990). Hence, this issue is considerably more complex than the imaging of a stationary scene. For these reasons and to shed light in physical aspects governing the SAR surface waves imaging a "SAR sea surface waves simulator", based on the velocity bunching VB theory (Alpers *et al.*, 1981), has been developed and presented (Nunziata *el at.*, sub).

Another aspect to be considered is how to deal with the speckle noise which affect SAR images. Typically, speckle can be reduced by a processing technique known as multilook (Franceschetti and Lanari, 1999). On one side, multilook enhances interpretability but, on the other side, this generates SAR images at coarser spatial resolution and this hamper small size oil spill detection. In this thesis a speckle model for marine Single-Look Complex SAR images is presented (Migliaccio *et al.,* sub.). The approach is based on the use of the three parameters of the generalized *K* probability density function and is physically based since the generalized *K* ensures a continuous and physically consistent transition among different scattering scenarios. Moreover this speckle model allows full-resolution SAR images and improving the oil spill detection capability.

Attention has been paid also on polarimetric SAR data. Oil spill detection by means of polarimetric SAR data is a quite unexplored field and only few studies have been conducted in last years. Nevertheless, there is a general consensus that radar polarimetry is able to provide additional information for environmental remote sensing applications. In this thesis work two studies on sea oil spills observation by means of polarimetric SAR data are presented. In one the oil spill detection is based on the combined use of a polarimetric

Constant False Alarm Rate filter to detect dark patches and the use of the Target Decomposition theorem to distinguish oil spills and look-alikes (Migliaccio *et al.*, 2007). In the second study, the capability of the phase difference standard deviation value ($\sigma_{\varphi c}$) to distinguish among different dark features over marine polarimetric SAR images is investigated (Gambardella *et al.*, 2007).

A related issue, that has been studied within this thesis work, is the definition of a mathematical objective framework of the oil spill detection problem. Such a fundamental mathematical problem has looked for the objective definition of the feature space and of the nature of the classification problem. In detail, a selection algorithm to objectively select the most effective subset of features and a formulation of the problem as a one-class classification problem are presented (Gambardella *et al.*, sub). All the studies reported in the literature are based on a two-class classification methodology, where examples of the two classes, i.e. oil spills and look-alikes, have to be provided to train the classification model. One-class approaches aim to model the class for which reliable examples can be provided, e.g. the oil spill class.

The thesis is organized in five chapters. In Chapter 1 the electromagnetic scattering models and the damping model, considered in the subsequent studies, are presented. In Chapter 2 SAR sea surface waves simulator is introduced. In Chapter 3 the speckle model for marine Single-Look Complex SAR images is described. Successively, in Chapter 4 the studies on SAR polarimetry are presented and in Chapter 5 the feature selection procedure and the one-class pattern classification approach are described. Final comments are now in order.

In order to make reading of this thesis easier, a short description of symbols used in Chapters 1-5 is collected in Table of Symbols.

Finally, it must be noted that a great part of the material, presented from a systematic and unitary point of view in this thesis, has been already published (or is on going) by the author in the last three years, (see Contributes Section).

References

Alpers W., D. Ross, and C. Rufenach, "On the Detectability of Ocean Surface Waves by Real and Synthetic Aperture Radar," *J. of Geophysical Research,* vol. 86, no. C7, pp. 6481-6498, 1891.

Beckmann, P. and A.Spizzichino, *The Scattering of Electromagnetic Waves from Rough Surfaces*, Norwood, MA: Artech House, 1963.

Brekke C., and A. H. S. Solberg, "Oil Spill Detection by Satellite Remote Sensing," *Remote Sens. Environ.*, no. 95, pp. 1-13, 2005.

Brüning C., W. Alpers, and K. Hasselmann, "Monte-Carlo Simulation Studies of the Nonlinear Imaging of a Two-dimensional Surface Wave Field by a Synthetic Aperture Radar," *Int. J. of Remote Sensing,* vol. 11, no. 10, pp. 1695-1727, 1990.

Delilah H. A., "Marine Oil Pollution: Technologies and Technologies for Detection and Early Warning," *European Commission JRC report*, EUR 20231 EN, 2002.

Espedal H. A. and T. Wahl, "Satellite SAR Oil Spill Detection Using Wind History Information," *Int. J. Remote Sens.*, vol. 20, no.1, pp. 49-65, Jan. 1999.

Franceschetti G. and R. Lanari, *Synthetic Aperture Radar Processing*. Boca Raton, FL: CRC Press, 1999.

Fukuyama K., G. Shigenaka, and G. R. Van Blaricom, "Oil Spill Impacts and the Biological Basis for Response Guidance: an Applied Synthesis of Research on Tree Subartic Intertidal Communities," *NOAA Tech. Memorandum*, NOS ORCA 125, Seattle, Washington, Mar. 1998.

Gade M., W. Alpers, H. Huhnerfuss, V. R. Wismann, and P. A. Lange, "On the Reduction of the Radar Backscatter by Oceanic Surface Films: Scatterometer Measurements and Their Theoretical Interpretation," *Remote Sens. Environ.*, vol. 66, no. 1, pp. 52-70, Oct.1998.

Gambardella A., F. Nunziata, M. Migliaccio, "Oil Spill Observation by means of Co-polar Phase Difference", *Proc. of PolINSAR2007 Workshop*, ESA-ESRIN, Frascati, Italy, January 22-26, 2007.

Gambardella A., G. Giacinto, M. Migliaccio, A. Montali, "SAR Oil Spill Detection: Feature Analysis and One-Class Pattern Classification," *IEEE Trans. Geosci. Remote Sens.*, submitted for publication.

Girard-Ardhuin F., G. Mercier, and R. Garello, "Oil Slick Detection by SAR Imagery: Potential and Limitation," in *Proc. Ocean 2003*, San Diego, USA, pp. 164-169, Sept. 2003.

Jackson C.R. and J.R. Apel Ed., *Synthetic Aperture Radar Marine Users Manual*. NOAA, Washington, DC, 2004.

Migliaccio M. and M. Tranfaglia, "Oil Spill Observation by SAR: a Review," in *Proc. USA-Baltic International Symposium "Advances in Marine Environ. Res. Monitoring & Technologies"*, Klaipeda, Lithuania, 15-17 June 2004.

Migliaccio M., M. Tranfaglia, and S.A. Ermakov, "A Physical Approach for the Observation of Oil Spills in SAR Images*," IEEE J. Oceanic Engineering*, vol. 30, no. 3, pp. 495-507, July 2005.

Migliaccio M., G. Ferrara, A. Gambardella, F. Nunziata, A. Sorrentino, "Detection of Dark Areas and Strong Scatterers in Marine SLC SAR Images", *IEEE J. Oceanic Engineering*, submitted for publication.

Migliaccio M., A. Gambardella, M. Tranfaglia, "SAR Polarimetry to Observe Oil Spills," *IEEE Trans. Geosci. Remote Sens.*, vol.43 , no.2 , pp 506-511 , 2007.

Nunziata F., A. Gambardella, M. Migliaccio, "An Educational SAR Sea Surface Waves Simulator", *Int. J. Remote Sens.*, submitted for publication.

Tsang, L., J.A.Kong and R.T.Shin, *Theory of Microwave Remote Sensing*, New York, NY: John Wuey,1985.

Ulaby, F.T., R.K.Moore, and A.K.Fung, *Microwave Remote Sensing, vol. II*, Reading, MA: Addison-Wesley, 1982.

Chapter 1: Electromagnetic Models

Two classical analytical approaches have been considered to describe the scattering of electromagnetic waves by random rough surfaces. In the Kirchhoff approximation (KA), the field at any point of the surface are approximated by the fields that would be present on the tangent plane at that point. Thus the tangent plane approximation requires a large radius of curvature relative to the incident wavelength at every point on the surface. In the small perturbation method (SPM) the surface variations are assumed to be much smaller than the incident wavelength and the slopes of the rough surface are relatively small. Finally, a model for the observable damping, based on the SPM and on the oil damping theory, is presented.

1.1 Introduction

For a correct interpretation of the change of the radar backscatter from sea surface with and without oil films it is necessary to take into account scattering from a rough surface with a broad spectrum of roughness.

The problem of electromagnetic wave scattering from a randomly rough surface has been widely studied because of its great relevance in the fields of telecommunications and remote sensing. In the last decades, several approaches to the solution of this problem have been proposed and developed. Among them, the in this chapter, attention will be focused on the Kirchhoff approach (KA) and the Small Perturbation Method (SPM) (Beckmann and Spizzichino, 1963; Tsang *et al.*, 1985; Ulaby *et al.*, 1982). These approaches are based on different approximations and exhibit different ranges of validity (Ulaby *et al.*, 1982). In all cases, the surface is described by a stationary stochastic two-dimensional process, with given probability density function (pdf) and correlation function. Accordingly, the surface can be characterized by few parameters such as its height standard deviation and its correlation length.

Successively, a model for observable damping, based on the SPM and on the oil damping theory, is presented (Migliaccio *et al.*, 2005). The enhanced damping model takes into account oil visco-elastic properties and wind speed (Migliaccio *et al.*, 2005).

1.2 Statistical description of a random rough surface

The scatterer rough surface $z(x,y)$ can be described by a Gaussian stationary random process with zero mean and variance σ^2 with pdf:

$$\begin{aligned} p(z) &= \frac{1}{\sqrt{2\pi}\sigma}\exp\left(-\frac{z^2}{2\sigma^2}\right) \quad , \\ p(z,z') &= \frac{1}{2\pi\sigma^2\sqrt{1-C^2}}\exp\left(-\frac{z^2-2Czz'+z'^2}{2\sigma^2(1-C^2)}\right) \quad , \end{aligned} \tag{1.1}$$

where $z = z(x, y)$, $z' = z(x', y')$ and $C = C(x - x', y - y')$ is the surface autocorrelation function. If the surface is isotropic then $C = C(\tau)$, with $\tau = \sqrt{(x - x')^2 + (y - y')^2}$.

It is useful to remind the characteristic function of the random process z which is the Fourier transform of the pdf

$$\langle \exp(-jvz) \rangle = \int_{-\infty}^{+\infty} p(z) \exp(-jvz) dz = \exp\left(-\frac{1}{2} \sigma^2 v^2 \right) \quad . \tag{1.2}$$

An alternative description of a randomly rough surface is obtained by the power spectrum $\boldsymbol{S}(\kappa_x, \kappa_y)$ (or power spectral density function) which, for a stationary random process, is the Fourier transform of the autocorrelation function:

$$\boldsymbol{S}(\kappa_x, \kappa_y) = \iint \sigma^2 C(\tau_x, \tau_y) \exp(-j\kappa_x \tau_x - j\kappa_y \tau_y) d\tau_x d\tau_y \quad , \tag{1.3}$$

where $\kappa = \sqrt{\kappa_x^2 + \kappa_y^2}$.

On behalf of the evaluation of the scattered field is sometimes useful to evaluate the structure function of the random process z which is defined to be the mean square of the difference in z increases on a fixed length τ:

$$D(\tau) \overset{\Delta}{=} \left\langle [z(x, y) - z(x', y')]^2 \right\rangle \quad . \tag{1.4}$$

The structure function is related to the power spectra $\boldsymbol{S}$ (Ishimaru, 1993) and, for stationary surfaces, is formally equivalent to the correlation function:

$$D(\tau) = 2\sigma^2 [1 - C(\tau)] \quad . \tag{1.5}$$

A random rough surface is best described by its statistical properties. The surface is replaced by a two-dimensional random process.

If the surface is changing with time, a third dimension should be added. However, if the surface displacements are slow compared to the period of the illuminating wave, the surface can be considered as frozen and the time dependence ignored. This is the case, for instance for the ocean surface.

The following two assumptions are made :

1. The process is ergodic; this allows to replace ensemble averages by spatial (or temporal) averages. The measurement of a radar return, or of a brightness temperature, is obtained as the mean of a number of measurements separated in space (or in time).

2. The process is stationary and homogeneous (spatial stationarity). This implies that the statistical properties are invariant with respect to translation in space and time.

hence, the surface characteristics can be described by pdfs of displacement and slopes, and by covariances and the corresponding spectra.

1.3 The Kirchhoff Approximation

Consider a plane wave incident upon a separation random rough surface between air and a medium with dielectric constant ε_r (Fig. 1.1).

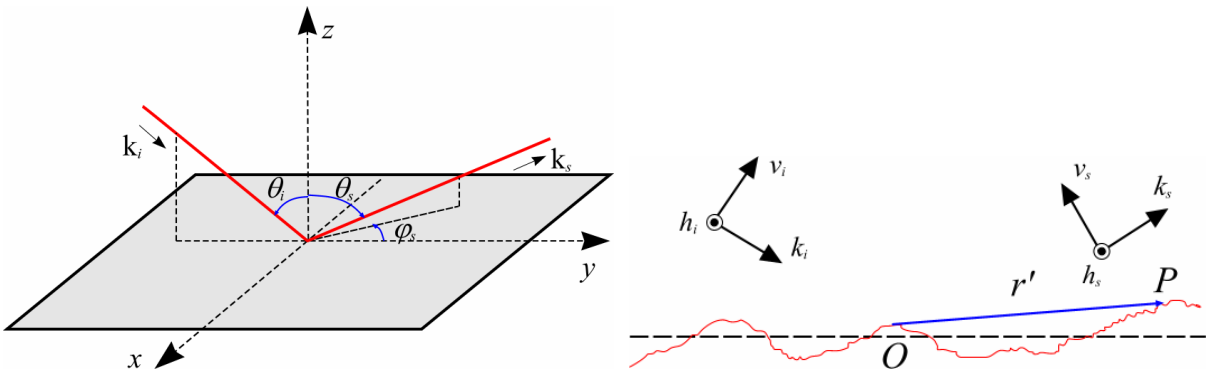

Fig. 1.1: Geometry of the problem.

The electric field of the incident wave on the surface is given by:

$$\mathbf{E}^{(i)}(\mathbf{r}') = \hat{\mathbf{e}}_i E_0 w(x', y') \exp(-jkr_l) \exp(-j\mathbf{k}_i \cdot \mathbf{r}') \quad , \tag{1.6}$$

where $\hat{\mathbf{e}}_i$ is the unit vector of the incident field, E_0 is a constant depending on the irradiate power and the distance r_l, k and $\mathbf{k}_i$ are the wave number and the wave vector of the incident field, respectively, and $w(x', y')$ is the illumination function. The unit vectors of the directions of propagation, horizontal polarization and vertical polarization for the incident and the scattered waves are:

$$\begin{aligned} \hat{\mathbf{k}}_i &= \hat{\mathbf{y}} \sin\theta_i - \hat{\mathbf{z}} \cos\theta_i \\ \hat{\mathbf{h}}_i &= \hat{\mathbf{x}} \\ \hat{\mathbf{v}}_i &= \hat{\mathbf{y}} \cos\theta_i + \hat{\mathbf{z}} \sin\theta_i \end{aligned} \tag{1.7}$$

$$\begin{aligned} \hat{\mathbf{k}}_s &= \hat{\mathbf{y}} \sin\theta_s \cos\varphi_s - \hat{\mathbf{x}} \sin\theta_s \sin\varphi_s + \hat{\mathbf{z}} \cos\theta_s \\ \hat{\mathbf{h}}_s &= \hat{\mathbf{y}} \sin\varphi_s + \hat{\mathbf{x}} \cos\varphi_s \\ \hat{\mathbf{v}}_s &= -\hat{\mathbf{y}} \cos\theta_s \cos\varphi_s + \hat{\mathbf{x}} \cos\theta_s \sin\varphi_s + \hat{\mathbf{z}} \sin\theta_s \end{aligned} \tag{1.8}$$

Considering the Equivalence Theorem, the Duality Theorem it is possible to express the scattered field, in the Fraunhofer region, in function of the tangential components of the electric and magnetic fields on the incidence surface (Kong, 1975):

$$\begin{aligned} \mathbf{E}^{(s)}(\mathbf{r}) = \frac{-jk \exp(-jkr_2)}{4\pi r_2} \left(\mathbf{I} - \hat{\mathbf{k}}_s \hat{\mathbf{k}}_s\right) \cdot \\ \int_{S'} \left\{\hat{\mathbf{k}}_s \times \left[\hat{\mathbf{n}}(\mathbf{r}') \times \mathbf{E}(\mathbf{r}')\right] + \varsigma \left[\hat{\mathbf{n}}(\mathbf{r}') \times \mathbf{H}(\mathbf{r}')\right]\right\} \exp(j\mathbf{k}_s \cdot \mathbf{r}') dS' \quad , \end{aligned} \tag{1.9}$$

where ς is the vacuum intrinsic impedance, $\mathbf{k}_s$ is the wave vector of the scattered field and $\hat{\mathbf{n}}(\mathbf{r}')$ is the unit vector perpendicular to the surface in $\mathbf{r}'$

$$\hat{\mathbf{n}}(\mathbf{r}') = \frac{-\xi\hat{\mathbf{x}} - \zeta\hat{\mathbf{y}} + \hat{\mathbf{z}}}{\sqrt{1 + -\xi^2 - \zeta^2}} \quad . \tag{1.10}$$

ξ and ζ are the local slopes in the $\hat{\mathbf{x}}$ and $\hat{\mathbf{y}}$ directions, respectively:

$$\xi = \frac{\partial z(x', y')}{\partial x'} \quad , \quad \zeta = \frac{\partial z(x', y')}{\partial y'} \quad . \tag{1.11}$$

In the Kirchhoff approach, an approximate expression for the surface fields is obtained using the tangent plane approximation. The fields at any point of the surface are approximated by the fields that would be present on the tangent plane at that point. Thus, the tangent plane approximation requires a large radius of curvature relative to the incident wavelength at every point on the surface (Beckmann and Spizzichino, 1963). In this case the surface can be confused with the tangent plane. Before proceeding further is important to note that to neglect the presence of shadowing and multiple scattering effects this approach is not applicable to the cases of low grazing incidence angle.

Hence, considering the tangent plane approximation the scattered field on the random rough surface is (Tsang *et al.*, 1985):

$$\begin{aligned} \mathbf{E}^{(s)}(\mathbf{r}) = {} & \frac{-jkE_0 \exp[-jk(r_1 + r_2)]}{4\pi r_2} \left(\mathbf{I} - \hat{\mathbf{k}}_s \hat{\mathbf{k}}_s\right) \cdot \\ & \int_{-\infty}^{+\infty} \int_{-\infty}^{+\infty} \mathbf{F}(\xi, \zeta) w(x', y') \exp[j(\mathbf{k}_i - \mathbf{k}_s) \cdot \mathbf{r}'] dx' dy' \quad , \end{aligned} \tag{1.12}$$

where $\mathbf{F}(\xi, \zeta)$ is a dimensionless function depending on the average Fresnel reflection coefficients over the mean plane, on the incidence and scattering angle and on the polarization:

$$\begin{aligned} \mathbf{F}(\xi, \zeta) = \sqrt{1 + \xi^2 + \zeta^2} \{ & -(\hat{\mathbf{e}}_i \cdot \hat{\mathbf{h}}_l)(\hat{\mathbf{n}} \cdot \hat{\mathbf{k}}_i)\hat{\mathbf{h}}_l(1 - R_h) + (\hat{\mathbf{e}}_i \cdot \hat{\mathbf{v}}_l)(\hat{\mathbf{n}} \times \hat{\mathbf{h}}_l)(1 + R_v) + \\ & + (\hat{\mathbf{e}}_i \cdot \hat{\mathbf{h}}_l)[\hat{\mathbf{k}}_s \times (\hat{\mathbf{n}} \times \hat{\mathbf{h}}_l)](1 + R_h) + (\hat{\mathbf{e}}_i \cdot \hat{\mathbf{v}}_l)(\hat{\mathbf{n}} \cdot \hat{\mathbf{k}}_i)(\hat{\mathbf{k}}_s \times \hat{\mathbf{h}}_l)(1 - R_v)\} \end{aligned} \tag{1.13}$$

$\hat{\mathbf{h}}_l$ and $\hat{\mathbf{v}}_l$ are unit vectors defining the local orthogonal and parallel polarizations:

$$\hat{\mathbf{h}}_l = \frac{\hat{\mathbf{k}}_i \times \hat{\mathbf{n}}}{|\hat{\mathbf{k}}_i \times \hat{\mathbf{n}}|} \quad , \quad \hat{\mathbf{v}}_l = \hat{\mathbf{h}}_l \times \hat{\mathbf{k}}_i \quad , \tag{1.14}$$

R_h and R_v are the Fresnel reflection coefficients:

$$R_h = \frac{\cos\theta_l - \sqrt{\varepsilon_r - \sin^2\theta_l}}{\cos\theta_l + \sqrt{\varepsilon_r - \sin^2\theta_l}} \quad , \quad R_v = \frac{\varepsilon_r \cos\theta_l - \sqrt{\varepsilon_r - \sin^2\theta_l}}{\varepsilon_r \cos\theta_l + \sqrt{\varepsilon_r - \sin^2\theta_l}} \quad , \tag{1.15}$$

and the local incidence angle θ_l is given by:

$$\cos\theta_l = -\hat{\mathbf{n}} \cdot \hat{\mathbf{k}}_i \quad . \tag{1.16}$$

Note that **F** depend on the integration variable only trough the local slopes α and β. Such dependence can be neglected in two cases: if the surface mean slope is small and if the frequency is high, i.e. $k \to \infty$.

1.3.1 Small Slopes Approximation

If the surface slope standard deviation is less than 1/4 (Ulaby *et al.*, 1982), in (1.12) **F** can be set as $\mathbf{F}(\xi,\zeta) \cong \mathbf{F}(0,0)$, i.e. the following approximations can be done: $\xi = \zeta = 0$; $\theta_l \equiv \theta_i$; $\hat{\mathbf{h}}_l \equiv \hat{\mathbf{h}}_i$; $\hat{\mathbf{v}}_l \equiv \hat{\mathbf{v}}_i$; $\hat{\mathbf{n}} \equiv \hat{\mathbf{z}}$**.** This approximation is known as *Small Slopes* or *Physic Optics*. The generic component of the scattered field, considering the incident field polarized horizontally or vertically, can be written as:

$$\mathbf{E}_q^{(s)}(\mathbf{r}) = \frac{-jkE_0 \exp[-jk(r_1 + r_2)]}{4\pi r_2} (\hat{\mathbf{q}} \cdot \mathbf{F}(0,0)) \int_{-\infty}^{+\infty} \int_{-\infty}^{+\infty} w(x', y') \exp[-j(\mathbf{k}_i - \mathbf{k}_s) \cdot \mathbf{r}'] dx' dy' \, , \tag{1.17}$$

where, p and q can be h or v, $\hat{\mathbf{q}}$ can be $\hat{\mathbf{h}}_s$ or $\hat{\mathbf{v}}_s$, and $\mathbf{F}_p$ can be $\mathbf{F}_h$ or $\mathbf{F}_v$, obtained setting $\hat{\mathbf{e}}_i = \hat{\mathbf{h}}_i$ and $\hat{\mathbf{e}}_i = \hat{\mathbf{v}}_i$ respectively. Hence:

$$\begin{aligned}
\hat{\mathbf{h}}_s \cdot \mathbf{F}_h(0,0) &= [(1-R_h)\cos\theta_i - (1+R_h)\cos\theta_s]\cos(\varphi_s - \pi) \\
\hat{\mathbf{v}}_s \cdot \mathbf{F}_h(0,0) &= [(1-R_h)\cos\theta_i \cos\theta_s - (1+R_h)]\sin(\varphi_s - \pi) \\
\hat{\mathbf{h}}_s \cdot \mathbf{F}_v(0,0) &= [(1+R_v) - (1-R_v)\cos\theta_i \cos\theta_s]\sin(\varphi_s - \pi) \\
\hat{\mathbf{v}}_s \cdot \mathbf{F}_v(0,0) &= [-(1+R_v)\cos\theta_s + (1-R_v)\cos\theta_i]\cos(\varphi_s - \pi)
\end{aligned} \tag{1.18}$$

A case of special interest in surface scattering is backscattering, since monostatic radar measurements fall in this category. Hence, in the backscattering configuration ($\theta_s = \theta_i$, $\varphi_s = \pi$) the (1.18) becomes:

$$\begin{aligned}
\hat{\mathbf{h}}_s \cdot \mathbf{F}_h(0,0) &= -2R_h(\theta_i)\cos\theta_i \\
\hat{\mathbf{v}}_s \cdot \mathbf{F}_h(0,0) &= \hat{\mathbf{h}}_s \cdot \mathbf{F}_v(0,0) = 0 \\
\hat{\mathbf{v}}_s \cdot \mathbf{F}_v(0,0) &= -2R_v(\theta_i)\cos\theta_i
\end{aligned} \tag{1.19}$$

If the scattering direction coincide with the specular reflection one ($\theta_s = \theta_i$, $\varphi_s = 0$), the (1.18) becomes:

$$\begin{aligned}
\hat{\mathbf{h}}_s \cdot \mathbf{F}_h(0,0) &= 2R_h(\theta_i)\cos\theta_i \\
\hat{\mathbf{v}}_s \cdot \mathbf{F}_h(0,0) &= \hat{\mathbf{h}}_s \cdot \mathbf{F}_v(0,0) = 0 \\
\hat{\mathbf{v}}_s \cdot \mathbf{F}_v(0,0) &= 2R_v(\theta_i)\cos\theta_i
\end{aligned} \tag{1.20}$$

1.3.2 Geometrical Optics Approximation

If the frequency is high enough, the integral (1.12) can be asymptotically evaluated applying the stationary phase method (Ulaby *et al.*, 1982). The phase term is:

$$\psi = (\mathbf{k}_i - \mathbf{k}_s)\cdot\mathbf{r}' = \mathbf{u}\cdot\mathbf{r}' = u_x x' + u_y y' + u_z z(x', y') \quad . \tag{1.21}$$

The stationary phase points are identified by the relations:

$$\frac{\partial \psi}{\partial x'} = u_x + u_z \xi = 0 \quad , \quad \frac{\partial \psi}{\partial y'} = u_y + u_z \zeta = 0 \tag{1.22}$$

Hence, in the stationary phase points:

$$\xi_0 = \frac{u_x}{u_z} \quad , \quad \zeta_0 = \frac{u_y}{u_z} \quad . \tag{1.23}$$

The slopes ξ_0 and ζ_0 make the local reflection direction coinciding the scattering one. In fact, considering (2.10), eq. (2.23) becomes:

$$\hat{\mathbf{n}} = (\mathbf{k}_s - \mathbf{k}_i)/|\,\mathbf{k}_s - \mathbf{k}_i\,| \quad . \tag{1.24}$$

Since the main contribute to the integral of the (1.12) is due to the stationary phase points, $\mathbf{F}$ can be set as $\mathbf{F}(\xi,\zeta) \cong \mathbf{F}(\xi_0,\zeta_0)$ and the generic component of the scattered field can be written as:

$$\mathbf{E}_q^{(s)}(\mathbf{r}) = \frac{-jkE_0 \exp[-jk(r_1+r_2)]}{4\pi r_2}\left(\hat{\mathbf{q}} \cdot \mathbf{F}(\xi_0,\zeta_0)\right)\int_{-\infty}^{+\infty}\int_{-\infty}^{+\infty} w(x',y')\exp[-j(\mathbf{k}_i - \mathbf{k}_s)\cdot\mathbf{r}']dx'dy' \,, \tag{1.25}$$

In the backscattering configuration ($\xi_0 = 0,\ \zeta_0 = \tan\theta_i$):

$$\begin{aligned} \hat{\mathbf{h}}_s \cdot \mathbf{F}_h(0,\tan\theta_i) &= \hat{\mathbf{v}}_s \cdot \mathbf{F}_v(0,\tan\theta_i) = -2R(0)/\cos\theta_i \\ \hat{\mathbf{v}}_s \cdot \mathbf{F}_h(0,\tan\theta_i) &= \hat{\mathbf{h}}_s \cdot \mathbf{F}_v(0,\tan\theta_i) = 0 \end{aligned} \tag{1.26}$$

If the scattering direction coincide with the specular reflection one ($\xi_0 = \zeta_0 = 0$), the (1.20) case is found.

1.3.3 Mean-square value of the scattered field

Since the scattering surface is described by a random process, the scattered field in any point of the space is a random variable. In many cases scattered field can be seen as complex Gaussian random variable, then the mean and the mean-square value, i.e. a second order statistical description, are enough to characterize the scattered field. Moreover, active microwave remote sensing systems usually measure the scattered power density, i.e. the normalized radar cross section (NRCS), hence a second order statistical description is certainly sufficient.

Before proceeding further, it is useful to give the expression for the NRCS in the monostatic case (backscatter):

$$\sigma_{pq}^{o} = \frac{4\pi r_2^2 \left\langle |\, E_q^{(s)} \,|^2 \right\rangle}{\mathcal{A}\, |\, E_0 \,|^2} \quad , \tag{1.27}$$

where $\mathcal{A}$ is the area of the illuminated surface.

Considering (1.17) or (1.25) the mean scattered field is given by:

$$\left\langle \mathbf{E}_q^{(s)}(\mathbf{r}) \right\rangle = \frac{-jkE_0 \exp[-jk(r_1 + r_2)]}{4\pi r_2} F_{pq} \cdot \int_{-\infty}^{+\infty}\int_{-\infty}^{+\infty} w(x', y') \exp[-j(u_x x' + u_y y')] \left\langle \exp[-ju_z z(x', y')] \right\rangle dx'\, dy' \,, \tag{1.28}$$

where $\mathbf{u} \equiv (u_x, u_y, u_z) = \mathbf{k}_i - \mathbf{k}_s$ and $F_{pq} \equiv \hat{\mathbf{q}} \cdot \mathbf{F}_{pq}$. If the surface is described by a Gaussian stationary random process (1.28) can be written as:

$$\left\langle \mathbf{E}_q^{(s)}(\mathbf{r}) \right\rangle = \frac{-jkE_0 \exp[-jk(r_1 + r_2)]}{4\pi r_2} F_{pq} \exp\left[-\frac{1}{2} u_z^2 \sigma^2 \right] W(u_x, u_y) \quad , \tag{1.29}$$

where W is the Fourier transform of w. If $u_z\sigma >> 1$, i.e. $\sigma >> \lambda$, the mean value of the scattered field is negligible. Moreover, if $w(x',y') = \text{rect}(x'/a)\text{rect}(y'/b)$, then:

$$\left\langle \mathbf{E}_q^{(s)}(\mathbf{r}) \right\rangle = \frac{-jkE_0 \exp[-jk(r_1+r_2)]}{4\pi r_2} F_{pq} \exp\left[-\frac{1}{2}u_z^2\sigma^2\right] \text{sinc}\left(\frac{u_x a}{2}\right) \text{sinc}\left(\frac{u_y b}{2}\right) \quad , \tag{1.30}$$

Hence, the mean field is maximum in the specular direction ($u_x = u_y = 0$) and, if $a>>\lambda$ and $b>>\lambda$, become negligible as soon as it depart from such direction. In other words, the mean field is always negligible but for a narrow cone around the specula direction; if the surface is very rough, the mean field is always negligible (Beckmann and Spizzichino, 1963).

Considering (1.17) or (1.25) the mean-square scattered field is given by:

$$\begin{aligned} \left\langle |\mathbf{E}_q^{(s)}(\mathbf{r})|^2 \right\rangle = \frac{k^2 |E_0|^2 |F_{pq}|^2}{(4\pi r_2)^2} \int\int\int\int w(x_1',y_1') w(x_2',y_2') \exp\{-j[u_x(x_1'-y_1') + u_x(x_2'-y_2')]\} \cdot \\ \cdot \left\langle \exp[-ju_z(z(x_1',y_1') - z(x_2',y_2'))] \right\rangle dx_1' dx_2' dy_1' dy_2' \end{aligned} \tag{1.31}$$

Since $z(x_1',y_1') - z(x_2',y_2')$ is a Gaussian stationary random process, it can be written:

$$\left\langle \exp[-ju_z(z(x_1',y_1') - z(x_2',y_2'))] \right\rangle = \exp\left[-\frac{1}{2}D(\tau)u_z^2\right] = \exp\left[-\frac{1}{2}2\sigma^2[1-C(\tau)]u_z^2\right] \quad . \tag{1.32}$$

and (1.31) can be integrated after a Taylor series expansion around the origin of the function $\cdot \exp[-1/2 \cdot 2\sigma^2[1-C(\tau)]u_z^2]$. Hence, the mean-square scattered field can be written as (Ulaby *et al.*, 1982):

$$\begin{aligned} \left\langle |\mathbf{E}_q^{(s)}(\mathbf{r})|^2 \right\rangle &= \frac{k^2 |E_0|^2 |F_{pq}|^2}{(4\pi r_2)^2} \exp(-u_z^2\sigma^2) \cdot \left[|W(u_x,u_y)|^2 + \sum_1^x \frac{u_z^{2m}}{m!} S^{(m)}(u_{xy}) \right] = \\ &= \left| \left\langle \mathbf{E}_q^{(s)}(\mathbf{r}) \right\rangle \right|^2 + \frac{k^2 |E_0|^2 |F_{pq}|^2}{(4\pi r_2)^2} \exp(-u_z^2\sigma^2) \cdot \sum_1^x \frac{u_z^{2m}}{m!} S^{(m)}(u_{xy}) \end{aligned} \tag{1.33}$$

where $u_{xy} = \sqrt{u_x^2 + u_y^2}$ and $\boldsymbol{s}^{(m)}(u_{xy}) = 2\pi\sigma^{2m}\int_0^\infty J_0(u_{xy}\tau)C^m(\tau)\tau d\tau$ and under the hypothesis that the function $w(x', y')$ is constant in a neighborhood considerably larger than the surface correlation length L. If $w(x', y') = \text{rect}(x'/a)\text{rect}(y'/b)$, this means $a>>L$ and $b>>L$.

For $k\sigma>>1$ the use of (2.33) may result awkward. However, in this case, $\cdot\exp[-1/2\cdot 2\sigma^2[1-C(\tau)]u_z^2]$ is always negligible except for $C(\tau)\cong 1$ and $C(\tau)$ can be considered even and derivable in 0. Then, (1.33) can be written as follows, recalling (1.23):

$$\left\langle |\mathbf{E}_q^{(s)}(\mathbf{r})|^2 \right\rangle = \frac{k^2 |E_0|^2 |F_{pq}|^2 \boldsymbol{A}}{(2u_z r_2)^2}\left\{\frac{1}{2\pi\sigma^2 |C''(0)|}\exp\left[-\frac{\xi_0^2+\zeta_0^2}{2\sigma^2 |C''(0)|}\right]\right\} \qquad (1.34)$$

where the term in the curly bracket represent the pdf of the correspondence of scattering and local specular reflection directions due to the surface slope (Tsang *et al.*, 1985; Ulaby *et al.*, 1982).

In the backscattering case the NRSC is:

$$\sigma_{pq}^o = \frac{|F_{pq}|^2}{2\sigma^2 |C''(0)| \cos^4\theta}\exp\left[-\frac{\tan\theta}{2\sigma^2 |C''(0)|}\right] \qquad (1.35)$$

1.4 The Small Perturbation Model

In the previous paragraph the KA was applied to surfaces with horizontal roughness scale and average radius of curvature larger than the electromagnetic wavelength. When both the surface standard deviation and correlation length are smaller than the wavelength, a different method must be used. The most commonly used formalism is the SPM, which requires the surface standard deviation to be less than about 5 percent of the electromagnetic wavelength (Tsang *et al.*, 1985; Ulaby *et al.*, 1982). This method consists in the evaluation of the scattered field as the sum of solution for the plane discontinuity case (specular reflection and

transmission according to the Snell Law) plus a small scattered field. The latter modeled as a sun of plane waves (Rayleigh hypothesis).

Consider a horizontally polarized plane wave incident upon a slightly rough interface (see Fig. 1.1), in the air the field is given by:

$$\begin{aligned} E_x(\mathbf{r}) &= \int_{-\infty}^{\infty}\int_{-\infty}^{\infty} U_x(u,v)\exp(jux+jvy-jwz)dudv + \\ &+ E_0\exp(-jky\sin\theta_i + jkz\cos\theta_i) + E_0R_h\exp(jky\sin\theta_i + jkz\cos\theta_i) \\ E_y(\mathbf{r}) &= \int_{-\infty}^{\infty}\int_{-\infty}^{\infty} U_y(u,v)\exp(jux+jvy-jwz)dudv \\ E_z(\mathbf{r}) &= \int_{-\infty}^{\infty}\int_{-\infty}^{\infty} U_z(u,v)\exp(jux+jvy-jwz)dudv \end{aligned} \quad , (1.36)$$

where $w=\sqrt{k^2-u^2-v^2}$, while in the dielectric:

$$\begin{aligned} E'_x(\mathbf{r}) &= \int_{-\infty}^{\infty}\int_{-\infty}^{\infty} U'_x(u,v)\exp(jux+jvy+jw'z)dudv + E_0T_h\exp(jk'y\sin\theta_t + jk'z\cos\theta_t) \\ E'_y(\mathbf{r}) &= \int_{-\infty}^{\infty}\int_{-\infty}^{\infty} U'_y(u,v)\exp(jux+jvy+jw'z)dudv \\ E'_z(\mathbf{r}) &= \int_{-\infty}^{\infty}\int_{-\infty}^{\infty} U'_z(u,v)\exp(jux+jvy+jw'z)dudv \end{aligned} \quad (1.37)$$

where k' is the wave-number in the dielectric and $w'=\sqrt{k'^2-u^2-v^2}$. By Snell's Low $k'\sin\theta_t = k\sin\theta_i$. the above formulations does not conserve the energy unless the coherently reflected and transmitted terms are modified to account for the energy in the scattered fields. However, if the surface is slightly rough the error is acceptable (Ulaby *et al.*, 1982).

The six unknown amplitudes $U_x, U_y, U_z, U'_x, U'_y, U'_z$ can be evaluated applying the boundary conditions to the tangential components of the field and considering the Maxwell equations in the two half-spaces. Since $z(x',y') << \lambda$, in (1.36-1.37) the exponentials in which z is present can be expanded in Taylor series considering only the first two terms.

Applying the same procedure to the vertically polarized incident filed, the generic component of the scattered field is given by:

$$E_q^{(s)}(\mathbf{r}) = E_0 \int_{-\infty}^{\infty}\int_{-\infty}^{\infty} j2k\cos\theta_i \alpha_{pq}(u,v) Z(u, v + k\sin\theta_i)\exp(jux + jvy - jwz)dudv \quad , \qquad (1.38)$$

where $Z(\cdot)$ is the Fourier transform of $z(x', y')$ and α_{pq} are given by:

$$\begin{aligned}
\alpha_{hh} &= [(\varepsilon_r - 1)\cos\varphi_s]\left[\cos\theta_s + (\varepsilon_r - \sin^2\theta_s)^{1/2}\right]^{-1}\left[\cos\theta_i + (\varepsilon_r - \sin^2\theta_i)^{1/2}\right]^{-1} \\
\alpha_{vh} &= \left[(\varepsilon_r - 1)(\varepsilon_r - \sin^2\theta_s)^{1/2}\right]\left[(\varepsilon_r - \sin^2\theta_s)^{1/2} + \varepsilon_r\cos\theta_s\right]^{-1}\left[\cos\theta_i + (\varepsilon_r - \sin^2\theta_i)^{1/2}\right]^{-1}\sin\varphi_s \\
\alpha_{hv} &= \left[(\varepsilon_r - 1)(\varepsilon_r - \sin^2\theta_i)^{1/2}\right]\sin\varphi_s\left[(\varepsilon_r - \sin^2\theta_s)^{1/2} + \cos\theta_s\right]^{-1}\left[\cos\theta_i + (\varepsilon_r - \sin^2\theta_i)^{1/2}\right]^{-1} \qquad (1.39) \\
\alpha_{vv} &= \left[(\varepsilon_r - \sin^2\theta_s)^{1/2}(\varepsilon_r - \sin^2\theta_i)^{1/2}\cos\varphi_s - \varepsilon_r\sin\theta_i\sin\theta_s\right](\varepsilon_r - 1)\cdot \\
&\quad \left[\varepsilon_r\cos\theta_s + (\varepsilon_r - \sin^2\theta_s)^{1/2}\right]^{-1}\left[\varepsilon_r\cos\theta_i + (\varepsilon_r - \sin^2\theta_i)^{1/2}\right]^{-1}
\end{aligned}$$

The scattered field in the far region can be asymptotically evaluated applying the stationary phase method (Ulaby *et al.*, 1982):

$$E_q^{(s)}(\mathbf{r}) = \frac{jkE_0\cos\theta_s}{2\pi r_2} j2k\cos\theta_i \alpha_{pq}(k_x, k_y) Z(k_x, k_y + k\sin\theta_i)\exp(jkr_2) \quad , \qquad (1.40)$$

where $k_x = -k\sin\theta_s\sin\varphi_s$ and $k_y = -k\sin\theta_s\cos\varphi_s$

1.4.2 Mean-square value of the scattered field

The mean-square value is given by (Ulaby *et al.*, 1982):

$$\left|\left\langle E_q^{(s)}(\mathbf{r})\right\rangle\right|^2 = \frac{4A\left|k^2\cos\theta_s\cos\theta_i\alpha_{pq}E_0\right|^2 \boldsymbol{s}(k_x, k_y + k\sin\theta_i)}{(2\pi r_2)^2} \quad . \qquad (1.41)$$

In the backscattering configuration ($\theta_i = \theta_s = \theta, \varphi_s = \pi$), applying the (1.41) to (1.27), the expression for the NRCS on is given by:

$$\sigma_{pq}^{o} = \frac{4k^4 \cos^4 \theta_i \left|\alpha_{pq}\right|^2 \boldsymbol{S}(0, 2K \sin\theta_i)}{\pi} \tag{1.42}$$

In this case:

$$\begin{aligned} \alpha_{hh} &= R_h(\theta) \\ \alpha_{vv} &= (\varepsilon_r - 1)\frac{\sin^2\theta - \varepsilon_r(1-\sin^2\theta)}{\left[\varepsilon_r \cos\theta + (\varepsilon_r - \sin^2\theta)^{1/2}\right]^2} \\ \alpha_{vh} &= \alpha_{hv} = 0 \end{aligned} \tag{1.43}$$

The surface spectrum $\boldsymbol{S}(0, 2K\sin\theta_i)$ is related to the electromagnetic wave number in this special case by the expression

$$k = 2K \sin\theta_i \tag{1.44}$$

This means that to the first order, backscattering from a slightly rough surface depends only on a particular frequency component of the surface roughness spectrum. The spatial wavelength of this component is related to the electromagnetic wavelength by (Tsang *et al.*, 1985; Ulaby *et al.*, 1982):

$$\Lambda = \frac{\lambda}{2K \sin\theta_i} \tag{1.45}$$

It follows that the surface component responsible for backscattering varies with the incident wavelength and angle.

1.5 Ranges of validity

It is useful to focus the attention on the ranges of validity of the KA e SPM models. This is sill an open matter and several approaches have been proposed. The condition of applicability are needed to avoid the cases of multiple scattering or shadowing. In the case of a surface is described by a stationary stochastic two-dimensional process, with Gaussian probability density function and Gaussian (or exponential) correlation function the applicability criteria of the two methods are simply related to the value of the product $k\sigma$. For example, according (Fung, 1994) the KA needs that $k\sigma > 1.5$, while according (Ulaby *et al.*, 1992) the SPM needs that $k\sigma < 0.3$. These latter condition, although effective, are not sufficient to completely define the applicability criteria. As regard the KA in (Papa and Lennon, 1984) reference is made on the value of the local radius of curvature which has to be grater that a reference value; for the SPM reference is made on the value of the *rms*.

In order to bridge the gap between the SPM and the KA, two-scale surface scattering models have been proposed (Write, 1968). There are several forms of the two-scale model in the literature. The most common is the one which is the sum of the KA and the first-order SPM averaged over the slope distribution of the large scale roughness. They are based on the assumption that the surface can be considered as the superposition of a large scale component and a small scale component, such that they satisfy the conditions of applicability of KA and of the SPM, respectively. The Kirchhoff model has several forms depending on the simplifying assumptions used in addition to the tangent plane approximation. The averaging operation of the small scale roughness also varies due to the way shadowing is accounted for.

Such constraining assumptions do not hold for all random rough surfaces. However the approach works rather well for certain classes of rough surfaces, such as the ocean surface, where the large scale and the small scale components correspond roughly to gravity waves and to capillary waves for the usual radar wavelength (Hasselmann *et al*., 1985; Brüning *et al.*, 1990). The various two-scale models mostly differ by the way the large scale and the small scale are defined.

1.6 Damping Model

In this paragraph a model for observable damping, based on the SPM and on the oil damping theory, is presented. The electromagnetic model is based on an enhanced damping model which takes into account oil visco-elastic properties and wind speed (Migliaccio *et al.*, 2005). At the basis of the physical damping theory background there is the fundamental action balance equation (Philips. 1966):

$$\frac{dN(\boldsymbol{K})}{dt} = \frac{\partial N(\boldsymbol{K})}{\partial t} + \boldsymbol{c_g} \cdot \nabla N(\boldsymbol{K}) = Q(\boldsymbol{K}) = Q_w + Q_{nl} - Q_d \,, \tag{1.46}$$

where $\boldsymbol{K}$ is the wavenumber vector, $N(\cdot)$ is the action spectral density defined as follows:

$$N(\boldsymbol{K}) = \frac{\Omega}{K} \boldsymbol{\mathcal{S}}(\boldsymbol{K}) = c_p \boldsymbol{\mathcal{S}}(\boldsymbol{K}) \quad . \tag{1.47}$$

$\boldsymbol{\mathcal{S}}(\boldsymbol{K})$ is the directional spectrum and Ω is the angular frequency of the wave defined by the dispersion relationship:

$$\Omega^2 = gK\left(1 + K^2 / K_m^2\right) \quad , \tag{1.48}$$

where g is the acceleration of gravity, $K_m=(\rho g/\tau)^{1/2}$, ρ is the sea water density and τ is the surface tension.

Equation (1.46) states that the energy content of wave propagating at the group velocity $\boldsymbol{c_g}$ is modified by source terms Q_w, Q_{nl} and Q_d which represent the spectral distribution of the energy input furnished by the wind, by the non-linear wave-wave interaction and subtracted by dissipation, respectively. This latter term is constituted by the terms Q_v and Q_{br} that represent the energy losses due to viscous dissipation and wave breaking, respectively.

Equation (1.46), for the case in question, is generally simplified as follows (Gade *et al.*, 1998a):

$$Q(\boldsymbol{K}) = Q_w + Q_{nl} - Q_d = 0 \quad . \tag{1.49}$$

Actually, the solution of (1.49) is not at all straightforward since the exact analytical expression of $Q(\cdot)$ is unknown. Hence, some physical assumptions are made to get the expression of $Q(\cdot)$. Let us now describe the various source terms.

The wind source term Q_w is here considered as (Gade *et al.*, 1998b):

$$Q_w = \beta \cdot N(\boldsymbol{K}) \quad . \tag{1.50}$$

The wind wave growth rate β for moderate wind regimes is described by a simple empirical expression (Plant, 1982):

$$\beta = B(\cos\varphi)^{2d} \left(\frac{u_*}{c_p} \right)^2 \Omega \quad , \tag{1.51}$$

where B=0.04, d=0.5, φ is the sea wave azimuth angle, i.e. the angle between wind and wave propagation direction, c_p is the phase velocity and u_* is the friction velocity.

The rate of energy transfer to waves is dependent on the profile of mean flow very close to the interface. If a neutral atmosphere is considered, i.e. such that there is not thermal exchange between air and water, the wind speed U at given height z above the surface is related to the wind friction velocity u_* by (Myrhaug and Slaattelid, 2002):

$$U(z) = \frac{u_*}{0.4} \ln\left(\frac{z}{z_0} \right) \quad . \tag{1.52}$$

In general, the roughness length z_0 depends on the sea state and thus on the wind velocity. Some relationships have been investigated to relate z_0 to u_*. In this study, we consider the new result obtained by (Donelan and Pierson, 1987), thus:

$$z_0 = 0.000037 \frac{U_{10}^2}{g} \left(\frac{c_p}{U_{10}} \right)^{-0.9} , \tag{1.53}$$

where U_{10} is the wind speed at 10 m of height.

If gentle wind regimes are in question, the expression for the wind wave growth coefficient becomes (Ermakov *et al.*, 1986):

$$\hat{\beta} = 10^{-2} \cdot Ku_* \cos\varphi \cdot \left[1 + 1.6 \frac{Ku_*}{\Omega} \cos\varphi \right] \cdot \left\{ 1 - \exp\left[8.9 \left(\frac{Ku_*}{\Omega} - 0.03 \right)^{1/2} \right] \right\} . \tag{1.54}$$

Let us now consider the dissipation terms.

Linear viscous dissipation in (1.46) can be described as follows (Gade *et al.*, 1998b):

$$Q_v = \chi N(\boldsymbol{K}) , \tag{1.55}$$

where the damping coefficient χ for the gravity-capillary waves in the presence of an elastic surface film can be written as (Ermakov, 2003):

$$\chi = 2\gamma K^2 + \frac{\chi_m}{2} \left| \frac{U_r}{U_p} \right|^2 . \tag{1.56}$$

The first term on the right-hand side of (1.56) is the well-known expression for the gravity-capillary waves damping in a fluid with a clean surface where γ is the kinematic viscosity of the sea water. The other term describes an additional damping due to the oil film in which χ_m is given by [26]:

$$\chi_m = \left(\frac{\gamma \Omega K^2}{2} \right)^{1/2} . \tag{1.57}$$

The ratio of the amplitudes of the vortex and potential components of gravity-capillary waves is defined by (Ermakov, 2003):

$$\left|\frac{U_r}{U_p}\right|^2 = 2\frac{e^2}{1-2e+2e^2} \quad , \tag{1.58}$$

where e dimensionless elasticity.

We note that although (1.56) is valid for purely elastic films, it is often applicable to thin (monomolecular) films, since surface film viscosity is usually small. When damping of thick crude oil film is in question one may think to consider appropriately tailored damping coefficient modeling. If gentle wind regimes are in question, the following expression for the viscous damping coefficient is used (Ermakov *et al.*, 1986):

$$\widehat{\chi} = 2\gamma K^2 \cdot \frac{\frac{2\gamma K^2}{\Omega} - \sqrt{\frac{2\gamma K^2}{\Omega}} \cdot \frac{EK^3}{\rho\Omega^2} - \left(\frac{EK^3}{\rho\Omega^2}\right)^2 \Big/ 2\sqrt{\frac{2\gamma K^2}{\Omega}}}{\frac{2\gamma K^2}{\Omega} - 2\sqrt{\frac{2\gamma K^2}{\Omega}} \cdot \frac{EK^3}{\rho\Omega^2} + 2\left(\frac{EK^3}{\rho\Omega^2}\right)^2} \quad . \tag{1.59}$$

The power-law approximation the non-linear term in (1.46) is (Gade *et al.*, 1998b):

$$Q_{br} = \overline{a}\left[K^4 \boldsymbol{S}(\boldsymbol{K})\right]^n \Omega N(\boldsymbol{K}) \quad , \tag{1.60}$$

where $\overline{a}$ is an empirical coefficient. Donelan and Pierson suggested to use (1.60) to phenomenological describe the surface wave breaking processes. Considering the spectrum of the wind waves under equilibrium state (dN/dt=0) from (1.46) we have (Gade *et al.*, 1998b):

$$\boldsymbol{S}(\boldsymbol{K}) \propto \sqrt{\frac{|\cos\varphi| u_*^2}{gK^7}} \quad . \tag{1.61}$$

In (Gade *et al.*, 1998b; Donelan and Pierson, 1987) a is set to 2^n where n is given by:

$$n = (n_1 - n_2)\left|2 - \frac{g + 3TK^2}{g + TK^2}\right|^d + n_2 \quad , \tag{1.62}$$

where T is the ratio between the surface tension τ and the density ρ; n_1, n_2, and d are dimensionless parameters determined from gravity wave observations and from radar backscatter measurements of gravity-capillary waves (Plant, 1982).

Lets consider now the observable damping model, i.e. the ratio of the NRCS in the slick-free and the slick covered cases.

Since, the thickness of the oil spill is very small compared to the microwave penetration depth at the sea, it is appropriate to consider the term α_{pq} unaffected by the presence of oil spill (Fung, 1994, Ulaby *et al.*, 1992). Accordingly, we have that the observable damping is given by:

$$\frac{\sigma_f^o}{\sigma_c^o} = \frac{N_f(\boldsymbol{K})}{N_c(\boldsymbol{K})} = \frac{\beta_c - \chi_c}{\beta_f - \chi_f} \cdot \frac{Q_{br}^f - Q_{nl}^f}{Q_{br}^c - Q_{nl}^c} \quad , \tag{1.63}$$

in which the symbols *f* and *c* are for slick-free and slick-covered sea surface respectively, and the (1.49), (1.50), (1.55) and (1.42) have been used.

In order to fully describe the observable damping we need to model the second factor appearing at the right side of the (1.63). Its analytical expression is unavailable and some approximations have been suggested in literature (Gade *et al.*, 1998b; Ermakov, 2004). In (Gade *et al.*, 1998b) an expression has been obtained by adjusting the model to measurements, in (Ermakov, 2004) some physical arguments have been given in support of the proposed expressions. According to (Gade *et al.*, 1998b); we have:

$$\frac{Q_{br}^f - Q_{nl}^f}{Q_{br}^c - Q_{nl}^c} = \frac{a_f}{a_c} \cdot r^{-n_c - 1} \cdot u_*^{n_f - n_c} \left(\sqrt{\frac{|\cos\varphi|}{g}}\right)^{n_f - n_c} \cdot K^{(n_f - n_c)/2} \quad , \tag{1.64}$$

The parameter r is the ratio of the friction velocities for slick-covered and slick-free surfaces and measures the reduction of friction velocity due to the oil spill.

Combining (1.62) and (1.64), a proper description of the non-linear and wave breaking terms is obtained

$$\frac{Q_{nl}^{f}-Q_{br}^{f}}{Q_{nl}^{s}-Q_{br}^{s}}=r^{\Delta n-4}\left(2u_{*}\sqrt{\frac{|\cos\varphi|K}{g}}\right)^{\Delta n}\quad , \tag{1.65}$$

where $\Delta n=n_f-n_c$.

Finally, the observable damping at moderate wind regimes is obtained:

$$\frac{\sigma_f^o}{\sigma_c^o}=\frac{N_f(K)}{N_c(K)}=\frac{\beta_c-\chi_c}{\beta_f-\chi_f}\cdot r^{\Delta n-4}\left(2u_{*}\cdot\sqrt{\frac{|cos\,\varphi|K}{g}}\right)^{\Delta n}. \tag{1.66}$$

At a gentle breeze, the viscous dissipation can be greater than the wind input. Equation (1.66) becomes zero when β_c and χ_c are equal. Therefore, the evaluation of the theoretical damping ratio is possible only for the case in which the wind input is greater than the viscous dissipation. At gentle wind regimes, the breaking wave term and the non-linear term in (1.49) can be neglected (Ermakov *et al.*, 1986).

Using (1.49), (1.54) and (1.59) the observable damping at gentle wind regimes is obtained (Ermakov *et al.*, 1986):

$$\frac{\sigma_f^o}{\sigma_c^o}=\frac{N_f(K)}{N_c(K)}=\frac{\hat{\chi}_c-\hat{\beta}_c}{\hat{\chi}_f-\hat{\beta}_f}\quad . \tag{1.67}$$

Equation (1.67) can be further simplified at very low wind regimes in which $\hat{\beta}$ can be neglected (Ermakov *et al.*, 1986).

References

Beckmann, P. and A.Spizzichino, *The Scattering of Electromagnetic Waves from Rough Surfaces*, Norwood, MA: Artech House, 1963.

Brüning C., W. Alpers, and K. Hasselmann, "Monte-Carlo Simulation Studies of the Nonlinear Imaging of a Two-dimensional Surface Wave Field by a Synthetic Aperture Radar," *Int. J. of Remote Sensing,* vol. 11, no. 10, pp. 1695-1727, 1990.

Ermakov S. A., M. Migliaccio, and M. Tranfaglia, "Oil spill Observation: a Physical Approach," in *Proc. USA-Baltic International Symposium "Advances in Marine Environ Research. Monitoring & Technologies"*, Klaipeda, Lithuania, 15-17 June 2004.

Donelan M. A. and W. J. P. Pierson, "Radar Scattering and Equilibrium Ranges in Wind-Generated Waves with Application to Scatterometry," *J. Geophys. Res.*, vol. 92, no. C5, pp. 4971-5029, May 1987.

Ermakov S. A., A. M. Zujkova, A. R. Panchenko, S. G. Salashin, T. G. Talipova, and V. I. Titov, "Surface Film Effect on Short Wind Waves," *Dynamics of Atmos. and Oceans*, no.10, pp. 31-50, 1986.

Ermakov S. A., "Resonance Damping of Gravity-Capillary Waves on the Water Surface Covered with a Surface-Active Film," *Izvestiya*, *Atmos. and Oceanics Physics*, vol. 39, no. 5, pp. 624-628, 2003.

Fung, A.K., Z.Li and K.S.Chen, "Backscattering from a Randomly Rough Dielectric Surface", *IEEE Trans. Geosci. Remote Sensing*, vol. 30, no. 2, pp. 356-369, 1992.

Fung, A.K., *Microwave Scattering and Emission. Models and Their Applications*, Norwood, MA: Artech House, 1994.

Gade M., W. Alpers, H. Huhnerfuss, V. R. Wismann, and P. A. Lange, "On the Reduction of the Radar Backscatter by Oceanic Surface Films: Scatterometer Measurements and Their Theoretical Interpretation," *Remote Sens. Environ.*, vol. 66, no. 1, pp. 52-70, Oct.1998.

Gade M., W. Alpers, H. Huhnerfuss, H. Masuko, and T. Kobayashi, "Imaging of Biogenic and Anthropogenic Ocean Surface Films by the Multifrequency/Multipolarization SIR-C/X-SAR," *J. Geophys. Res.*, vol. 103, no. C9, pp. 18851-18866, Aug. 1998.

Hasselmann K., R. K. Raney, W. J. Plant, W. Alpers, R. A. Shuchman, D. R. Lyzenga, C. Rufenach, and M. J. Tucker, "Theory of Synthetic Aperture Radar Ocean Imaging: a MARSEN View," *J. Geophys. Res.*, vol. 90, pp. 4659-4686, 1985.

Ishimaru, A., *Wave Propagation and Scattering in Random Media*, New York, NY: Academic Press, 1993.

Kong J. A., *Electromagnetic Wave Theory*, New York, NY: John Wiley & Sins, 1975.

Migliaccio M., M. Tranfaglia, and S.A. Ermakov, "A Physical Approach for the Observation of Oil Spills in SAR Images*," IEEE J. Oceanic Engineering*, vol. 30, no. 3, pp. 495-507, July 2005.

Myrhaug D. and O. H. Slaattelid, "Effects of Sea Roughness and Atmospheric Stability on Wind Wave Growth," *Ocean Eng.*, vol. 29, no. 9, pp. 1133-1143, Aug. 2002.

Papa R. J. and Lennon J. F, "Conditions for the Validity of Physical Optics in Rough Surface Scattering," *IEEE Trans. Antennas Propagat.*, vol. 36, n. 5, pp. 647-650, 1988.

Phillips O. M., *The Dynamics of the Upper Ocean.* Cambridge, UK: Cambridge University Press, 1966.

Plant W. J., "A Relationship Between Wind Stress and Wave Slope," *J. Geophys. Res.*, vol. C3, no. 87, pp. 1961-1967, 1982.

Tsang, L., J.A.Kong and R.T.Shin, *Theory of Microwave Remote Sensing*, New York, NY: John Wiley,1985.

Ulaby, F.T., R.K.Moore, and A.K.Fung, *Microwave Remote Sensing, vol. II*, Reading, MA: Addison-Wesley, 1982.

Wright J. W., "A New Model for Sea Clutter," *IEEE Trans. Antennas Propagat.*, vol. AP-16, n. 2, pp. 217-223, 1968.

Chapter 2: A SAR Sea Surface Waves Simulator

A SAR sea surface waves simulator, based on the velocity bunching (VB) theory and developed in the Matlab® programming language. The software has been designed and implemented both to allow a full comprehension of the physical mechanisms governing the SAR sea surface image formation and for educational use.

2.1 Introduction

SAR imaging of a dynamic scene, such as sea surface, is considerably more complex than the imaging of a stationary scene. In particular, though wave-like patterns are often discernible on sea surface SAR images obtained both from aircraft and space missions, the relationship between such patterns and the actual sea surface wave fields is an intriguing and non-trivial issue.

Hence, simulation procedures can be very helpful to shed light in physical aspects governing the SAR surface waves imaging. In fact, it is widely accepted that a full comprehension of the physical mechanisms governing the SAR sea surface image formation is an aspect that cannot be disregarded. Two main theories have been proposed: the distributed surface (DS) theory (Harger, 1980), and the velocity bunching (VB) (Alpers *et al.*, 1981) one. In simple terms, the DS theory focuses on the imaging of the sea wave pattern while the VB theory focuses on the simple particle scattering.

In literature there are some simulators based on the DS theory, (Harger and Korman, 1989, Franceschetti *et al.*, 1998), and some on the VB theory, (Brüning *et al.*, 1990; Vachon *et al.*, 1989). Unfortunately, these sea surface simulators are not sufficiently user-friendly.

In this chapter, a SAR sea surface waves simulator, based on the VB theory, is presented. It is entirely developed in Matlab® environment, which is probably the most popular programming environment at educational and research centers. Unlike the former simulators, this one uses a Graphic User Interface (GUI). Only a student version of Matlab® is requested, i.e. there is no need of particular toolboxes, and can run on Windows, Mac OS and Linux PC systems.

The effectiveness of the new simulator is shown by means of a set of meaningful examples.

2.2 Theory of SAR surface waves imaging

The electromagnetic interaction between the microwave radiation and the sea surface can be described by a two-scale model. This model distinguishes between small- and large- scale components of roughness. In particular in the context of SAR imaging is useful adopting a

separation scale (SAR separation scale) which is related to the SAR resolution cell (Hasselmann *et al*., 1985; Brüning *et al.*, 1990). As the matter of fact the ocean wave field is divided in to deterministic (ocean waves larger than the separation scale) and statistic (ocean waves smaller than the separation scale) regimes (Hasselmann *et al*., 1985; Brüning *et al.*, 1990; Bao, 1995). Since satellite and airborne SAR normally operates at incidence angles ranging between 20° and 70°, for low to moderate sea state it is possible it is normally assumed that the backscattering mechanism is primary Bragg scattering (Alpers *et al.*, 1981; Brüning *et al.*, 1990)

According to Bragg theory only sea waves whose wavelengths are the same order of the incidence electromagnetic one are "seen" by SAR. As a consequence longer waves are imaged indirectly because of amplitude and phase modulation processes, also known as Real Aperture Radar (RAR) and motion induced effects, respectively (Brüning *et al.*, 1990).

The RAR process, for low to moderate sea state, can be described by a linear function (weak modulation) which relates the NRCS to the long sea wave field. This function is known as RAR Modulation Transfer Function (MTF). According to this theory, the modulated NRCS, $\overline{\sigma}^{o}(\cdot)$, is given by (Bao, 1995):

$$\overline{\sigma}^{o}(\mathrm{z}_{o}) = \sigma^{o}\left\{1 + \sum_{m=1}^{M}\left|R^{RAR}(\boldsymbol{K}_{m})\right|\boldsymbol{s}(\boldsymbol{K}_{m})\cos(\boldsymbol{K}_{m}z_{o} + \varphi_{m} - \psi_{m})\right\} \quad , \tag{2.1}$$

where σ^{o} is the NRCS evaluated according to Small Perturbation Model (SPM), $|R^{RAR}(\boldsymbol{K}_{\mathrm{m}})|$ and ψ_{m} are the modulus and phase of the RAR MTF, respectively, $\boldsymbol{s}(\cdot)$ is related to the two-dimensional sea wave spectrum, which describes the energy distribution of a given sea state as a function of both frequency and direction (Apel, 1990), sampled at M (long wave) wavenumbers. x_0 is the azimuth coordinate over the sea reference plane, y_0 is the ground range coordinate over the sea reference plane, $z_o=(x_0,y_0)$. $\boldsymbol{K}$ is the long wave wavenumber, φ is an uniformly distributed random variable and M are the number of samples to represent the long waves.

The RAR MTF, under the assumption of linear modulation, does not depend on $\boldsymbol{s}(\cdot)$ and can be decomposed in three terms (Alpers *et al.*, 1981):

$$R^{RAR}(\boldsymbol{K})=R^{t}(\boldsymbol{K})+R^{r}(\boldsymbol{K})+R^{h}(\boldsymbol{K}) \quad . \tag{2.2}$$

The first term, $R^{t}(\cdot)$, is the tilt modulation term. It is due to a geometric tilting effect modeling the variations of the Bragg resonant wavenumber because of the incidence angle modulation along the long wave profile. Its contribute is stronger for HH polarization and for range traveling waves.

The second term, $R^{r}(\cdot)$, is the range bunching modulation term. Physically, it is due to the change of the effective backscattering area because of the slope variations along the long wave profile. This variation of the backscattering area modulates the backscattered power per unit area.

The third term, $R^{h}(\cdot)$, is the hydrodynamic modulation term. It is due to the interactions between long and short waves, in particular it describes the non-uniform distribution of the short waves over the longer ones. It is still a subject of research. Under the hypothesis of low to moderate sea state and neglecting wind drifts that might be induced by the waves, a theoretical expression can be found in (Alpers *et al.*, 1981). According to (Alpers *et al.*, 1981; Bao, 1995), $R^{h}(\cdot)$ depends on the azimuthal angle between the long waves and the Bragg one, the angular frequencies and wavenumbers of the long sea waves and on a parameter, μ, which is called relaxation rate. This latter is related to an offset between the crest of the long waves and the spectral energy peak of the short waves. It is a function which depends on wind and wavenumbers (Alpers *et al.*, 1981; Hara and Plant, 1994; Brüning *et al.*, 1994) and it is still an object of research.

The motion induced effects, are a SAR inherent artifact. They are caused by the fact that SAR achieves a fine azimuthal resolution recording the phase history of the backscattered signals by the observed scene over a finite integration time. Thus the radial component of the orbital motion associated with the long sea waves distort such phase history (Alpers and Rufenach, 1979). In particular the radial component of the orbital velocity gives rise to the well-known velocity bunching phenomena, i.e. scatter elements which are characterized by different orbital velocities are non-uniformly displaced in the SAR image plane, thus apparent position of the scattering elements are bunched and spread out (Alpers and Rufenach, 1979; Alpers *et al.*, 1981; Brüning *et al.*, 1990). The radial component of the orbital acceleration is responsible for the degradation of the azimuthal resolution.

Since both orbital acceleration and orbital velocity vary along the flight direction they can produce a wave-like pattern onto SAR images. However for certain radar and sea parameters the wave pattern can be severely distorted or completely smeared out (Alpers *et al.*, 1981; Brüning *et al.*, 1990). Actually, in addition to this acceleration induced mechanism, the azimuthal resolution is also degraded by the sub-resolution scale variations of the orbital velocities which characterize the different backscattering elements within the SAR resolution cell. This phenomena can be modeled by a scene coherence time, which is inversely proportional to the mean-square radial velocity of the backscattering elements within a SAR resolution cell (Bao, 1995). Such mean-square radial velocity can be estimated, under the hypothesis of short sub-resolution scale waves lying in the Phillips equilibrium range of the waves spectrum, according to (Brüning *et al.*, 1990). The orbital velocity $u_r(\cdot)$ and the acceleration in range direction $a_r(\cdot)$ are given by (Alpers *et al.*, 1981; Bao, 1995):

$$u_r(z_0) = \sum_{m=1}^{M} \boldsymbol{s}(\boldsymbol{K}_m)\Omega_m \left(\sin^2\vartheta\sin^2\phi_m + \cos^2\vartheta\right)^{1/2} \sin(\boldsymbol{K}_m z_0 + \upsilon_m) \quad , \tag{2.3}$$

and

$$a_r(z_0) = -\sum_{m=1}^{M} \boldsymbol{s}(\boldsymbol{K}_m)\Omega_m^2 \left(\sin^2\vartheta\sin^2\phi_m + \cos^2\vartheta\right)^{1/2} \cos(\boldsymbol{K}_m z_0 + \upsilon_m) \quad , \tag{2.4}$$

where υ_m depends on the local incidence angles and on ϕ_m (Alpers and Rufenach, 1979; Alpers *et al.*, 1981), which is the angle between the m-th sea wave propagation direction and the platform flight direction.

Once the main processes responsible for the wave-like formation onto SAR images have been described, the relationship between the SAR image intensity $I(\boldsymbol{x})$ and $\overline{\sigma}^o(\cdot)$ can be expressed as follows (Brüning *et al.*, 1990):

$$I(z) = \int \frac{\overline{\sigma}^o(z_0)}{\overline{\rho}_a^2(z_0)} \delta(y - y_0) \exp\left\{ -\frac{\pi^2}{\overline{\rho}_a^2(z_0)} \left[x - x_0 - \frac{R}{V} u_r(z_0) \right]^2 \right\} dz_0 \quad . \tag{2.5}$$

where $z=(x,y)$ are the azimuth and range coordinate over the SAR image plane, R and V are slant range of the target and platform velocity and $\delta(\cdot)$ is the Dirac delta function. The degraded azimuthal resolution $\bar{\rho}_a(\cdot)$ is given by (Bao and Alpers, 1998):

$$\bar{\rho}_a(z) = \left\{ \rho_a^2 + \left[\frac{\pi}{2} \frac{TR}{V} a_r(z_0) \right]^2 + \frac{\rho_a^2 T^2}{\tau_s^2} \right\}^{1/2} \quad , \tag{2.6}$$

where T is the SAR integration time, τ_s is the scene coherence time and ρ_a is the individual-look azimuthal resolution for a stationary target. Eq. (2.6) shows that the degradation in azimuth resolution increases with the ratio R/V, with the ratio T/τ_s and with the radial component of the orbital acceleration which increases with the amplitude $z(\cdot)$ and the angular frequency (see Eq. 2.4).

According to (Alpers and Rufenach, 1979) VB is related to the gradient of the orbital velocity in the azimuthal direction. To better understand this phenomena a $\mathscr{C}$ parameter was introduced for describing the degree of non-linearity of such phenomena (Brüning *et al.*, 1990):

$$\mathscr{C} = \frac{R}{4V} g^{1/2} K_p^{3/2} H_s \cos\vartheta \cos\varphi_p \quad , \tag{3.7}$$

where g is the acceleration of gravity, K_p and φ_p are the peak wave component and its propagation direction relative to the azimuth, respectively, and H_s is the significant wave-height.

In particular, VB is a linear imaging phenomena for $\mathscr{C} << 1$. It can be seen (Alpers and Rufenach, 1979; Alpers *et al.*, 1981; Brüning *et al.*, 1990) that for range traveling waves the orbital motion effects vanish and the waves are linearly imaged by SAR. For azimuthal traveling waves the imaging can become highly non-linear. Thus it is possible to say that the imaging process is always linear for range traveling waves and for quasi-range traveling waves. The definition of the width of the angular range depends on R/V, on $\boldsymbol{s}(\cdot)$ and on $\boldsymbol{K}$. In the linear imaging regime the velocity bunching can be described by a linear function

similarly to the RAR MTF, thus the overall SAR MTF can be defined as the complex sum of these two terms (Alpers and Rufenach, 1979; Alpers *et al.*, 1981; Brüning *et al.*, 1990).

In the simulator a general formulation (Alpers and Rufenach, 1979) has been used:

$$I(z) \approx \frac{\pi^{1/2}}{2} T^2 \rho_a \frac{\bar{\sigma}^o(\mathrm{z}_o)}{\left|1 + \frac{R}{V}\frac{\partial}{\partial x_0} u_r(\mathrm{z}_o)\right|} \quad . \tag{2.8}$$

Eq. (2.8) corresponds to (2.5) when $u_r(\cdot)$, $a_r(\cdot)$, $\bar{\rho}_a(\cdot)$ and $\bar{\sigma}^o(\cdot)$ are slightly variable within the azimuthal resolution cell.

2.3 The Simulator

In this paragraph the SAR simulator structure and the GUI are described. The simulator has been designed and implemented modularly, and the numerical code can be described according to the steps depicted in Fig. 2.1. For each step a brief description is given as well as the input and the output parameters.

Step I models the directional wave spectrum in the wavenumber range relevant to the long sea waves (such wavenumbers range goes up to the SAR separation scale). In the present version of the software a JONSWAP (Apel, 1990, Brüning *et al.* 1990) spectrum with a cosine-type spreading function is implemented. Such spectrum is educationally interesting since it is able to describe different sea states; fully and non-fully developed sea, and swell (Brüning *et al.* 1990). The input parameters relevant to this step are the number of harmonics and directions to be used to discretize the sea waves spectrum, the Phillips parameter and the spreading factor.

Step II generates a realization of the sea surface displacement associated with the long sea waves by means of the Random Phase Double Summation Technique (Miles and Funke, 1987) and sampled according to the sensor resolutions. The inputs are the wave amplitudes, the long wave wavenumbers and the sensor parameters. The output are the sea surface displacement and the local incidence angles.

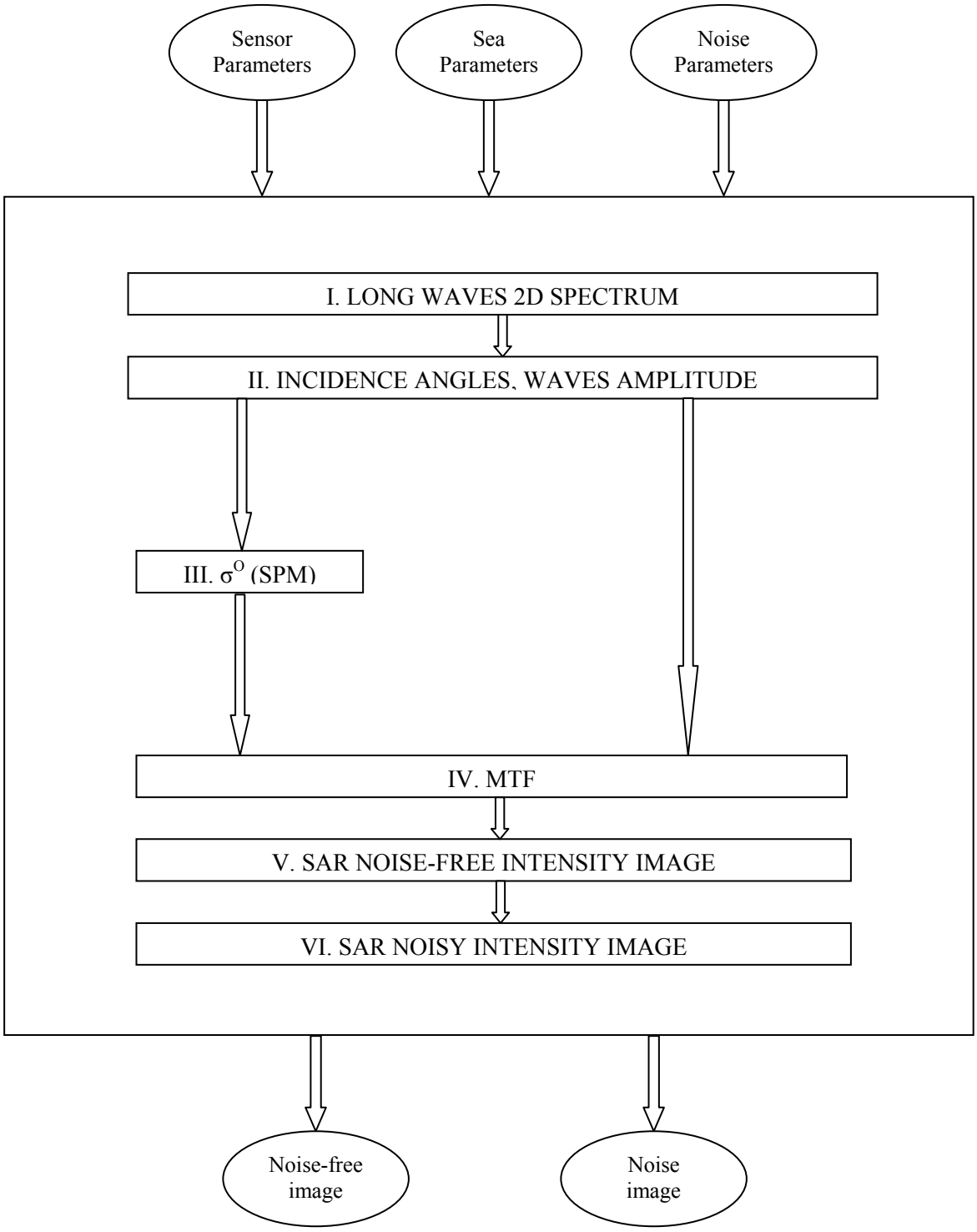

Fig. 2.1: SAR simulator block scheme.

Step III models the NRCS according to the SPM. The inputs are the electromagnetic wavelength, the local incidence angles, the wind direction, the sea surface temperature and

salinity (which are relevant to evaluate the complex sea dielectric constant) and the polarization. In the present version of the software the short wave spectrum is modeled by the Phillips spectrum and the long and the short waves are considered aligned.

Step IV evaluates the MTF which consists of the RAR MTF, and the motion induced effects. The inputs of the sub-step relevant to the RAR MTF are the NRCS, the long waves amplitudes and wavenumbers, the local incidence angles, the polarization and the relaxation rate (which is set according to Table 2.I (Brüning *et al.*, 1994)). The input parameters of the motion induced effects sub-step are the long waves amplitudes and wavenumbers, the local incidence angles and the long waves azimuth angles.

TABLE 2.I
RELAXATION RATE *M* FOR X-, C- AND L- BAND
AS A FUNCTION OF WIND SPEED.

Wind speed	**X band**	**C band**	**L band**
1-5 ms^{-1}	0.24 s^{-1}	0.1 s^{-1}	0.01 s^{-1}
> 5 ms^{-1}	1.7 s^{-1}	0.7 s^{-1}	0.1 s^{-1}

Step V evaluates the SAR noise-free intensity image once the RAR MTF, the motion induced effects and sensor parameters are provided. The intensity image is evaluated according to (2.8).

Step VI generates the SAR noisy intensity image once the SAR noise free image and the noise parameters are provided. In particular two noise sources are considered: the additive and the multiplicative one. The additive noise comes from multiple sources, most notably from internal thermal excitement of the electronic instruments and radiometric radiation incident on the antenna instrument. The internal thermal noise is the most significant contribute and it is zero mean and normally distributed with a white spectrum (Yoho and Long, 2003). It is a characteristic of the specific sensor. The multiplicative noise (speckle) is related to the coherent sum of responses from multiple surface scatters. In order to characterize speckle for this particular scenario, a Weibull distribution (Bucciarelli *et al.* 1995), filtered through an ideal bi-dimensional rectangular window whose cut-off frequencies are related to the range

and azimuth SAR resolution, is used. The Weibull distribution used is a two-parameters function given by (Bucciarelli *et al.* 1995):

$$p(I) = \frac{\ell}{a}\left(\frac{I}{\chi}\right)^{\ell-1} \exp\left[-\left(\frac{I}{a}\right)\right] \quad , \tag{2.9}$$

where I is the intensity of the noise-free SAR image, a and ℓ are scale and shape parameter of the distribution, respectively. The mean of the Weibull distribution is given by:

$$E[I] = \Gamma\left(1+\frac{1}{\ell}\right)a \quad , \tag{2.10}$$

where $\Gamma(\cdot)$ is gamma function. Once the mean value is set equal to the noise-free SAR image it is possible to obtain the scale parameter.

The external inputs to the simulator, are grouped into three classes, i.e. sensor, sea and noise inputs and they are detailed described in Appendix 2.A

2.4 Simulations

In this paragraph some meaningful simulations, related both to single monochromatic wave and to realistic sea wave spectrum, are shown in order to demonstrate the physical consistence of this SAR sea surface waves simulator.

In all subsequent simulations reference is made to ERS-1/2 SAR parameters (Table 2.II). The speckle noise is Weibull distributed with shape parameter equal to 2 (Table 2.II), scale parameter is set according to (2.10) once mean value has set equal to SAR noise-free image. The relaxation rate has been set according to Table 2.I and, for each simulation, long waves direction follows wind direction. Pixel size is taken half a resolution cell.

TABLE 2.II
INPUT PARAMETERS USED IN ALL SIMULATIONS.

Input parameter	Value
ERS-1 SAR	
Frequency	5.30 [GHz]
Flight direction	8 [degree]
Look angle	20.355 [degree]
Pulse Bandwidth	1.55499e+007 [Hz]
Platform height	785000 [m]
Platform velocity	6628 [m/s]
Sensor Integration Time	0.6 [s]
Polarization	VV
Azimuth antenna length L	10 [m]
Elevation antenna length W	1 [m]
Noise	
Noise floor	-23 dB
Weibull shape parameter	2
Sea	
Sea temperature	15 [°C]
Salinity	0.035 [psu]
Wind speed	10 [m/s]
Phillips parameter	0.0081
Peak enhancement factor	1

In the first case a single 60 m wavelength azimuth traveling long wave is simulated and the noisy SAR intensity image is shown in Fig. 2.2(a). To appreciate the results an azimuth transect (see white dotted line in Fig. 2.2(a)) is made in the noise-free SAR image (not shown) and referred to the corresponding long wave, see Fig. 2.2(b), where are plotted the first 200 pixels. Since an azimuth traveling wave has been simulated, the user can experience that the SAR imaging process is strongly non-linear in this case (Alpers *et al.*, 1981) as clearly shown in Fig. 2.2(b). In fact analyzing the plots of Fig. 2.2(b) it is possible to recognize the non-linear effect of VB. User can also evaluate the C parameter (2.7) which, in this case, is equal to 1 witnessing a strongly non-linear imaging process. User can also experience that in this case $R^t(\cdot)$ is equal to zero (Alpers *et al.,* 1981).

In the second case a single 100 m wavelength range traveling wave is simulated and the noisy SAR intensity image is shown in Fig. 2.3(a). Similarly to the former case a range transect (see white dotted line in Fig. 2.3(a)) is made in the noise-free SAR image (not shown) and referred to the corresponding long wave, see Fig. 2.3(b). User can appreciate that now the $\mathcal{C}$ parameter is equal to zero as expected (Alpers *et al.*, 1981) and witnessed by Fig. 2.3(b). User can physically explain the linear imaging process noting that the VB vanishes and the RAR MTF is maximum (Alpers *et al.*, 1981).

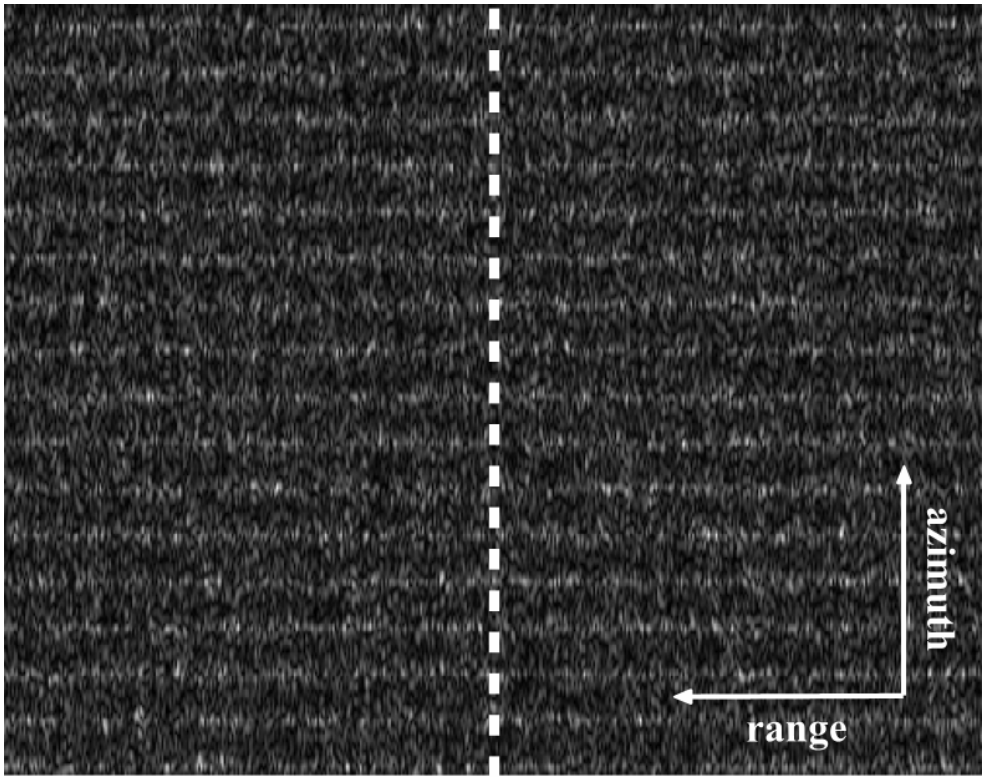

(a)

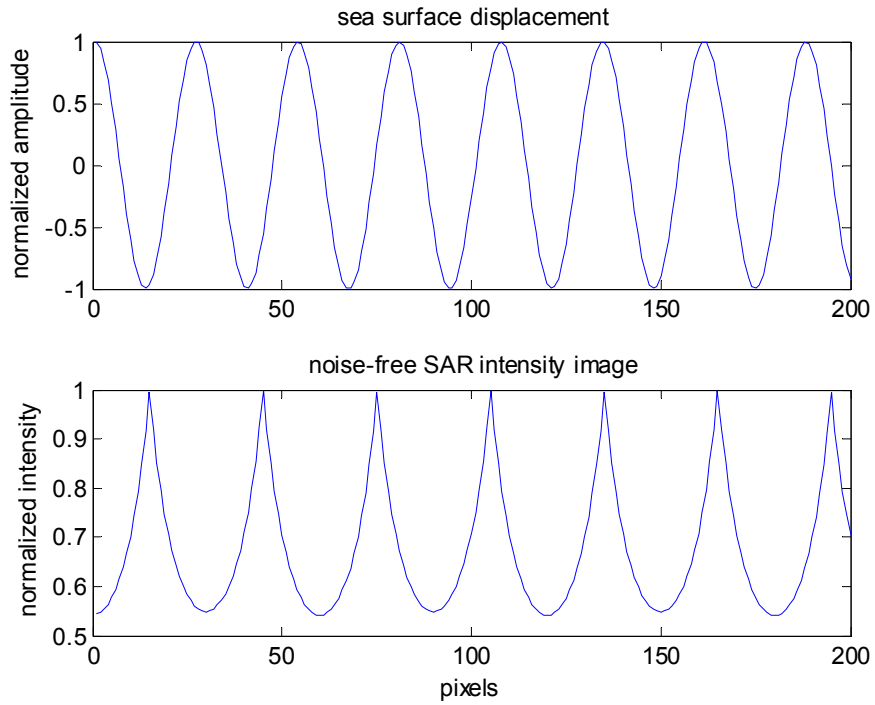

(b)

Fig. 2.2: a)Noisy SAR (500x500 pixels) image relevant to simulation 1. b) Plots of the 60 meters long ocean wave (up side) and of the simulated noise-free SAR image transect (bottom side), associated to Fig. 3.2(a). Both plots are normalized to the maximum.

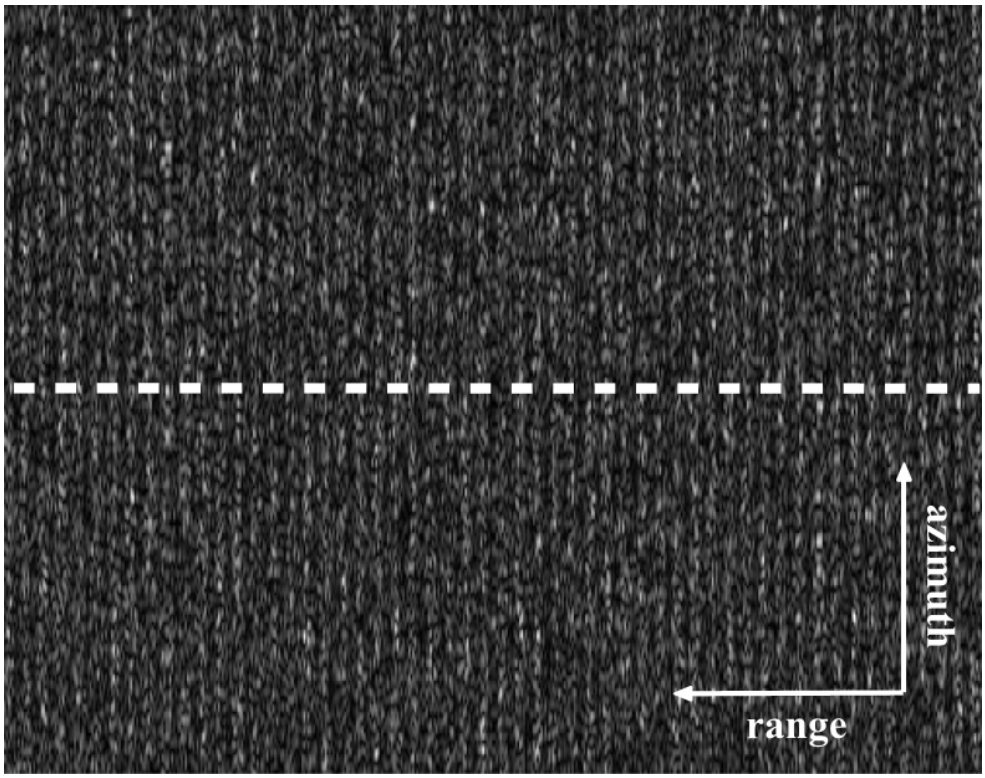

(a)

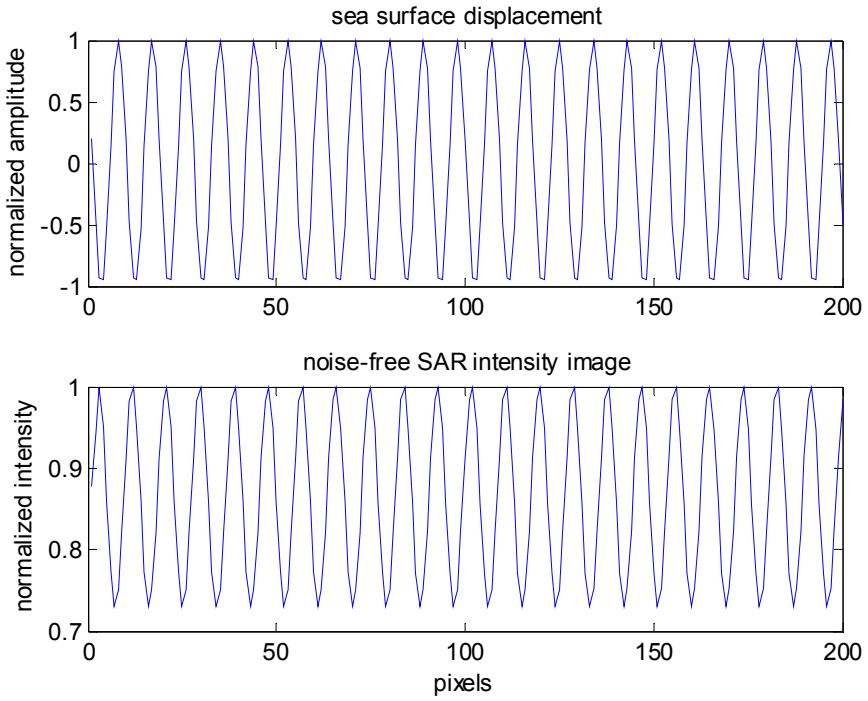

(b)

Fig. 2.3: a)Noisy SAR (500x500 pixels) image relevant to simulation 2. b) Plots of the 100 meters long ocean wave (up side) and of the simulated noise-free SAR image transect (bottom side), associated to Fig. 3.3(a). Both plots are normalized to the maximum.

User should be encouraged to take benefit to simulate a simple monochromatic long wave to fully understand basic, and non trivial, physical processes governing the formation of SAR images. In fact, user can appreciate the relative importance of the single terms of the RAR MTF as well as the dependency of the non-linear VB process on the long waves wavelength and directionality. By considering a sensor characterized by a different *R/V* user can learn the different VB effect. As a matter of fact, a larger sensor parameters choice will be included in a next version. Use can also appreciate that different salinity and sea temperature values do not play any role in the SAR imaging process. Further, user can experience that although the tilt modulation is larger for HH polarization than for the VV one, the overall return for VV polarization is stronger than HH (Alpers *et al.*, 1981).

Finally, user is ready to consider a more complex, i.e. realistic, sea wave field. The input parameters are shown in Table 2.II and the fully-developed JONSWAP spectrum is approximated by means of 60 wavenumbers.

In the first case a 100 m peak wavelength sea spectrum made of all range traveling components has been simulated and the relative SAR image is shown in Fig. 2.4(a). To better understand the SAR sea surface wave field imaging a simple one-dimensional spectral analysis can be made. As a matter of fact, a spectral analysis of a range transect (see dotted line in Fig. 2.4(a)), made in the noise-free SAR image (not shown) and referred to the corresponding spectral analysis of the sea surface displacement is shown in Fig. 2.4(b). User can appreciate that the imaging process is essentially linear, the peak wavelength is the same both in the sea surface and in the SAR spectrum. In particular in the latter one high wavenumber components, related to the Bragg resonant waves, are visible.

In the second case a 125 m peak wavelength sea spectrum, made of all azimuth traveling components, has been simulated and the relative noisy SAR image is shown in Fig. 2.5(a). Similarly to the former case the spectral analysis is shown in Fig. 2.5(b). User can appreciate the non-linearity of the SAR imaging process. In particular also this simple spectral analysis shows that in the SAR image spectrum the spectral energy is shifted towards lower wavenumbers, as predicted by (Bruning *et al.*, 1990). Therefore, user can evaluate the stretching parameter, defined according to (Bruning *et al.*, 1990) as the ratio between the wavelengths of the spectral peaks in the SAR image and in the sea plane, discovering that it is larger than one, as expected in (Bruning *et al.*, 1990).

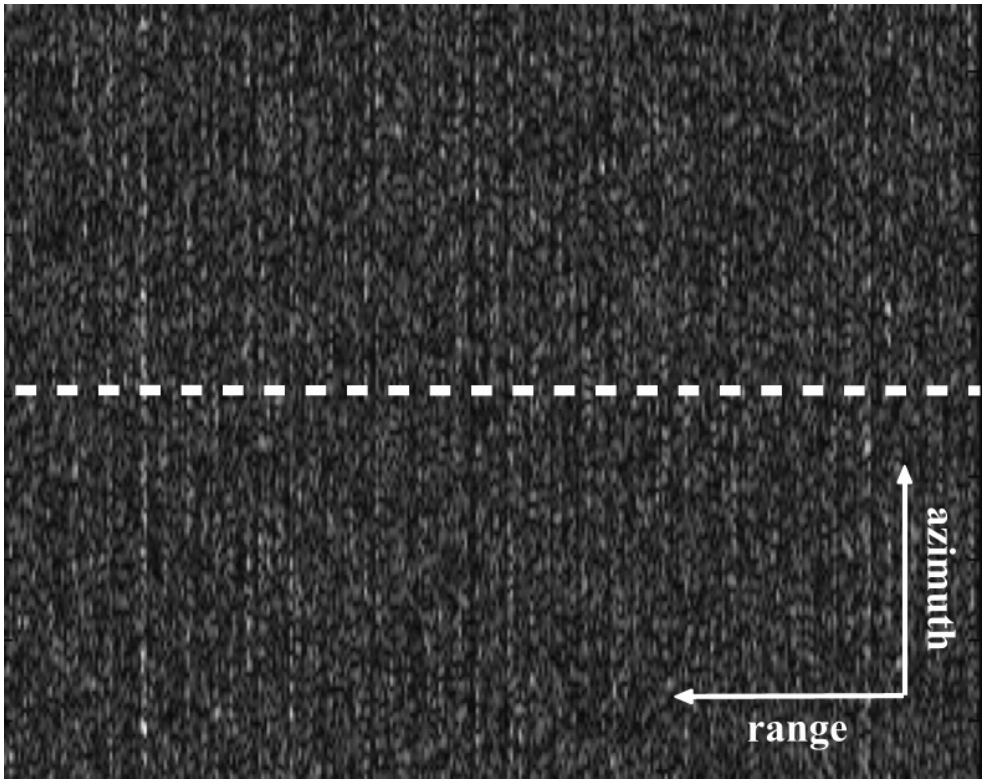

(a)

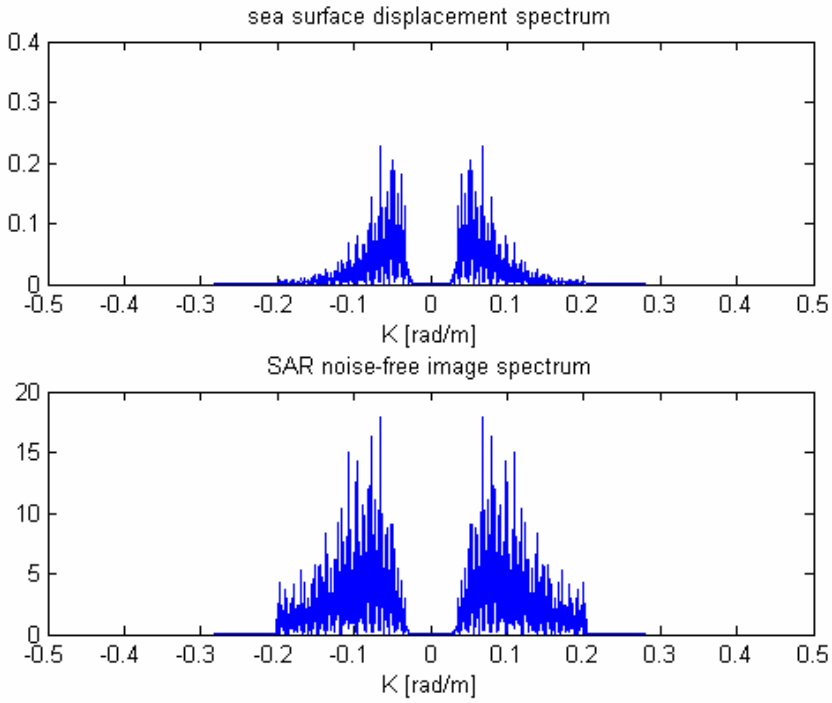

(b)

Fig. 2.4: a)Noisy SAR (500x500 pixels) image relevant to simulation 3. b) Plots of the spectral analyzed sea surface displacement (up side) and noise-free SAR image transect (bottom side), associated to Fig. 3.4(a).

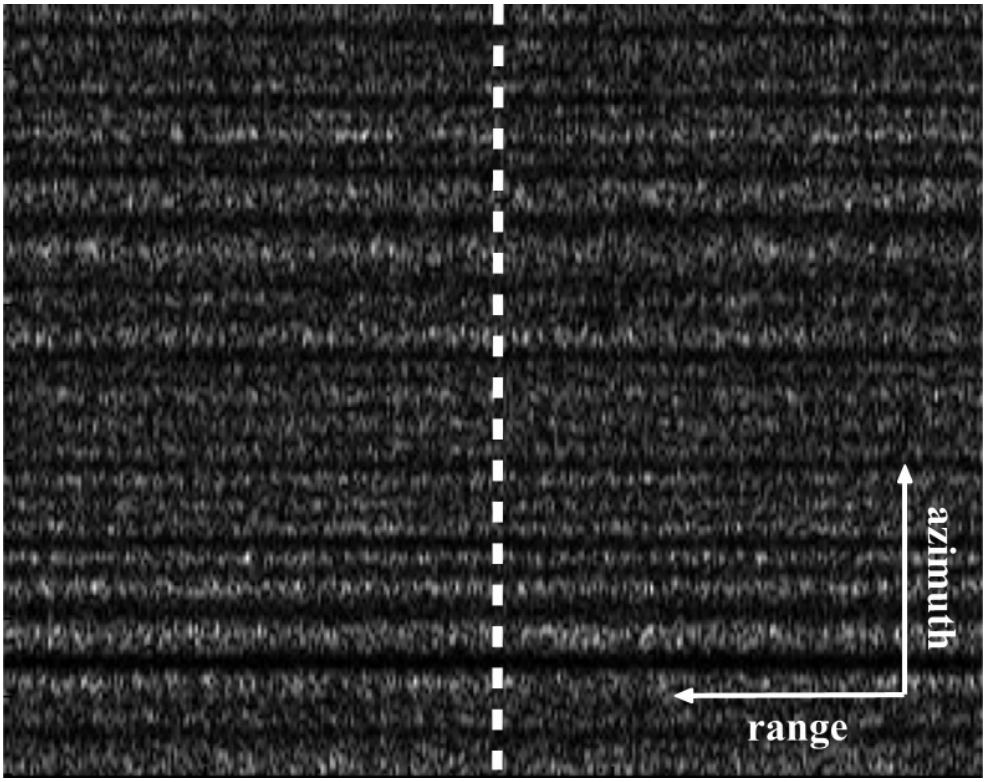

(a)

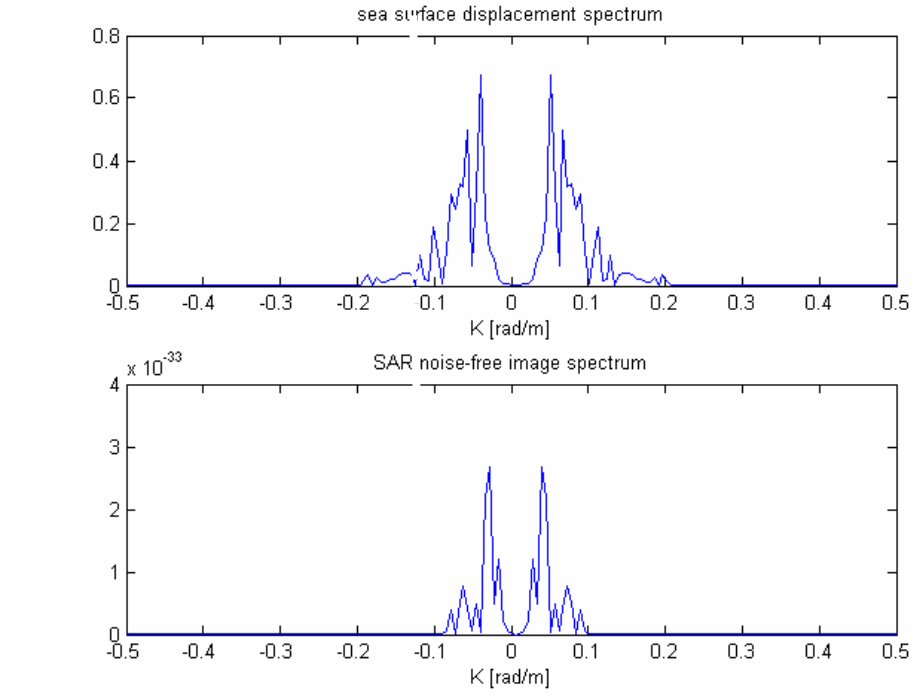

(b)

Fig. 2.5: a)Noisy SAR (500x500 pixels) image relevant to simulation 4. b) Plots of the spectral analyzed sea surface displacement (up side) and noise-free SAR image transect (bottom side), associated to Fig. 3.5(a).

As final examples, a broader spreading function is considered (spreading factor equal to 10), described by 30 components. In particular the noisy SAR intensity images shown in Figs. 2.6 and 2.7 are relevant to a 100 m sea peak wavelength, range traveling (Fig. 2.6), and azimuth traveling (Fig. 2.7). The SAR images clearly show that a broaden spreading function has been employed. Once again user can evaluate the $\mathcal{C}$ parameter, making reference to the peak wavelength and direction (Bruning *et al.*, 1990), recognizing that VB is a linear process in the first case and highly non-linear in the second one. User can also appreciate that the degree of non-linearity of the SAR imaging process decreases increasing the wind speed, as expected for fully-developed wind-seas (Bruning *et al.*, 1990).

Basically, users can understand that only by a critical analysis of the remotely sensed data, supported by a model (even if approximated or semi empirical) it is possible to infer about the geophysical parameters of interest. Because the simulator is able to give as output both the noisy and the noise free SAR image, it can be used an useful tool for developing and testing spectral estimators. Finally due to the modularly nature of the software it can be easily up-to-dated or modified adding *ad hoc* software blocks to add new features to the simulator.

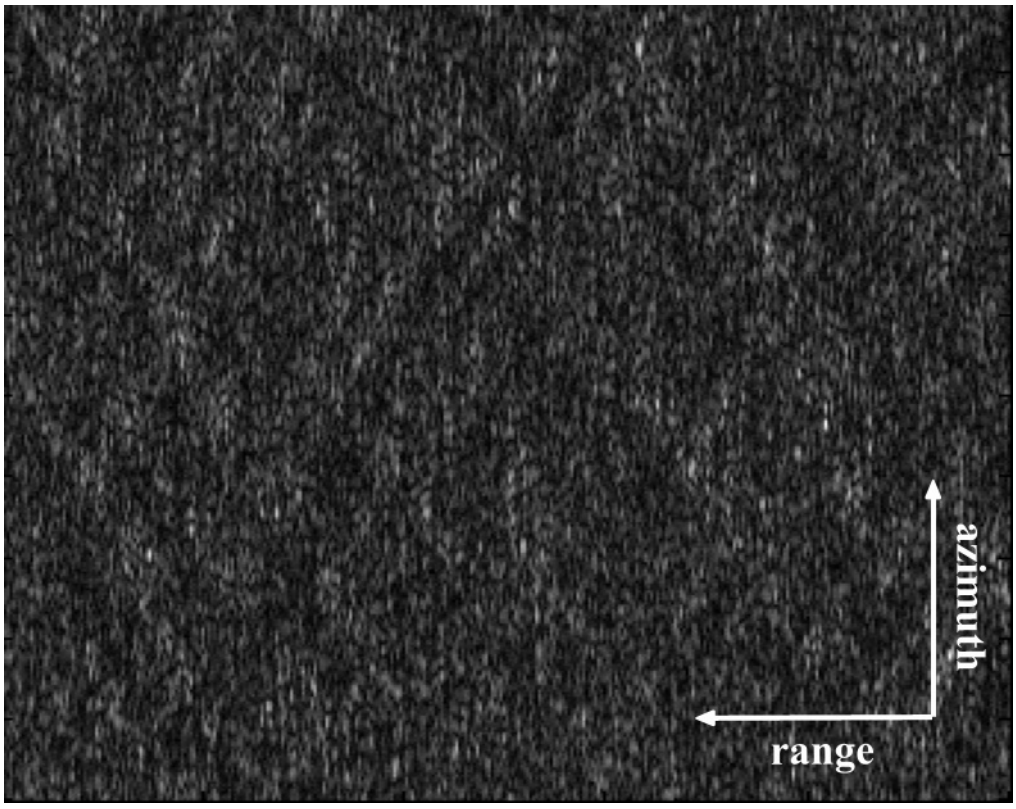

Fig. 2.6: Noisy SAR (500x500 pixels) intensity image.

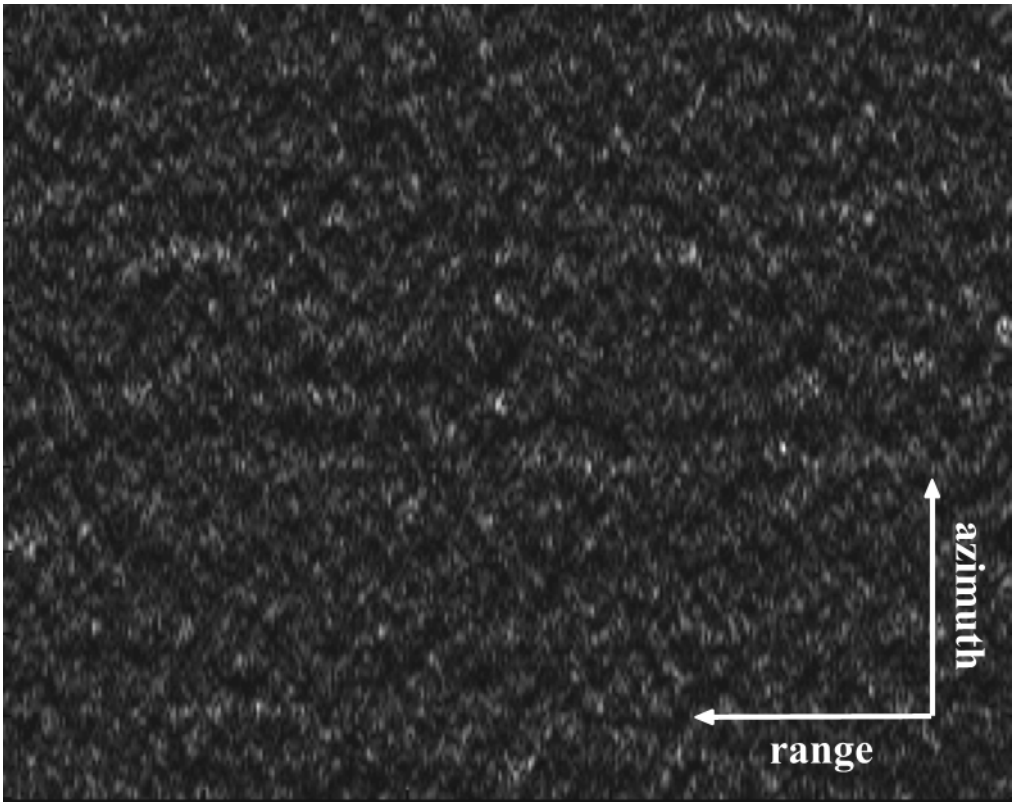

Fig. 2.7: Noisy SAR (500x500 pixels) intensity image.

Appendix 2.A: External inputs and GUI

The GUI allows user setting the external inputs by means of the *Input Parameters* menu (Fig. 2.8a). User is guided to provide physically consistent values by means of a warning message emphasizing if the parameter is out of the predefined expected range.

Scrolling the *Input Parameters* menu the *Sensor Parameters* window is found (Fig. 2.8b). In the present version of the software user is constrained among three data sets, which are relevant to the shuttle (HH and VV) L-band SIR-C and C-band SIR-C missions and to the satellite ERS-1 mission. Future developments may include a software code that helps in identifying free consistent radar parameters.

Scrolling the *Input Parameters* menu the *Sea Parameters* window is found (Fig. 2.8c). The temperature and salinity can be freely inserted by the user. The predefined expected ranges are 0°-35° and 5-45 psu, respectively. The wind speed and direction can be freely inserted by the user. The predefined wind speed constrain calls for occurrence of low to moderate sea state. Finally, the user must set some free parameters related to the discretization of the two-dimensional JONSWAP spectrum. However, to limit the phase locking effect a rather high number of spectral components is advisable to adopt (Miles and Funke, 1987). The spreading factor can be freely inserted by the user, provided that is positive and different from zero. The Phillips parameter and the peak enhancement factor allow simulating different sea states, however, in the present version of the software only fully-developed wind sea spectrum and swell can be simulated. The predefined expected values are, 0.0081 and 1, for fully developed spectrum, 0.25×10^{-3} and 10 for swell. Further developments will also allow considering non-fully developed sea state and simulating a wind-driven spectrum plus a narrow-band swell spectrum (Lemarie, 1999).

Scrolling the *Input Parameters* menu the *Noise Parameters* window is found (Fig. 2.8d). The Weibull shape parameter can be freely inserted by the user. The predefined shape parameter constrain calls for occurrence of different speckle distributions. In particular for shape parameter values ranging between 0 and 1 an exponential distribution is achieved, while, for values larger than 1 a Rayleigh distribution is achieved (Bucciarelli, 1995).

The GUI has two other menus: the Option and the File menus. The first one (Fig. 2.8e) consists of two parts: the first one (*Sensor Features* and *Image Features*) shows Footprint,

Fig. 2.8: GUI and main menus. a) Main menu. b) Input parameters menu: Sensor parameters window. c) Input parameters menu: Sea parameters window. d) Input parameters menu: Noise parameters window. e) File menu: Option menu. f) File menu: Image properties.

Swath, Range and Azimuth resolution due to the parameters previously set through Sensor parameters menu. Moreover simulated image sizes, in azimuth and range directions, are showed in terms of pixel. In the second part (*Image Definitions*) it is possible to reduce image size in order to have a quicker simulation. The second one (Fig. 2.8f) allows opening a previously simulated SAR image, to display its statistics, to print the SAR image and to exit from the SAR simulator (Fig. 2.9).

In each window clicking the *OK* button settings are saved. The simulation starts clicking the *RUN* button (Fig. 2.8a). Obviously the processing time depends on many factor, but the algorithm is quite fast (of the order of few minutes). Once the processing is completed the noisy and the noise-free intensity images are displayed. Then it is possible to save or not these images as *.dat files. In this case the two SAR images and an information *.txt file, which contains input and image parameters, are saved in an user defined folder. This latter are the outputs of the simulator.

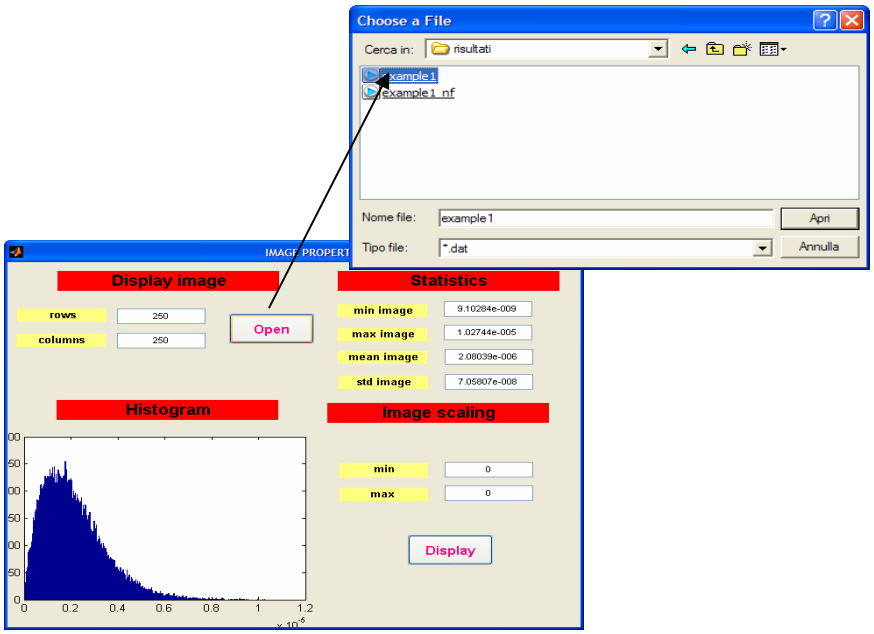

Fig. 2.9: Open file menu.

References

Alpers W. and C. Rufenach, "The Effect of Orbital Motions on Synthetic Aperture Radar Imagery of Ocean Waves," *IEEE Trans. Antennas Propag*, vol. AP-27, no. 5, pp. 685-690, 1979.

Alpers W., D. Ross, and C. Rufenach, "On the Detectability of Ocean Surface Waves by Real and Synthetic Aperture Radar," *J. of Geophysical Research,* vol. 86, no. C7, pp. 6481-6498, 1891.

Apel J. R., *Principles of Ocean Physics*. London, UK. Academic Press: International Geophysics Series, 1990.

Bao M., *On the Imaging of Two-dimensional Ocean Surface Wave Field by an Along-track Interferometric Synthetic Aperture Radar*. Ph.D. dissertation. The University of Hamburg, Germany. 1995,

Bao M. and W. Alpers, "On the Cross Spectrum Between Individual-look Synthetic Aperture Radar Images of Ocean Waves," *IEEE Trans. Geosci. Remote Sensing,* vol. 36, no. 3, pp. 922-932, 1998.

Brüning C., W. Alpers, and K. Hasselmann, "Monte-Carlo Simulation Studies of the Nonlinear Imaging of a Two-dimensional Surface Wave Field by a Synthetic Aperture Radar," *Int. J. of Remote Sensing,* vol. 11, no. 10, pp. 1695-1727, 1990.

Brüning C., R. Schmidt, and W. Alpers, "Estimation of the Ocean Wave-radar Modulation Transfer Function from Synthetic Aperture Radar Imagery. *J. of Geophysical Research,,* vol. 99, no. C5, pp. 9803-9815, 1994.

Bucciarelli T., P. Lombardo C. J. Oliver, and M. Perrotta, "A Compound Weibull Model for SAR Texture Analysis," *Proc. of IGARSS95,* vol. 1, pp. 181-183, 1995.

Ellison W., A. Balana, G. Delbos, K. Lamkaouchi, L. Eymard, C. Guillou, and C. Prigent, "New Permittivity Measurements of Seawater," *Radio Science*, vol. 33, no. 3, pp. 639-648, 1998.

Franceschetti G., M. Migliaccio, and D. Riccio, "On Ocean SAR Raw Signal Simulation," *IEEE Trans. Geosci. Remote Sensing,* vol. 36, no. 1, pp. 84-100, 1998.

Greco M., F. Bordoni, and F. Gini, "X-Band Sea-Clutter Nonstationarity: Influence of Long Waves," *IEEE J. Oceanic Eng.,* vol. 29, no. 2, pp. 269-283, 2004.

Hara T. and W. J. Plant, "Hydrodynamic Modulation of Short Wind-wave Spectra by Long Waves and its Measurement Using Microwave Backscatter," *J. of Geophysical Research,* vol. 99, no. C5, pp. 9767-9784, 1994.

Harger R. O., "The Synthetic Aperture Image of Time-variant Scenes," *Radio Science*, vol. 15, pp. 749-756, 1980.

Harger R. O. and C. E. Korman, "Comparisons of Simulated and Actual Synthetic Aperture Radar Gravity Wave Images," *J. of Geophysical Research,*, vol. 93, pp. 13867-13882, 1989.

Hasselmann K., R. K. Raney, W. J. Plant, W. Alpers, R. A. Shuchman, D. R. Lyzenga, C. Rufenach, and M. J. Tucker, "Theory of Synthetic Aperture Radar Ocean Imaging: a MARSEN View," *J. of Geophysical Research,*, vol. 90, pp. 4659-4686, 1985.

Lemaire D., P. Sobieski, and A. Guissard, "Full-range Sea Surface Spectrum in Nonfully Developed State for Scattering Calculations," *IEEE Trans. Geosci. Remote Sensing,* vol. 37, no. 2, pp. 1038-1051, 1999.

Miles M. D. and E. R. Funke, "A Comparison of Methods for Synthesis of Directional Seas," *Proc. of OMAE*, 1987.

Romaiser R. and D. R. Thompson, "Numerical Study on the Along-track Interferometric Radar Imaging Mechanism of Oceanic Surface Currents," *IEEE Trans. Geosci. Remote Sensing,* vol. 38, no. 1, pp. 446-458, 2000.

Vachon P.W, R. K. Raney, and W. J. Emery, "A Simulation for Spaceborne SAR Imagery of a Distributed Moving Scene," *IEEE Trans. Geosci. Remote Sensing,* vol. 27, no. 1, pp. 67-78, 1989.

Yoho P. and D. Long, "An Improved Simulation Model for Spaceborne Scatterometer Measurements," *IEEE Trans. Geosci. Remote Sensing,* vol. 41, no. 11, pp. 2692-2695, 2003.

Chapter 3: Detection of Dark Areas and Strong Scatterers in Marine SLC SAR Images

A new approach for the detection dark areas and areas with strong scatterers in marine Single-Look Complex (SLC) Synthetic Aperture Radar (SAR) images is here investigated. The approach is based on the use of the three parameters of the generalized K (GK) probability density function (pdf). The approach is physically based since the GK pdf is a suitable speckle model for marine SAR images ensuring a continuous and physically consistent transition among different scattering scenarios. This speckle model embodies the Rayleigh scattering scene, which is descriptor of scenes dominated by Bragg scattering, the Rice scattering scene, which is descriptor of areas in which a dominant scatter is present, and the K-distribution, which is descriptor of non-Gaussian signal statistic which normally characterize the sea echo from free-area illuminated by an high-resolution radar. A large data-set of ERS 1/2 SLC SAR images, provided by the ESA under the CAT-1 Project C1P-2769, is employed. Results show that the three differential GK parameters are suitable descriptors.

3.1 Introduction

Synthetic Aperture Radar (SAR) is the key sensor for several marine remote sensing applications. In this study the stochastic nature of a SAR image is investigated as an additional source of information to be exploited to learn more about the underlying physics.

Classical Rayleigh distribution model for the amplitude of backscattered signal well fits homogeneous land scenes and the backscattered signal from sea surface when a large area is illuminated by the radar. It represents a reference since it is associated to the so-called fully-developed speckle (Beckmann and Spizzichino, 1963). Moreover, when an high-resolution radar illuminates sea surface large deviations from Rayleigh statistic are often found, thus many other distributions have been proposed in literature to model the amplitude of high-resolution sea echo, i.e. they are the β, lognormal, Weibull, *K* and generalized *K* (GK) distributions (Beckmann and Spizzichino, 1963; Jakeman and Pusey, 1976; Jakeman, 1980; Bakarat, 1986; Jakeman and Tough, 1987; Maffett and Wackerman, 1991; Eltoft and Høgda, 1998; Greco *et al.*, 2004). The *K* pdf has been found to be a particularly useful model for sea amplitude statistics (Jakeman and Pusey, 1976), and has a reasonable justification in terms of physical scattering processes. It reduces to the Rayleigh pdf under appropriate circumstances (Jakeman and Pusey, 1976). Moreover, the *K* pdf model has been generalized to model the amplitude of backscattered signals with a non-uniform phase distribution by a fluctuating population of objects (Bakarat, 1986; Jakeman and Tough, 1987).

The proposed model is based on the GK pdf, which ensures a continuous and physically consistent transition among different scattering scenarios (Bakarat, 1986). This speckle model embodies the Rayleigh scattering scene, which is descriptor of scenes dominated by Bragg scattering, the Rice scattering scene, which is descriptor of areas in which a dominant scatter is present, and the *K*-distribution, which is descriptor of non-Gaussian signal statistic which normally characterize the sea echo from free-area illuminated by an high-resolution radar (Jakeman and Tough, 1987).

Hereafter, a study on the physical significance of the three GK distribution parameters, as descriptors of marine dark areas and strong (although small) scatterers in Single-Look Complex (SLC) SAR images, is investigated. In practice, instead of suppressing the speckle by means of appropriate averaging, which makes the SAR image spatial resolution coarser, the speckle statistics, under the unitary GK pdf, is used to assist physical interpretation. Such

approach is justified both from a theoretical and practical point of view. In fact, such model is able to describe the high-resolution SAR statistical behavior and is advisable when small dark areas and strong scatterers need to be detected. From the application stand point, this study can assist classical oil spill detection techniques.

In summary, the rationale of this study is to characterize the electromagnetic return of selected regions of interest (ROIs) over SLC SAR images by means of the three characteristic parameters of the GK distribution α, η and ν. Results show the effectiveness of the approach once that the differential GK parameters are used.

The reference data set, i.e. the ERS 1/2 SLC SAR VV polarized C-band images, has been provided by the European Space Agency (ESA) under the CAT-1 Project C1P-2769 and the wind data have been provided by NASA-PODAAC (SeaWinds/QuikSCAT) and by ECMWF.

3.2 The Model

In this paragraph the sea surface backscattering is described from physical and electromagnetic point of view. The behavior of sea surface backscattering is determined by the nature of the sea surface roughness (Jackson and Apel, 2004; Apel, 1990; Lemarie, 1998). This is normally characterized in terms of two fundamental types of waves: short and long waves (Jackson and Apel, 2004; Apel, 1990; Lemarie, 1998). The first ones, directly associated to the local wind, are characterized by a wavelength order of centimeters. The long waves, characterized by a wavelengths ranging from few hundreds meters to less than a meter, are, neglecting non-linear wave interactions, not always associated to the local wind. Thus at any point on the sea surface the waves are complex summation of the locally generated wind waves and waves propagating from different areas and directions, resulting in a complex interaction (Jackson and Apel, 2004; Apel, 1990; Lemarie, 1998).

According to the two-scale model the surface height is partitioned into a large-scale and a small-scale displacement (Jackson and Apel, 2004; Apel, 1990; Lemarie, 1998). Thus, over any patch of the surface, large compared with small-scale length but small respect to the large-scale length, the scattering can be generally modeled as first-order Bragg scattering from the small inhomogeneities (Jackson and Apel, 2004; Apel, 1990; Lemarie, 1998). The

effect of the large-scale structure is to modulate, both linearly and non-linearly, the small-scale scattering (Jakeman and Pusey, 1976; Greco *et al.*, 2004).

When the dominant mechanism is Bragg scattering it is possible to assume a fully developed speckle model for the statistical fluctuations of the backscattered signal. This is the case of sea surface when a weak large-scale modulation occurs or the area illuminated by the radar is too large with respect to the large-scale structure (Jakeman and Pusey, 1976; Jakeman, 1980; Bakarat, 1986; Jakeman and Tough, 1987; Maffett and Wackerman, 1991; Eltoft and Høgda, 1998; Greco *et al.*, 2004).

In this case the scattered field can be written as the sum of N elementary fields:

$$\mathbf{E}(\mathbf{r},t) = \sum_{n=1}^{N} a_n(\mathbf{r},t) e^{j\varphi_n(\mathbf{r},t)} \quad , \tag{3.1}$$

where j is the imaginary unit, $a_n(\mathrm{r},t)$ and $\varphi_n(\mathrm{r},t)$ are the real form and the relative phase factor (depending on the propagation path) governing the n-th elementary field. N, which is the number of elementary field scattering contributions, in far-field scattering geometries is defined by the size of the scattering region (Jakeman and Tough, 1987). Mathematically (3.1) can be seen as a N-step two-dimensional random walk in a complex plane where the $\{a_n\}$ and $\{\varphi_n\}$ represent the n-th step length and the associated phase shift, respectively (Bakarat, 1986). When N is a given number, assuming statistical independence between the $\{a_n\}$ and $\{\varphi_n\}$, if $\{\varphi_n\}$ are uniformly distributed the central-limit theorem, for asymptotically N large, can be exploited and fully developed speckle regime is achieved (Jakeman and Tough, 1987). In this case the scattered field can be described by a zero-mean circular complex Gaussian process. Hence, the field amplitude and intensity are Rayleigh and exponentially distributed, respectively (Bakarat, 1986; Jakeman and Tough, 1987). However, the above mentioned assumptions of randomness and statistical independence for (3.1), although likely in the case of a confused short-crested sea, may fail in presence of a large-scale modulation due to a long-wave field (Jakeman and Pusey, 1976). Thus, under this conditions, large deviation from Gaussian statistic is often found, particularly when an high-resolution radar, such as SAR, is considered (Jakeman and Pusey, 1976). In fact, when a SAR illuminates a sea area of linear dimensions comparable to the longer wavelengths on the sea surface, the modulation of

small-scale inhomogeneities by the larger ones cannot be neglected (Alpers *et al.*, 1981). Such modulation leads to the well-known bunching phenomena, which characterizes sea surface (Jakeman and Tough, 1987; Alpers *et al.*, 1981; Garello *et al.*, 1993). This phenomena can be included in the random walk (3.1) taking N as a random number fluctuating according to a negative binomial (NB) distribution, ruled by a non-negative bunching parameter α. For asymptotically large mean step number and under the hypothesis of strong scattering a non-fully developed model based on the K-distribution is achieved (Bakarat, 1986; Jakeman and Tough, 1987). The K pdf, relevant to the intensity of the scattered field ($i \equiv |\mathbf{E}|^2$), is given by (Jakeman and Pusey, 1976):

$$f(i) = \frac{2\alpha}{\Gamma(\alpha)\eta^{\alpha+1}} \alpha^{\frac{\alpha+1}{2}} K_{\alpha-1}\left(\frac{2}{\eta}\sqrt{\alpha i}\right) \quad , \tag{3.2}$$

where $\Gamma(\cdot)$ is the Eulerian gamma function, $K_{\alpha-1}(\cdot)$ is the modified Bessel function of the second kind of order $\alpha-1$ and η is the slope parameter. This is a two-parameters function which has shown a good agreement in fitting experimental data in a wide range of non-Gaussian scattering configurations, including microwave sea echo (Jakeman and Pusey, 1976; Jakeman, 1980; Jakeman and Tough, 1987; Eltoft and Høgda, 1998; Greco *et al.*, 2004). Eqquation (3.2) is a function of the modified Bessel function of the second kind and as the order of $K_{\alpha-1}(\cdot)$ gets larger the NB distribution, associated to N, tends to a Poisson distribution and the shape of (3.2) finally becomes an exponential pdf, i.e. a Rayleigh pdf for the field amplitude (Bakarat, 1986; Jakeman and Tough, 1987). Hence, α is unambiguously referred as shape parameter and can be used as indicator of the degree of non-Gaussian signal statistics (Eltoft and Høgda, 1998), which are due to some important physical causes as detailed in (Jakeman and Pusey, 1976; Jakeman and Tough, 1987; Eltoft and Høgda, 1998).

In summary, the shape parameter α is an indicator of the degree of non-Gaussian signal statistic, while the η parameter, under uniform large-scale conditions, is mainly related to the intensity of the local backscattering, due to the small-scale inhomogeneities (Jakeman, 1980; Greco *et al.*, 2004).

According to (Bakarat, 1986; Jakeman and Tough, 1987) it is possible to generalize this model considering a biased two-dimensional random walk (i.e. a non-uniform phase

distribution). In this case, for large mean step number, a GK pdf is obtained. This is a three parameters pdf whose expression, for the field intensity, is given by (Bakarat, 1986):

$$f(i)=\frac{2\alpha}{\Gamma(\alpha)\eta^{\alpha+1}}\left(\frac{\alpha}{1+\left(\frac{\nu^2}{4\alpha}\right)}\right)^{\frac{\alpha-1}{2}} i^{\frac{\alpha-1}{2}} I_o\left(\frac{\nu}{\eta}\sqrt{i}\right)K_{\alpha-1}\left\{\frac{2}{\eta}\left[\left(1+\frac{\nu^2}{4\alpha}\right)\alpha i\right]^{\frac{1}{2}}\right\} \quad . \qquad (3.3)$$

α and η are the same parameters shown in (3.2) and v deals with the presence of a dominant scatterer. The v parameter is expected to reveal the presence of a non-negligible coherent component in the backscattered sea surface signal, due, for example, to a ship.

Before proceeding further it is important to note that proper estimation of the three GK pdf parameters is an essential point to fully characterize the model. Estimation is a delicate matter which must be carefully considered (Eltoft and Høgda, 1998; Greco *et al.*, 2004; Joughin *et al.*, 1993; Corona *et al.*, 2004). According to (Eltoft and Høgda, 1998) the classical method of moments (MoM) (Bakarat, 1986), which consists of equating the first and the second empirical and theoretical GK moments, is not appropriate due to the flatness of these moments. An *ad hoc* procedure has been presented and discussed in (Greco *et al.*, 2004). It is based on the minimization of a two-dimensional functional and requires an accurate minimization routine to avoid convergence to local minima. Alternatively, a physically reliable and computer time effective sub-optimal approach is proposed in (Corona *et al.*, 2004). According to such approach v and η parameters are estimated by means of the Rice factor, i.e. the coherent to incoherent received power ratio. The α parameter is estimated by means of a numerical procedure, based on the χ^2 test, which minimize the L^2 error norm between the measured pdf and the theoretical GK pdf, where the α parameter is left free (Corona *et al.*, 2004). Therefore, α estimation is simple, viable and useful for physical interpretation of the presence of dominating scatterers.

3.3 Experiments

In this paragraph the physical relevance of the three GK distribution parameters, as descriptors of marine dark areas and strong (although small) scatterers over SLC SAR VV polarized C-band images, is presented and discussed. The SAR images were acquired by the Active Microwave Instrument (AMI) sensor mounted on board of the ERS-1/2 satellites operated by the ESA. The nominal resolution is 10 meters in range and 5 meters in azimuth.

The study is conducted evaluating the GK parameters relevant to the different ROIs. In order to better appreciate the parameters sensitivity, each ROI is coupled with an adjacent area (not shown), which is assumed as reference with respect to the interpretation of the estimated parameters. Such reference area is identical in size, is a non-dark area and without dominant scatterers. To further assist the physical interpretation of the results the wind speed is evaluated by the SAR images (Wackermann *et al.*, 1996; Fetterer *et al.*,1998; Korsbakken *et al.*,1998; Horstmann *et al.*, 2003; Horstmann and Koch, 2005; Herbach, 2005; Migliaccio and Reppucci, 2006). The evaluation of the wind speed by SAR data, although sub-optimal (Migliaccio and Reppucci, 2006), allows overcoming the incorrect time/spatial co-location between SAR data and operational wind data (Fetterer *et al.*,1998; Horstmann and Koch, 2005) and retrieves the wind speed at a finer spatial scale (1-2 Km) (Horstmann and Koch, 2005). In detail, once wind direction has been obtained from ECMWF/SeaWinds data, ocean surface wind speed is derived from the calibrated normalized radar cross section (NRCS) and image geometry by means of the C-band model CMOD5 (Herbach, 2005). The retrieved wind speed is relevant to areas of linear dimensions of about 1-2 Km, adjacent the ROIs. Wind speed is classified as low (< 3 m/s), moderate (3 to 7 m/s) and high (7 to 10 m/s) (Brekke and Solberg, 2005).

The first data set is relevant to the acquisition of 26 July 1992, 9:42 UTC (ERS-1, SLCI, orbit 5377, frame 2889, descending pass) off the coast of Malta. Fig. 3.1 shows the quick-look of the SAR image. The ROIs, which are manually selected in the SAR image, are shown in Fig. 3.2 which is made by two sub-images excerpted by Fig. 3.1. By visual inspection the following interpretation of the ROIs could be made. In the right and bottom-right side of the image (see Figs. 3.1 and 3.2a) several oil slicks are present. On the left side of the image (see Figs. 3.1 and 3.2b), near the coast of the isle of Malta, a low wind area is present, in the top-middle of the image some ships and small oil slicks are present. The ROIs relevant to low-wind areas are labeled as “LW”, oil slicks are labeled as “Oil” and the ROIs including the

ships are labeled as "S". In Fig. 2c a zoom of the SAR image relevant to Oil4 area is shown. The same format is used in all subsequent experiments. The SAR image regards a sea surface area characterized by a low-to-moderate wind speed.

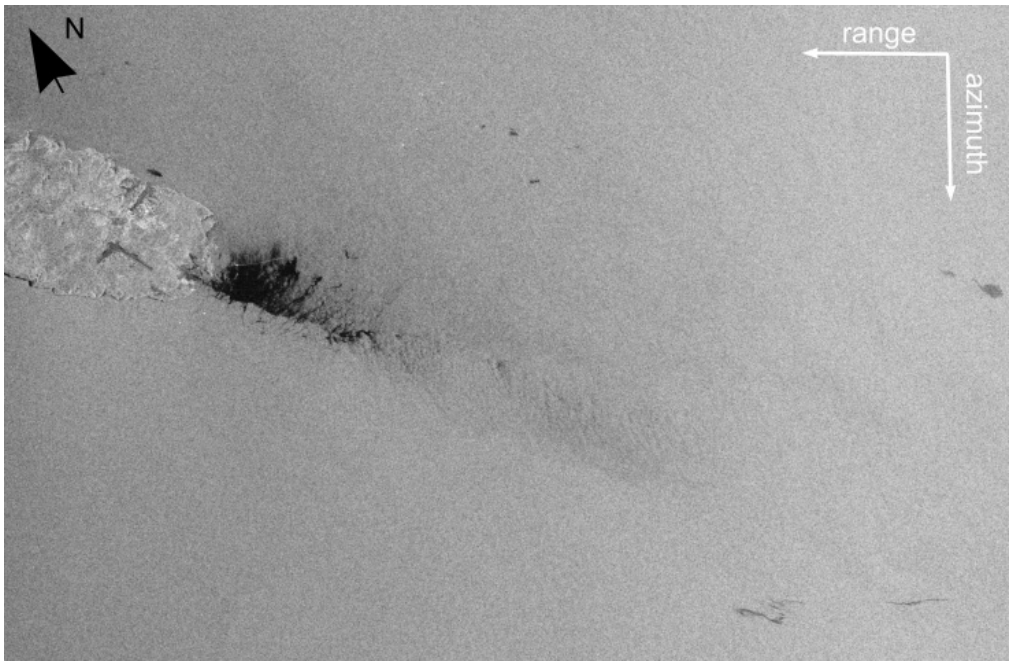

Fig. 3.1: Quicklook image of the area of interest relevant to the acquisition of 26 July 1992, 9:42 UTC (ERS-1, SLCI, orbit 5377, frame 2889, descending pass) off the coast of Malta.

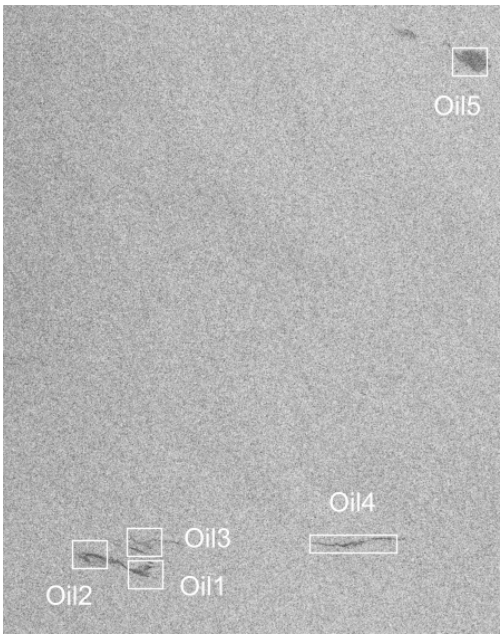

(a)

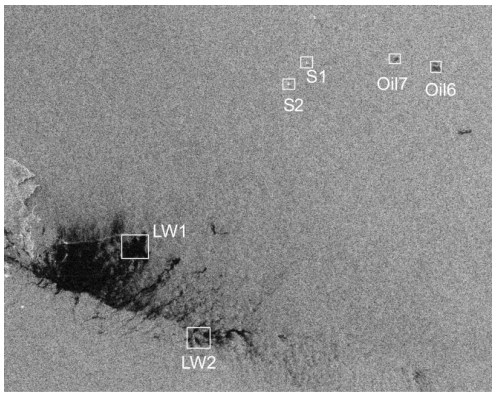

(b)

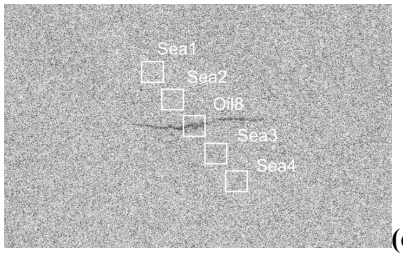

(c)

Fig. 3.2: Zooms of three part of SAR image of Fig.4.1.

In Tables 3.I and 3.II the GK parameters are listed for all ROIs and corresponding reference areas. In all cases the χ^2-test of hypothesis with a 95% confidence level was applied and passed.

Analysis of the three GK parameters shows that the absolute value of η is useless, the absolute value of α is of some interest and the absolute value of v is useful. Therefore the differential parameters $\eta_{\%}$ and $\Delta\alpha$ have been introduced. They are defined as follows:

TABLE 3.I
MEASURED GK PARAMETERS RELEVANT TO ROIS OF FIGS. 3.2(a)- 3.2(b).

ROI	η	$\eta_{\%}$	α	$\Delta\alpha$	v	$v_{\%}$	Wind
Oil 1	0.0009486	-52.9	9	-11	0.08	+14.2	Moderate
Ref. Sea	0.002014		20		0.07		
Oil 2	0.0008612	-56.2	9	-22	0.02	-33.3	Moderate
Ref. Sea	0.001968		31		0.03		
Oil 3	0.001568	-24.7	13	- ∞	0.02	-60.0	Moderate
Ref. Sea	0.002083		∞		0.05		
Oil 4	0.001083	-48.1	4	- ∞	0.04	-20.0	Moderate
Ref. Sea	0.002085		∞		0.05		
Oil 5	0.001122	-48.9	35	- ∞	0.03	-57.1	Moderate
Ref. Sea	0.002194		∞		0.07		
Oil 6	0.0007162	-52.8	6	-34	0.03	-72.7	Low
Ref. Sea	0.001520		40		0.11		
Oil 7	0.0006750	-55.6	3	-37	0.02	-81.8	Low
Ref. Sea	0.001520		40		0.11		
LW 1	0.0002059	-81.2	41	-13	0.04	-42.8	Low
Ref. Sea	0.001093		54		0.07		
LW 2	0.0009361	-29.7	1	- ∞	0.04	0.0	Low
Ref. Sea	0.001331		∞		0.04		
S1	0.01387	+950	NA	-	0.26	+766	Low
Ref. Sea	0.001320		∞		0.03		
S2	0.01225	+828	NA	-	0.45	+1400	Low
Ref. Sea	0.001320		∞		0.03		

TABLE 3.II
MEASURED GK PARAMETERS RELEVANT TO ROIS OF FIG. 3.2(c).

ROI	η	$\eta_{\%}$	α	$\Delta\alpha$	v	$v_{\%}$	Wind
Sea1	0.002182	0.0	∞	0	0.04	0.0	Moderate
Sea2	0.002084	-4.5	∞	0	0.11	+175	Moderate
Oil8	0.001093	-50.0	6	- ∞	0.08	+100	Moderate
Sea4	0.002170	-1.0	∞	0	0.05	+25.0	Moderate
Sea5	0.002099	-3.8	∞	0	0.03	-25.0	Moderate

$$\eta_{\%} = \left(\frac{\eta_{\mathrm{ROI}} - \eta_{\mathrm{Ref}}}{\eta_{\mathrm{Ref}}} \right) \cdot 100 \quad , \tag{3.4}$$

and

$$\Delta\alpha = \alpha_{\mathrm{ROI}} - \alpha_{\mathrm{Ref}} \quad . \tag{3.5}$$

With respect to η, all these experiments show that the dark areas are characterized by a negative $\eta_{\%}$ value around 50%. This is untrue for the Oil3 and LW2 ROIs, where $\eta_{\%}$ value is negative but higher. This can be physically explained by the sea-oil mixing occurring in the Oil3 area and in general by the heterogeneity of these two ROIs, see Figs. 3.1 and 3.2. Physically the characterization of dark areas in terms of negative $\eta_{\%}$ value is due to a smaller roughness in dark areas. Results listed in Table 3.II show that $\eta_{\%}$ exhibits only little variations among the adjacent Sea ROIs. Moreover, if the reference area is changed it is possible to note that the sign of $\eta_{\%}$ can change. It is also important to note that the S1 and S2 ROIs, characterized by the presence of a ship, exhibit a very high positive $\eta_{\%}$ value.

With respect to α it must be noted that the notation "∞" is used to emphasize that an high value (>60) is measured, since this means that a Gaussian scattering regime is in place. Results listed in Tables 3.I and 3.II clearly show that the dark areas are characterized by an high negative $\Delta\alpha$ value witnessing a change of the scattering regime. When the scattering regime changes from the non-Gaussian to the Gaussian case $\Delta\alpha$ is equal to $-\infty$, when scattering regime changes from different non-Gaussian cases $\Delta\alpha$ is finite and negative.

With respect to v, Tables 3.I and 3.II show that, as expected, it is very low for all dark and reference areas. In S1 and S2 ROIs v is much greater than usual values. To emphasize this it is appropriate to consider $v_{\%}$ defined analogously to (3.4). As result S1 and S2 ROIs are characterized by very high and positive $v_{\%}$ values. It must be noted however that surprisingly v is not as large as one would expect. In order to physically explain such unexpected result a detailed analysis was accomplished. Relevant pdfs (not shown to conserve space) are indistinguishable from a K pdf, but for some strong isolated outliers. These outliers witness the presence of few strong dominating scatterers. As matter of fact a Rice pdf in not achieved but the GK parameters estimation procedure fails to estimate the α value because the measured pdf shows some gaps and bins with very few number of samples (Corona *et al.*,

1996). The notation "NA" is used to emphasize this. In conclusion, the used GK parameters estimation procedure is able to frame ROIs in which a dominating scatterer is present.

The second data set is related to the acquisition of 16 July 1992, 9:56 UTC (ERS-1, SLCI, orbit 5234, frame 2871, descending pass) off the Tunisian coast. Fig.3.3 shows the quick-look of the SAR image and the selected ROIs are relevant to oil slicks, a low wind area, a ship and a dark area due to a current (labeled as "C"). The SAR image regards a sea surface area characterized by a moderate wind speed. Relevant results are shown in Table 3.III. Physical results are in total agreement to what formerly experienced.

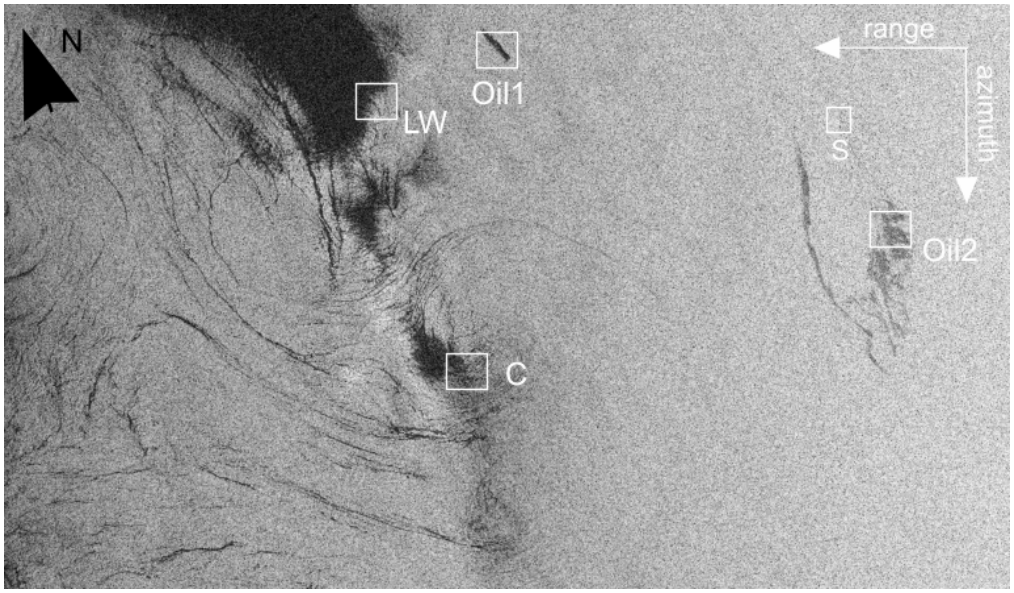

Fig. 3.3: Quick-look image of the area of interest relevant to the acquisition of 16 July 1992, 9:52 UTC (ERS-1, SLCI, orbit 5234, frame 2871, descending pass) and sketch of the ROIs selected for parameters estimation.

TABLE 3.III
MEASURED GK PARAMETERS RELEVANT TO ROIS OF FIG. 3.3.

ROI	η	$\eta_{\%}$	α	$\Delta\alpha$	ν	$\nu_{\%}$	Wind
Oil 1	0.0002422	-81.1	10	- ∞	0.01	-66.7	Moderate
Ref. Sea	0.001281		∞		0.03		
Oil 2	0.0007462	-61.1	7	- ∞	0.05	-16.7	Moderate
Ref. Sea	0.001915		∞		0.06		
LW	0.0002105	-82.5	13	-18	0.05	-28.6	Moderate
Ref. Sea	0.001201		31		0.07		
C	0.0004852	-57.8	3	-12	0.05	+66.7	Low
Ref. Sea	0.001148		15		0.03		
S	0.009930	+ 418	NA	-	0.26	+383	Moderate
Ref. Sea	0.001915		∞		0.06		

The following cases concern the well-known oil spill accidents which have been widely studied and documented, e.g. ([Int.3.1]; [Int.3.2]; [Int.3.3]).

The third data set is related to the acquisition of 02 June 2003, 21:02 UTC (ERS-2, SLCI, orbit 42439, frame 1107, ascending pass). Fig.3.4 shows the quick-look of the SAR image and the selected ROIs. In this case all ROIs are relevant to oil slicks. It is shown an oil slick of about 39 kmq offshore south of the Swedish coast caused by the Fu Shan Hai bulk carrier accident which occurred north of the Danish island of Bornholm in the Baltic Sea, on Saturday 31 May. More than 100 tonnes of heavy fuel oil began streaming from the ship hull, and currents carried the oil towards Sweden ([Int.3.1]). The interest on this data set is twofold: the dark area is relevant to a spillage 48 hours old and the scene is characterized by a high wind speed (8 m/s) ([Int.3.1]). Relevant results are shown in Table 3.IV. Physical results are in agreement to what formerly experienced. However, it must be noted that the $\eta_{\%}$ values are greater than standard one, see Tables 3.I-3.III. This is physically due to the oil spill aging process which is not balanced by the high wind speed regime (Espedal and Wahl, 1999).

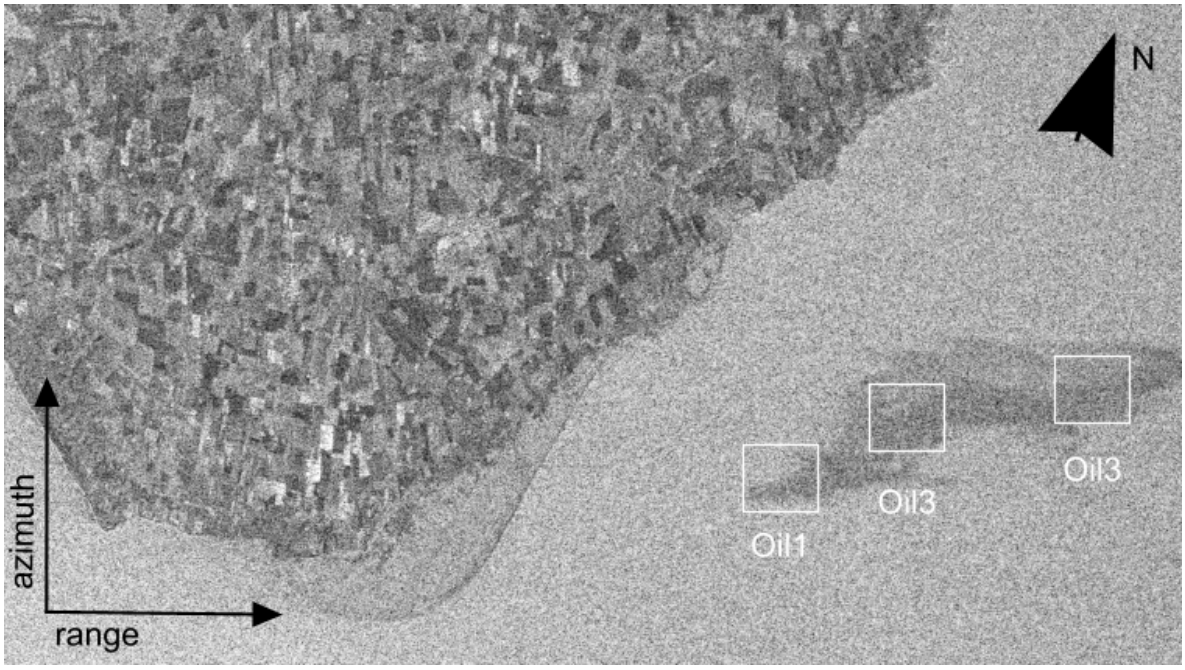

Fig. 3.4: Quick-look image of the area of interest relevant to the acquisition of 02 June 2003, 21:02 UTC (ERS-2, SLCI, orbit 42439, frame 1107, ascending pass) and sketch of the ROIs selected for parameters estimation.

TABLE 3.IV
MEASURED GK PARAMETERS RELEVANT TO ROIS OF FIG. 3.4

ROI	η	$\eta_{\%}$	α	$\Delta\alpha$	ν	$\nu_{\%}$	Wind
Oil 1	0.001074	-20.1	5	-33	0.01	-66.7	High
Ref. Sea	0.001343		38		0.03		
Oil 2	0.0008146	-38.3	10	-10	0.01	-50.0	High
Ref. Sea	0.001321		20		0.02		
Oil 3a	0.0007391	-37.7	15	-18	0.02	0.0	High
Ref. Sea	0.001185		33		0.02		
Oil 3b	0.0009366	-21.0	17	-16	0.01	-50.0	High
Ref. Sea	0.001185		33		0.02		

The last data set is relevant to the acquisition of 04 October 1994, 11:20 UTC (ERS-1, SLCI, orbit 16838, frame 2781, descending pass). Fig. 3.5 shows the quick-look of the SAR image and the selected ROIs relevant to oil slicks, a ship and a dark area due to a rain cell (labeled as "RC"). It is shown a huge oil slick near the Portuguese coast caused by the oil tanker Cercal accident which struck a rock while entering the Oporto harbor, releasing about 1.000 tonnes of crude oil into the sea on 02 October 1994.

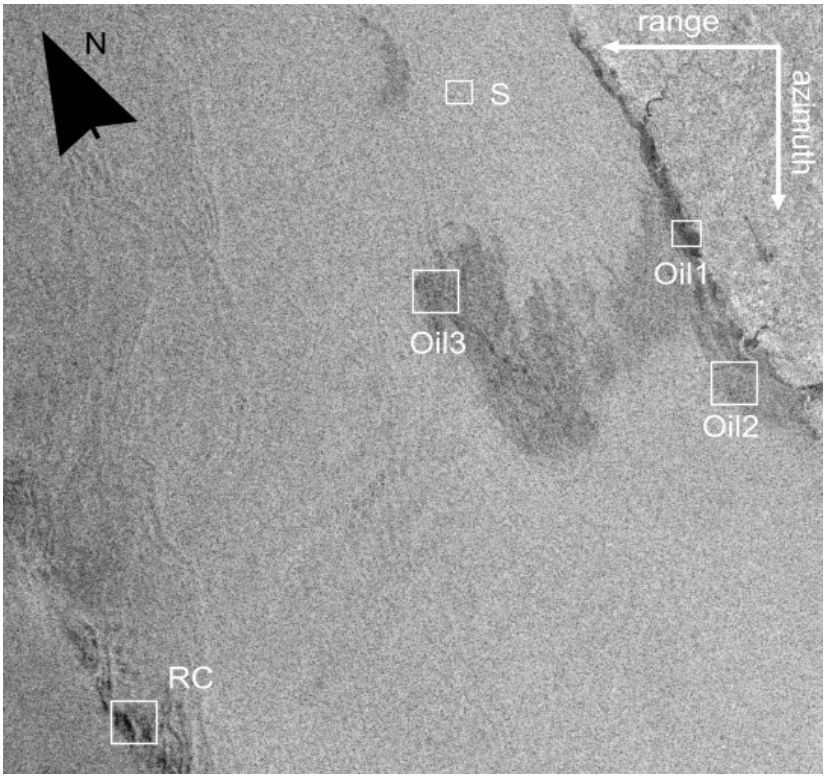

Fig. 3.5: Quicklook image of the area of interest relevant to the acquisition of 04 October 1994, 11:20 UTC (ERS-1, SLCI, orbit 16838, frame 2781, descending pass) and sketch of the ROIs selected for parameters estimation.

In this case Oil ROIs are relevant both to young and old spill and the scene is characterized by a high wind speed (>8 m/s) and by the presence of rain ([Int.3.2]). The experimental results are shown in Table 3.V. Physical results are in total agreement to former ones. In fact, $\eta_{\%}$ value is smaller for young oil spill (Oil1) and greater for older ones ([Int.3.2]).

TABLE 3.V
MEASURED GK PARAMETERS RELEVANT TO ROIS OF FIG. 3.5.

ROI	η	$\eta_{\%}$	α	$\Delta\alpha$	v	$v_{\%}$	Wind
Oil 1	0.0007019	-67.1	5	-12	0.02	0.0	High
Ref. Sea	0.002131		13		0.02		
Oil 2	0.001493	-30.7	16	-17	0.04	+100	High
Ref. Sea	0.002155		33		0.02		
Oil 3	0.001098	-43.3	4	-11	0.01	0.0	High
Ref. Sea	0.001935		15		0.01		
RC	0.0005270	-57.7	1	-20	0.03	0.0	Moderate
Ref. Sea	0.001245		21		0.03		
S	0.005527	+164	NA	-	0.35	+1650	High
Ref. Sea	0.002092		12		0.02		

In summary, the key physical results of this study can be identified as follows:

1. The GK pdf is a suitable model to describe marine SLC SAR images;
2. The three parameters $\eta_{\%}$, $\Delta\alpha$ and $v_{\%}$ are suitable descriptors of dark areas and areas with a dominant scatterer;
3. Dark areas are characterized by low and negative $\eta_{\%}$ values and negative $\Delta\alpha$ values;
4. This approach is not able to discriminate among the physical causes generating dark areas;
5. Dark areas due to oil slicks are characterized by $\eta_{\%}$ value related to the aging process;
6. Areas with a small and strong dominant scatterer are characterized by a positive and very high $\eta_{\%}$, value, an α value which can not be estimated and a very high and positive $v_{\%}$ value.

The approach is therefore able to detect even small dark areas and strong scatterers over full-resolution speckled SAR images.

References

Alpers W., D. Ross, and C. Rufenach, "On the Detectability of Ocean Surface Waves by Real and Synthetic Aperture Radar," *J. Geophys. Res.,* vol. 86, no. C7, pp. 6481-6498, 1981.

Apel J. R., "*Principles of Ocean Physics*". London, Academic Press: International Geophysics Series, 1990.

Barakat R., "Weak-Scatterer Generalization of the K-Density Function with Application to Laser Scattering in Atmospheric Turbulence," *J. Opt. Soc. Am. A*, vol. 3, no. 4, pp. 401-409, 1986.

Beckmann P. and A. Spizzichino. *"The Scattering of Electromagnetic Waves From Rough Surfaces"*. Norwood, MA: Artech House, 1963.

Brekke C., and A. H. S. Solberg, "Oil Spill Detection by Satellite Remote Sensing," *Remote Sens. Environ.*, vol. 95, no. 1, pp. 1-13, 2005.

Corona P., G. Ferrara, and M. Migliaccio, "Generalized Stochastic Field Model for Reverberating Chambers," *IEEE Trans. Electromagn. Compat.*, vol. 46, no. 4, pp. 655-660, 2004.

Corona P., G. Ferrara, and M. Migliaccio, "Reverberating Chambers as Sources of Stochastic Electromagnetic Fields," *IEEE Trans. Electromagn. Compat.*, vol. 38, no. 3, pp. 348-356, 1996.

Eltoft T. and K. A. Høgda, "Non-Gaussian Signal Statistics in Ocean SAR Imagery," *IEEE Trans. Geosci. Rem. Sensing*, vol. 36, no. 2, pp. 562-574, 1998.

Espedal H. A. and T. Wahl, "Satellite SAR Oil Spill Detection Using Wind History Information," *Int. J. Remote Sens.*, vol. 20, no.1, pp. 49-65, 1999.

Fetterer F., D. Generis, and C. C. Wackerman, "Validating a Scatterometer Wind Algorithm for ERS-1 SAR," *IEEE Trans. Geosci. Remote Sensing*, vol.36, no.2, pp.479-492, 1998.

Garello R., S. Proust and B. Chapron, "2D Ocean Surface SAR Images Simulation: A Statistical Approach," *Proc. OCEANS'93*, vol. 3, pp. 7-12, 1993.

Greco M., F. Bordoni, and F. Gini, "X-Band Sea-Clutter Nonstationarity: Influence of Long Waves," *IEEE J. Oceanic Eng.,* vol. 29, no. 2, pp. 269-283, 2004.

Herbach H., "CMOD5 An Improved Geophysical Function for ERS C-band Scatterometry," *ECMWF Technical Memorandum* 395, ECMWF, Reading, England, 2003.

Horstmann J., H. Schiller, J. Schultz-Stellenfelth, and S. Lehner, "Global Wind Speed Retrieval from SAR," *IEEE Trans. Geosci. Remote Sensing*, vol.41, no.10, pp.2277-2286, 2003.

Horstmann J. and W. Koch, "Measurement of Ocean Surface Winds Using Synthetic Aperture Radars," *IEEE J. Oceanic Eng.*, vol.30, no.3, pp.508-515, 2005.

Korsbakken E., J. A. Johannessen, and O. M. Johannessen, "Coastal Wind Field Retrievals from ERS Synthetic Aperture Radar Images," *J.Geophys. Res.*, vol.103, no.C4, pp. 7857-7874, 1998.

Jackson C. R. and J. R. Apel Editors. "*Synthetic Aperture Radar Marine Users Manual*". NOAA, Washington, DC, 2004.

Jakeman E., "On the Statistics of K-distributed Noise," *J. Phys. A*, vol. 13, no. 1, pp. 31-48, 1980.

Jakeman E. and P. N. Pusey, "A Model for Non-Rayleigh Sea Echo," *IEEE Trans. Antennas Propag.*, vol. 24, no. 6, pp. 806-814, 1976.

Jakeman E. and P. Tough, "Generalized K Distribution: A Statistical Model for Weak Scattering," *J. Opt. Soc. Am. A*, vol. 4, no. 9, pp. 1764-1772, 1987.

Joughin I. R., D. B. Percival, and D. P. Winebrenner, "Maximum Likelihood Estimation of K Distribution Parameters for SAR data," *IEEE Trans. Geosci. and Remote Sensing*, vol. 31, no.5, pp 989-999, 1993.

Lemaire D., *Non-fully Developed Sea State Characteristics from Real Aperture Radar Remote Rensing*, PhD Thesis, Université Catholique de Louvain, Louvain-la-Neuve, Belgium, 220 pp., 1998.

Maffett A. L. and C. C. Wackerman, "The Modified Beta Density Function as a Model for Synthetic Aperture Radar Clutter Statistics," *IEEE Trans. Geosci. Rem. Sensing*, vol. 29, no. 2, pp. 277-283, 1991.

Migliaccio M. and A. Reppucci, "A Review of Sea Wind Vector Retrieval by means of Microwave Remote Sensing," *Proc. European Microwave Association*, vol. 2, no. 1, pp. 136-140, 2006.

Wackermann C. C., C. L. Rufenach, R. A. Shuchman, J. A. Johannessen, and K. L. Davidson, "Wind Vector Retrieval Using ERS-1 Synthetic Aperture Radar Imagery," *IEEE Trans. Geosci. Remote Sensing*, vol.34, no. 6, pp.1343-1352, 1996.

Internet Sites:

[Int.3.1] http://ocean.dmi.dk/spill/FuShanHai/

[Int.3.2] http://www.rss.chalmers.se/rsg/Education/RSUM/

[Int.3.3] http://www.esa.int/esaEO/

Chapter 4: SAR Polarimetry to Observe Oil Spills

A study on sea oil spills observation by means of polarimetric Synthetic Aperture Radar (SAR) data is accomplished. The contribute is two-fold. The first contribute concern the use of a polarimetric Constant False Alarm Rate (CFAR) filter to detect dark patches over SAR images and the use of the Target Decomposition (TD) theorem to distinguish oil spills and look-alikes. In the second approach, the capability of the phase difference standard deviation value ($\sigma_{\varphi c}$) to distinguish among different dark features over marine polarimetric SAR images is investigated. The $\sigma_{\varphi c}$, evaluated between the co-polarized terms of the scattering matrix, needs only HH and VV data and can be applied also on dual-polarized SAR sensors such as the ASAR operated on board of the ENVISAT satellite. The $\sigma_{\varphi c}$ estimation has been performed through a simple and effective filter, which can assist oil spill classification. Experiments are conducted on polarimetric SAR data acquired during the SIR-C/X-SAR mission on April and October 1994. The data were processed and calibrated at NASA/JPL. Results show that new polarimetric approaches are able to assist classification.

4.1 Introduction

Nowadays, there is a general consensus that radar polarimetry is able to provide additional information for environmental remote sensing applications. Moreover, several Earth Observation satellite missions will carry on board polarimetric SARs. The main approved SAR missions are ALOS/PALSAR (2005, L-band), already in orbit, RADARSAT 2 (2007, C-band), TerraSAR-X (2007, X-band), COSMO/Skymed (2007, X-band), SAR-Lupe (2008, X-band). The main planned SAR missions are MAPSAR (2008, L-band), TerraSAR-L (2008, L-band), ECHO-L (2008, L-band), RADARSAT 3 (2009, C-band), TanDEM-X (2009, X-band). Some polarimetric airborne SAR sensors are to be mentioned: E-SAR of the DLR (P-, L-, C-, X-band), EMISAR of the DCRS (L-, C-band), RAMSES of the ONERA (P-, L-, C-, S-band) and the AIRSAR system of the NASA/JPL (P-, L-, C-band), now decommissioned.

Hence, all this has motivated the present studies over polarimetric SAR data to observe oil spills.

Only few oil spill detection studies, based on polarimetric SAR data, have been conducted in last years (Gade *et al.*, 1998; Fortuny-Guasch, 2003; Lombardo and Oliver, 2000). Before proceeding further, a brief summary of the state-of-art in oil spill detection by means of SAR polarimetry is due. In (Gade *et al.*, 1998) a detailed physical and experimental study on the SIR-C/X-SAR imaging of biogenic and anthropogenic films is reported. Results show that the damping behavior of the same substance is dependent on the wind speed. It is noted however that only slight differences in the damping behavior of different substances were measured by SIR-C/X-SAR. Further, in (Gade *et al.*, 1998), it is shown that C-band is more appropriate to observe biogenic and anthropogenic films with respect to L-band. With regards to the use of polarimetric SAR data it is shown that it is not possible discriminate among different surface films.

In (Fortuny-Guasch, 2003), a preliminary study on the use of the Anisotropy parameter (see section II), which is related to the Target Decomposition (TD) theorem (Cloude and Pottier, 1996), to improve oil spill detection is reported. The experimental study is developed making use of SIR-C/X-SAR images. A set of cases are presented and discussed. Among them a C-band data set, already examined in (Gade *et al.*, 1998), is used. Results suggest that polarimetric SAR data can enhance oil spill detection.

In (Lombardo and Oliver, 2000), a statistical and experimental study on oil spill detection with polarimetric SAR data is accomplished. A single SIR-C/X-SAR L-band data set is considered. It belongs to the data set used in (Gade *et al.*, 1998) and shows biogenic and anthropogenic films. The proposed polarimetric Maximum Likelihood filter is tested over different combinations of polarimetric information. It is shown that surface films detection by means of polarimetric SAR data better performs with respect to the best single channel data. No mention is made on the capability to discriminate among different surface films.

It is also interesting to mention some very recent papers on the matter (Schuler *et al.*, 2004; Schuler *et al.*, 2005). These studies use AIRSAR data and measure the sensitivity of entropy, anisotropy, and alpha values to Bragg wave Marangoni damping by the slicks as a function of the incidence angle (Schuler *et al.*, 2005) and the wave slope distributions and wave spectra in both the range and azimuth directions by combining measurements of the polarimetric orientation angle with the decomposition parameter alpha (Schuler *et al.*, 2004; Schuler and Lee, 2006). A classification algorithm, based on the polarimetric features and the complex Wishart Classifier is developed and tested. Applications include the mapping of surface features and, in particular, the unsupervised detection and characterization of spiral eddy features embedded in a biogenic slick-field.

In this chapter, two polarimetric approaches to observe oil spill in SAR images are presented. The first approach combines the use of a Constant False Alarm Rate (CFAR) filter for polarimetric SAR data adapted from (Schou *et al.*, 2003) to best identify the ROIs and the use of the TD theorem to assist oil spill classification. It is important to note that this approach can be nested into a classical procedure (Brekke and Solberg, 2005). Therefore, in a operational implementation is expected to extract also classical, i.e. non-polarimetric, features.

The second approach concern the standard deviation of the phase difference ($\sigma_{\varphi c}$). The $\sigma_{\varphi c}$, which has been used for classifying different agricultural field (Mattia *et al.*, 1997; Ulaby *et al.*, 1987; Ulaby *et al.*, 1992), is shown to be useful to assist oil spill detection. In detail, the capability of $\sigma_{\varphi c}$ for distinguishing among different dark features over marine polarimetric SAR images is investigated. Moreover, since $\sigma_{\varphi c}$ needs only HH and VV data, it can be applied also on dual-polarized SAR sensors such as the ASAR operated on board of the ENVISAT satellite.

Experiments are conducted on SIR-C/X-SAR C-band data including features related to oil spills and biogenic look-alikes. Results show that the polarimetric SAR approaches are able to effectively identify the ROIs and to assist classification.

4.2 Radar Polarimetry Background

In this paragraph the radar polarimetry background theory is provided. Full polarimetric SAR sensors are able to measure the complete 2x2 scattering matrix **S**:

$$\mathbf{S} = \begin{bmatrix} S_{hh} & S_{hv} \\ S_{vh} & S_{vv} \end{bmatrix} \quad , \tag{4.1}$$

where the first subscript stands for the transmitted polarization, either horizontal or vertical, and the second one for the received. In the monostatic case, the reciprocity theorem dictates that the cross-polarized terms are equal, i.e. $S_{hv}=S_{vh}$.

It is useful to vectorize **S**. This can be accomplished either by making use of the lexicographic decomposition and by the Pauli one (Cloude and Pottier, 1996; Conradsen *et al.*, 2003):

$$\boldsymbol{k}_L = \begin{bmatrix} S_{hh} & \sqrt{2}S_{hv} & S_{vv} \end{bmatrix}^T \quad , \tag{4.2}$$

$$\boldsymbol{k}_P = \frac{1}{\sqrt{2}} \begin{bmatrix} S_{hh} + S_{vv} & S_{hh} - S_{vv} & 2S_{hv} \end{bmatrix}^T \quad , \tag{4.3}$$

where the symbol T stands for the transpose operator. Accordingly, the covariance matrix **C** and the coherence matrix **T** are obtained by averaging the outer product of $\boldsymbol{k}_L$ and $\boldsymbol{k}_P$ vectors with their transpose conjugate (or adjoint vector), respectively (Conradsen *et al.*, 2003):

$$\mathbf{C} = \left\langle \boldsymbol{k}_L \boldsymbol{k}_L^{\dagger} \right\rangle = \begin{bmatrix} \left\langle |S_{hh}|^2 \right\rangle & \sqrt{2}\left\langle S_{hh} S_{hv}^* \right\rangle & \left\langle S_{hh} S_{vv}^* \right\rangle \\ \sqrt{2}\left\langle S_{hv} S_{hh}^* \right\rangle & \left\langle |S_{hv}|^2 \right\rangle & \sqrt{2}\left\langle S_{hv} S_{vv}^* \right\rangle \\ \left\langle S_{vv} S_{hh}^* \right\rangle & \sqrt{2}\left\langle S_{vv} S_{hv}^* \right\rangle & \left\langle |S_{vv}|^2 \right\rangle \end{bmatrix} , \tag{4.4}$$

$$\mathbf{T} = \left\langle \boldsymbol{k}_P \boldsymbol{k}_P^{\dagger} \right\rangle = \frac{1}{2} \begin{bmatrix} \left\langle |S_{hh} + S_{vv}|^2 \right\rangle & \left\langle (S_{hh} + S_{vv})(S_{hh} - S_{vv})^* \right\rangle & 2\left\langle (S_{hh} + S_{vv}) S_{hv}^* \right\rangle \\ \left\langle (S_{hh} - S_{vv})(S_{hh} + S_{vv})^* \right\rangle & \left\langle |S_{hh} - S_{vv}|^2 \right\rangle & 2\left\langle (S_{hv} - S_{vv}) S_{hv}^* \right\rangle \\ 2\left\langle S_{hv} (S_{hh} + S_{vv})^* \right\rangle & 2\left\langle S_{hv} (S_{hh} - S_{vv})^* \right\rangle & 4\left\langle |S_{hv}|^2 \right\rangle \end{bmatrix} \tag{4.5}$$

where $\langle \cdot \rangle$ indicates the ensemble average and † stand for transpose conjugate. Note that both **C** and **T** are Hermitian by definition. More important to note is the unambiguous relationship between **T** and the Muller matrix **M** (Cloude, 1986) he most general representation of a complex polarimetric scattering process (Conradsen *et al.*, 2003). **T** can be unambiguously associated to a decomposition into elementary polarimetric scattering mechanisms (Cloude and Pottier, 1996). As a matter of fact, under unitary transformation in the complex space, it is possible to rewrite the coherence matrix as follows (Cloude and Pottier, 1996):

$$\mathbf{T} = \mathbf{U} \boldsymbol{\Lambda} \mathbf{U}^{-1} \quad , \tag{4.6}$$

where **Λ** is a 3x3 diagonal matrix whose elements are the real non-negative eigenvalues of **T**, with $\lambda_1 \geq \lambda_2 \geq \lambda_3$ and $U = [\boldsymbol{e}_1 \ \boldsymbol{e}_2 \ \boldsymbol{e}_3]$ is a 3x3 unitary matrix in which:

$$\boldsymbol{e}_i = \begin{bmatrix} \cos\alpha_i \exp(j\phi_{1i}) \\ \sin\alpha_i \cos\beta_i \exp(j\phi_{2i}) \\ \sin\alpha_i \sin\beta_i \exp(j\phi_{3i}) \end{bmatrix} \tag{4.7}$$

are the eigenvectors of **T**.

Therefore, the coherence matrix **T** can be rewritten as follows (Cloude and Pottier, 1996):

$$\mathbf{T} = \sum_{i=1}^{3} \lambda_i \boldsymbol{e}_i \boldsymbol{e}_i^{\dagger} \quad . \tag{4.8}$$

Equation (4.8) physically states that **T** can be decomposed as a non-coherent sum of three independent elementary polarimetric mechanisms (Cloude and Pottier, 1996). Further, three compact physical parameters can be defined. The entropy *H*, measures the randomness of the complex polarimetric scattering process (Hajnsek *et al.*, 2003). It can be also interpreted as a degree of statistical disorder and is defined as follows:

$$H = -\sum_{i=1}^{3} p_i \log_3 p_i \quad , \tag{4.9}$$

where p_i values are given by:

$$p_i = \frac{\lambda_i}{\lambda_1 + \lambda_2 + \lambda_3} \quad . \tag{4.10}$$

The case of pure polarization states, i.e. single elementary polarimetric mechanism, is characterized by H=0, while the total depolarization case is characterized by H=1. All other cases are characterized in the range 0-1. Note that (4.9) is consistent with the entropy definition in Von Neuman sense (Kinchin, 1957).

The mean scattering angle $\hat{\alpha}$ physically provides information about the isotropy of the scattering process (Cloude and Pottier, 1996) and is defined as follows:

$$\hat{\alpha} = p_1\alpha_1 + p_2\alpha_2 + p_3\alpha_3 \quad . \tag{4.11}$$

where $\hat{\alpha}$ ranges within 0°-90° and 0° characterizes an isotropic surface.

The anisotropy *A*, measuring the difference between the secondary polarimetric scattering mechanisms, is defined as follows (Hajnsek *et al.*, 2003):

$$A = \frac{\lambda_2 - \lambda_3}{\lambda_2 + \lambda_3} \quad . \tag{4.12}$$

Anisotropy A provides complementary information with respect to H and is expected to be of particular significance for low and medium H values. It can be exploited to estimate surface roughness (Cloude, 1986).

In studies of ocean, marine scenes have as been regarded as a low entropy surface dominated by the return from tilted-Bragg scatterers (Schuler and Lee, 2006; Schuler *et al.*, 2003). In fact, the free surface backscatter is dominated by Bragg scatter measured by the first eigenvalue while the return from slick covered surface is due to multiple scattering mechanism of comparable strength (Schuler *et al.*, 2003). The average alpha angle indicates the type of scattering mechanism that is dominant. Anisotropy, may be regarded as a parameter measuring small-scale surface roughness (Schuler and Lee, 2006; Schuler *et al.*, 2002). For ocean scatter, at L- and C-bands, A is determined by centimetric wavelength Bragg scatter and do not depend on long wave tilting (Schuler *et al.*, 2003). Moreover, H, α and A are roll invariant variables. Anisotropy is, additionally, invariant in the azimuth direction and the range direction and independent of changes in the dielectric constant (Schuler and Lee, 2006). All these aspects have motivated the choice of H, $\hat{\alpha}$ and A in this study.

4.2.1 Phase Difference

Each complex element of the scattering matrix and can be written as:

$$S_{pq} = |S_{pq}| e^{j\varphi_{pq}} \quad p,q = h,v \quad . \tag{4.13}$$

Thus, the scattering matrix, shown in Eq. 4.1, can be re-written as:

$$\mathbf{S} = e^{j\varphi_{vv}} \begin{bmatrix} S_{hh} e^{j\varphi_c} & S_{hv} e^{j\varphi_x} \\ S_{hv} e^{j\varphi_x} & S_{vv} \end{bmatrix} \quad , \tag{4.14}$$

where $\varphi_x = \varphi_{hv} - \varphi_{vv} = \varphi_{vh} - \varphi_{vv}$ and $\varphi_c = \varphi_{hh} - \varphi_{vv}$ are the cross- and the co-polarized phase angles, respectively.

When a polarimetric SAR illuminates an area of a sea surface many scatters point contribute to the total scattered electric field received by the SAR antenna, thus each scattering amplitudes can be written as:

$$S_{pq} = \sum_{n=1}^{N} |S_{pq}^{n}| e^{j\varphi_{pq}^{n}} \quad . \tag{4.15}$$

Hence, under the hypothesis of strong scattering regime (Oglivy, 1991), the pdf of each phase angle φ_{pq} is uniformly distributed over [-π π] and therefore does not contain informations about the scene geometrical and dielectric properties. However, their phase differences φ_x and φ_c may not be uniformly distributed and thus can be related to the scene properties. In particular while the pdf of φ_x is usually uniformly distributed over [-π π], the pdf of φ_c is approximately Gaussian in shape (Joughin *et al.*, 1994; Lee *et al.*, 1994; Ulaby *et al.*, 1992) and its mean and standard deviation, $m_{\varphi c}$ and $\sigma_{\varphi c}$, respectively, are related to the scene properties. However, whereas both $m_{\varphi c}$ and $\sigma_{\varphi c}$ exhibit variations with surface roughness, incidence angle and wavelength, the variation of $m_{\varphi c}$ are relatively smaller than $\sigma_{\varphi c}$ ones (Ulaby *et al.*, 1992). The latter can be regarded as a measure of the degree of correlation between the co-polarized components of the scattering matrix (Ulaby *et al.*, 1992). As a matter of fact, $\sigma_{\varphi c}=0^{\circ}$ corresponds to a total correlation between the two co-polarized scattering amplitudes, thus the pdf of φ_c approaches to a Dirac delta function. $\sigma_{\varphi c}>100^{\circ}$ is representative of a total uncorrelation and the pdf of φ_c approaches to a uniform distribution (Ulaby *et al.*, 1992).

4.3 The Polarimetric Filter

In this section the polarimetric filter employed to semi-automatically detect dark patches, i.e. possible oil spills, over polarimetric SAR images is presented.

The filter belongs to the class of CFAR (Schou *et al.*, 2003) filters and its rationale is summarized hereafter. It makes use of the covariance matrix **C** and of the underlying complex Wishart distribution $W(\cdot,\cdot,\cdot)$ (Schou *et al.*, 2003). In practice, once that a pixel is considered and two adjacent non-overlapping areas are defined (Fig. 4.1), a test of hypothesis can be applied over the associated polarimetric data. If the test of hypothesis is rejected the pixel is labeled as edge.

In particular, reference is made to the average covariance matrices $\mathbf{Z}_1$ and $\mathbf{Z}_2$ associated to the two non-overlapping areas which follows the complex Wishart distribution, i.e. $\mathbf{Z}_1 \sim W(p,L,\mathbf{\Sigma}_1)$ and $\mathbf{Z}_2 \sim W(p,L,\mathbf{\Sigma}_2)$ where p is the dimensionality of **Z** (and **C**) and equal to 3 in our case, L is the effective number of look (Franceschetti and Lanari, 1999) and $\mathbf{\Sigma}$ in the mean values matrix. The null hypothesis H_0 corresponds to the presence of only clutter where $\mathbf{\Sigma}_1=\mathbf{\Sigma}_2$.

In detail, the test of hypothesis is based on the evaluation of the function $-2\rho\log Q$ whose asymptotic distribution is given by (Van Zyl *et al.*, 1987):

$$\begin{aligned} p\{-2\rho\log(Q) \le T_f\} &= -p\{\chi^2(f) \le T_f\} + \\ &+ \omega\left[P\{\chi^2(f+4) \le T_f\} - p\{\chi^2(f) \le T_f\}\right] \end{aligned} \quad , \tag{4.16}$$

where $p\{\cdot\}$ is for probability and $\chi^2(\cdot)$ is the chi-squared distribution, T_f is the reference threshold value and

$$f = p^2 \quad , \tag{4.17}$$

$$\rho = 1 - \frac{2p^2-1}{6p}\left(\frac{3}{2L}\right) \quad , \tag{4.18}$$

$$\omega = -\frac{f}{4}\left(1-\frac{1}{\rho}\right)^2 + \left(\frac{f(f-1)}{24}\right)\left(\frac{2}{L^2}-\frac{1}{(2L)^2}\right)\frac{1}{\rho^2} \quad , \tag{4.19}$$

where:

$$Q = 2\frac{|\mathbf{Z}_1|^L |\mathbf{Z}_2|^L}{|\mathbf{Z}_1+\mathbf{Z}_2|^{2L}} \tag{4.20}$$

and $|\cdot|$ stands for the determinant operator (Schou *et al.*, 2003).

Ideally the filter must be applied in all the possible directions. In practice, four windows are considered, see Fig. 4.1. The Q value is computed for each directions. The minimum Q value ($Q_{\min}$), corresponding to the most probable edge direction, is considered.

The probability of false alarm P_{fa} is related to the threshold T_f value according to the following relationship (Schou *et al.*, 2003):

$$\begin{aligned} & p\{-2\rho\log(Q_{\min}) \le T_f\} \simeq \\ & \simeq \left(P\{\chi^2(f) \le T_f\} + \omega\left[P\{\chi^2(f+4) \le T_f\} - P\{\chi^2(f) \le T_f\}\right]\right)^4 \equiv 1 - P_{fa} \end{aligned} \tag{4.21}$$

.

Two important points deserve special care.

The test of hypothesis summarized before can be usefully applied also on incomplete covariance matrices, e.g. targets with azimuthal symmetry (Schou *et al.*, 2003). Note that, if we force the sample **C** into the azimuthal symmetry case it does not follow exactly the complex Wishart distribution but the test statistic is still enforceable (Conradsen *et al.*, 2003). In particular, two incomplete covariance cases are of special interest (Schou *et al.*, 2003): the azimuthal and the diagonal configurations. Application to such cases of the polarimetric filter calls for a modification of Q (Schou *et al.*, 2003).

Let us now consider the threshold choice. Physically T_f depends on the nature of the surface films, local wind field, sea state (Brekke and Solberg, 2005). Unfortunately, these latter data are not generally available and when available are often at different scale and/or not collocated. In practice, T_f is set by means of rule of thumbs. Although this may sound rough it operationally ensures good results (Brekke and Solberg, 2005). For reader completeness it

must be noted however that some pioneering alternative approaches have been proposed in (Espedal and Wahl, 1999; Migliaccio *et al.*, 2005; Solberg *et al.*, 1999).

In this study the T_f is empirically set once that the filtering window size is objectively determined by means of an imagery homogeneity analysis. The scene homogeneity, which is physically dependent on the wind speed, is measured following the guidelines detailed in (Horstmann *et al.*, 2003). In practice, 20 WxW sub-images of the span image are considered to estimate the mean and the variance of the periodogram *PG*. The parameter ς_W is given by:

$$\varsigma_W = \sum_{k=1}^{20} \frac{\mathrm{var}(PG_k)}{\mathrm{mean}(PG_k)} \Big/ \sum_{k=1}^{20} \mathrm{mean}(PG_k) \quad , \tag{4.22}$$

The filtering window size selected corresponds to the smallest sub-images size for which ς_W is greater than 2.4.

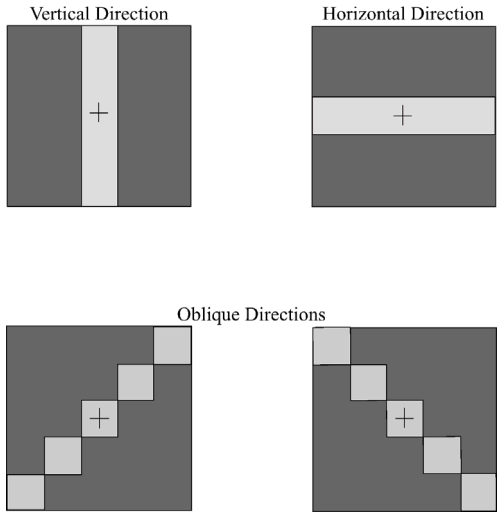

Fig. 4.1. Relevant to oil spill CFAR filter. + indicates the application point, the two dark zones are the non-overlapping regions.

4.4 The Polarimetric Technique for Oil spill Detection

In this paragraph the polarimetric semi-automatic technique for oil spill detection in SAR images is applied over C-Band SAR data acquired during the SIR-C/X-SAR mission in September-October 1994.

The technique can be usefully framed into two phases:

1. Identification of ROIs by means of polarimetric CFAR filtering.
2. Polarimetric feature extraction by means of TD.

Note that in this paper emphasis is on polarimetric features but phase 1 also allows extracting classical and effective features (Brekke and Solberg, 2005). Therefore, the polarimetric features can be meant to assist a classical oil spill detection procedure (Brekke and Solberg, 2005).

4.4.1 SIR-C/X-SAR mission and data calibration

The SIR-C/X-SAR mission was the first mission in which a multifrequency/multipolarization imaging radar system has been flown in the space. SIR-C/X-SAR flew on space shuttle Endeavour on mission STS-59 April 9-20, 1994 and on mission STS-68 September 30 - October 11, 1994. The Endevour missions are also commonly designated the Space Radar Laboratory-1 (SRL-1) and -2 (SRL-2) respectively ([Int.4.1]). The SAR system was designed and built to make eight different polarimetric measurements at the same time: L-Band and C-Band backscatter in the full-polarimetric configuration, i.e. all the elements of the scattering matrix **S** are measured. Moreover, X-band SAR data were acquired in the VV polarization channel.

The data set used in this study was acquired during the SRL-2 SIR-C/X-SAR mission. Compressed data products (CDP) are multi-look complex (MLC); they have been processed and calibrated at NASA/JPL by processing software version 3.0.2. (Freeman, 1992; Freeman *et al.*, 1995; Sarabandi *et al.*, 1995). The incidence angle varied between 20-55 degrees and the SAR swath width on the ground varied between 15 Km and 90 Km ([Int.4.1]). The noise floor at L and C bands was -36dB and -28dB respectively. The interested reader can find much more detail about SIR-C/X-SAR mission in (Freeman, 1992; Freeman *et al.*, 1995; Sarabandi *et al.*, 1995).

4.4.2 Oil spill detection

The oil spill detection is applied to two meaningful cases. The first case is relevant to the SAR data acquired at 08:12:44.032 GMT on October 6, 1994 over the English Channel. In Fig. 4.2(a) is shown the total power image, in which the presence of an oil spill is highlighted by the white box. No information about the type of oil is reported in literature (Fortuny-Guasch, 2003). The estimated wind speed in the area of interest at 08 October 1994 06:00:00, was provided by ECMWF data service (ERA40 data set), is 4-5 m/s and in 170 degrees North. In order to study the relevance of the polarimetric data, phase 1 has been also applied over incomplete **C** matrices. In fact, the polarimetric CFAR filtering has been run over the full, azimuthal and diagonal configurations. Further, the ratio of averages (ROA) CFAR filter (Touzi *et al.*, 1988) over the VV polarization channel has been run for comparative purposes. In all cases a 13x13 pixel filter window has been fixed, see paragraph 4.2. In Fig. 4.2(b)-(e), the results relevant to the polarimetric and ROA filterings are shown.

Results show that polarimetric filtering is more accurate that the non polarimetric one. In fact, the polarimetric CFAR filtering ensures a better definition of the ROI boundary and much less outliers. Among the three polarimetric filterings we have that the full configuration and the azimuthal one get similar results while the diagonal one get poorer results.

It is also important to compare the computer processing times at the present software version: if we say 1 the time to process the non-polarimetric data. i.e. the VV-pol data, relevant to the 15.8 Km x 11 Km area, the processing times become 6.5, 8 and 9 for the diagonal, azimuthal and full polarimetric configurations. This is obviously due to the larger volume of data to be processed and to the complexity of the polarimetric CFAR filter. It is important to remark that a better phase 1 facilitates the extraction of the geometrical features and this is very much advisable for classification purposes (Brekke and Solberg, 2005).

Once that the phase 1 has identified the ROIs, phase 2 can be operated over the ROIs. The key polarimetric features are H, $\hat{\alpha}$ and A which are plotted in Fig. 4.3. In particular, the polarimetric features shown are relevant to the oil-covered area, i.e. the ROI, and to an adjacent oil-free area. These plots show the values of H, $\hat{\alpha}$ and A in the 3D space and their H/α plane projections (gray clouds).

To detail the features behavior in Fig. 4.4 the pdf of H, $\hat{\alpha}$ and A are shown (from left to right). Solid line with dots corresponds to the oil-covered area

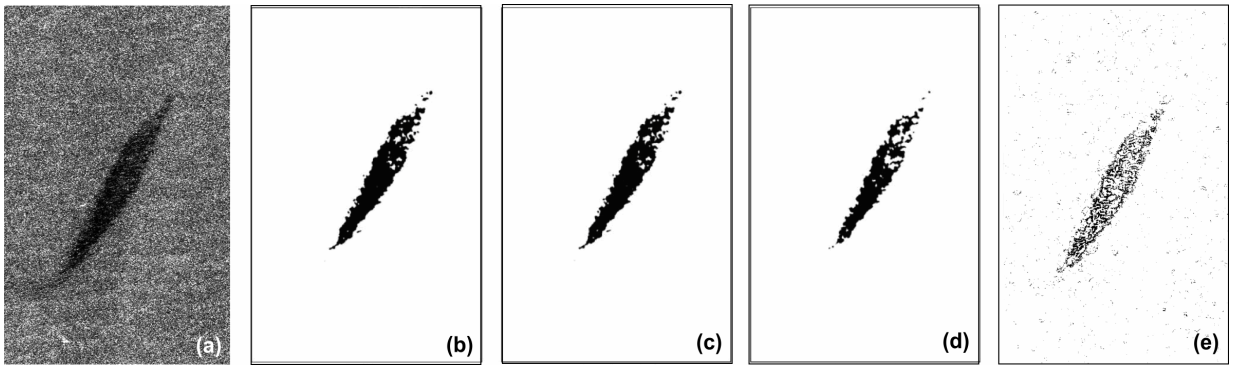

Fig. 4.2. SAR image relevant to total power SIR-C/X-SAR image acquired at C-band, on October 8, 1994 over the English Channel. Scene identifier E66, site name Therford - England, GMT at image center 05:57:36.942, lat. at image center 52.9005547, lon. at image center 2.4576561, looks number 4.76, ascending pass, processed range 21 Km, processed azimuth 106 Km. (a) total power image, polarimetric CFAR (b) full matrix configuration, (c) azimuthal configuration, (d) diagonal configuration, (e) ROA CFAR processing.

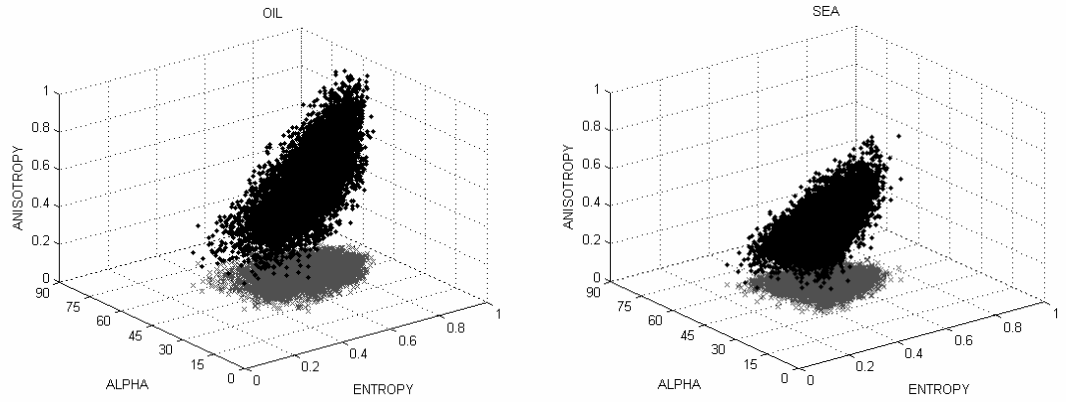

Fig. 4.3. $H/\bar{\alpha}/A$ plots for oil-covered and oil-free sea surface relevant to Fig. 1(a). The grey clouds show the $H/\bar{\alpha}$ plane projections.

while the thick solid line to the oil-free area. The H and A pdfs are always separable, i.e. distinguishable, while $\bar{\alpha}$ pdfs are similar. This is also witnessed by the mean and the standard deviation values reported in Table 4.I. The mean difference for $H(A)$ is equal to 16% (18%) while the mean difference for α is only 0.1%. Standard deviation values are much more similar. To further investigate all this, in Fig. 4.5 the normalized moments (NM) from 1 to 10, in semi-logarithmic scale, are shown. Circles (o) correspond to the oil-covered area while plus (+) to the oil-free area. Comparative analysis of NMs show that oil free and oil covered areas are similar in terms of H and different in terms of $\bar{\alpha}$ and A. These results are in accordance with what experienced in (Fortuny-Guasch, 2003; Schuler *et al.*, 2004; Schuler and Lee, 2006). In fact, it is found that the capability to distinguish among oil-covered and oil-free areas is based on the H and A features under low wind conditions.

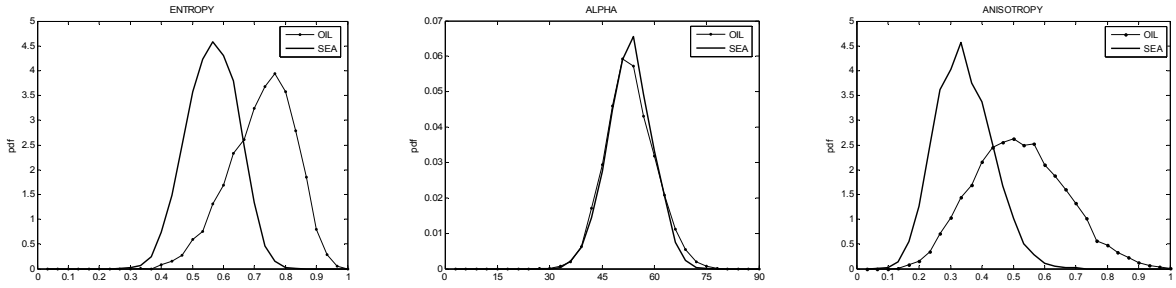

Fig. 4.4: Pdfs of H, $\tilde{\alpha}$ and A relevant to oil-covered (solid line with dots) and oil-free sea surface (thick line).

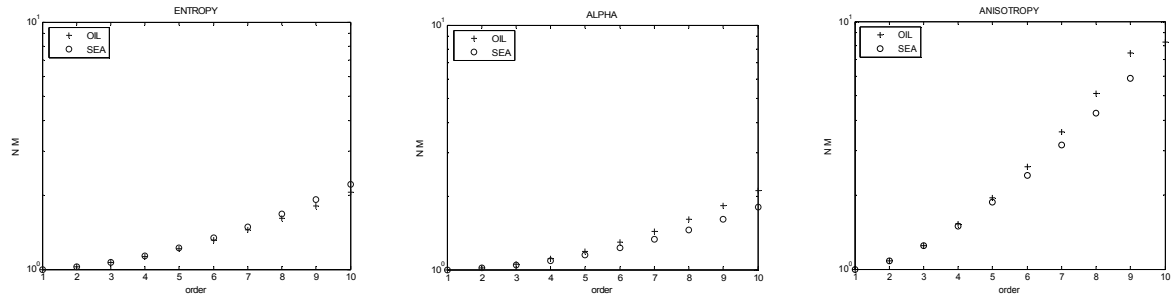

Fig. 4.5: Normalized moments of H, $\tilde{\alpha}$ and A relevant to oil-covered (+) and oil-free sea surface (o).

TABLE 4.I
MEAN AND STD VALUES OF H, $\tilde{\alpha}$ AND A
FOR OIL COVERED AND OIL FREE SEA SURFACE
RELEVANT TO THE ENGLISH CHANNEL SAR DATA

	MEAN		**STD**	
	OIL	SEA	OIL	SEA
H	0.706	0.547	0.104	0.0804
$\tilde{\alpha}$	51.63	51.49	6.950	6.280
A	0.503	0.327	0.1431	0.0846

The second case is relevant to the experiment conducted by the University of Hamburg described in (Gade *et al.*, 1998). In this experiment were deployed artificial biogenic films and a mineral oil spill consisting of heavy fuel (IFO 180). The corresponding SAR data were acquired on October 11, 1994 over the German Bight of the North Sea. The area interested by the experiment is shown in Fig. 4.6a where the seven slick-covered areas can be visually identified. From left to right the surface films are due to IFO 180, oleyl alcohol (OLA), oleic acid methyl ester (OLME), triolein (TOLG), TOLG spread with the help of *n*-hexane, OLME

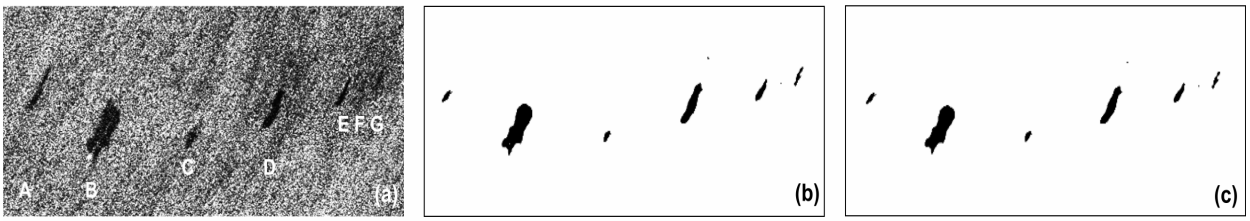

Fig. 4.6: SAR image relevant to total power SIR-C/X-SAR image acquired at C-band, on October 11, 1994 over the German Bight - North Sea. Scene identifier NBA, site name North Sea A0, GMT at image centre 08:12:44.032, lat. at image centre 54.9365158, lon. at image centre 8.3916855, looks number 4.59, descending pass, processed range 21 Km, processed azimuth 106 Km. (a) total power image, polarimetric CFAR (b) full matrix configuration, (c) azimuthal configuration.

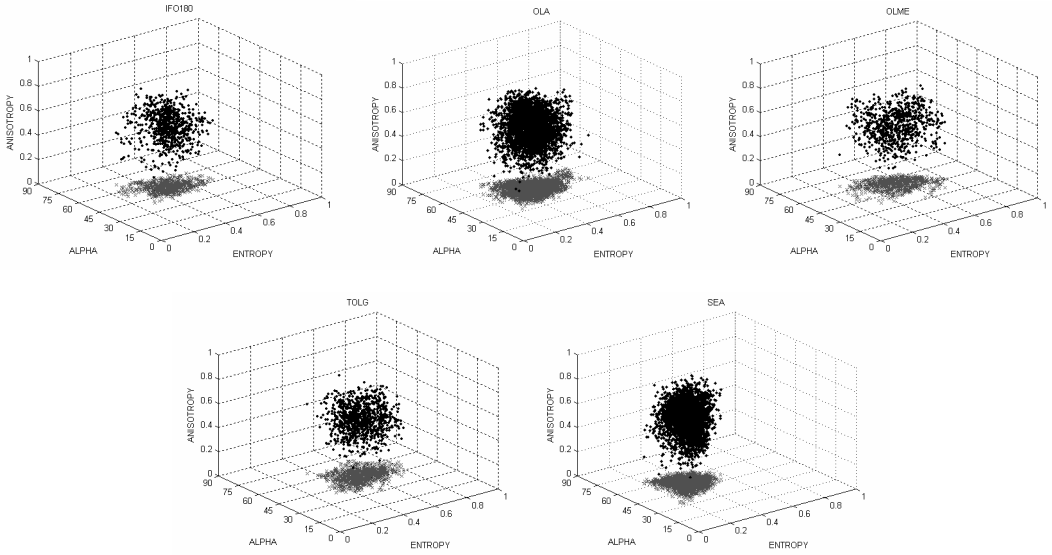

Fig. 4.7: $H/\hat{\alpha}/A$ plots for the ROIs A, B, C, D and slick-free sea surface relevant to Fig. 5(a). The grey clouds show the $H/\hat{\alpha}$ plane projections.

spread with the help of *n*-hexane and OLME spread with the help of ethanol, respectively (Gade *et al.*, 1998). In order to better identify the seven slicks we label them from left to right as A, B, C, D, E, F and G. The measured wind speed in the area of interest is 12 m/s and in 210 degrees North. The polarimetric CFAR filter is applied in the full and azimuthal configuration and a 17x17 pixel filter window is used. Result are shown in fig 4.6(b)-(c) and are in agreement with the ones found in the former case. We note however that, even in the full configuration the slick labeled as F, due to its small size, is not detected. Similar result was found in (Gade *et al.*, 1998). The polarimetric features H, $\hat{\alpha}$ and A are plotted in Fig. 4.7 for the ROIs A to D, and an slick-free area.

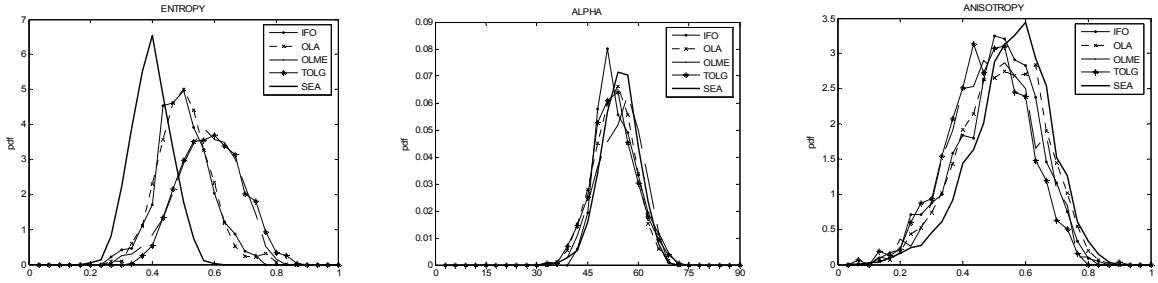

Fig. 4.8. Probability density functions of H, $\hat{\alpha}$ and A relevant to IFO 180 (solid line with dots), OLA (dashed line with crosses), oil spill (solid line with dots), OLME (dashed-dotted line), TOLG (solid line with asterisks) and slick-free sea surface (thick line).

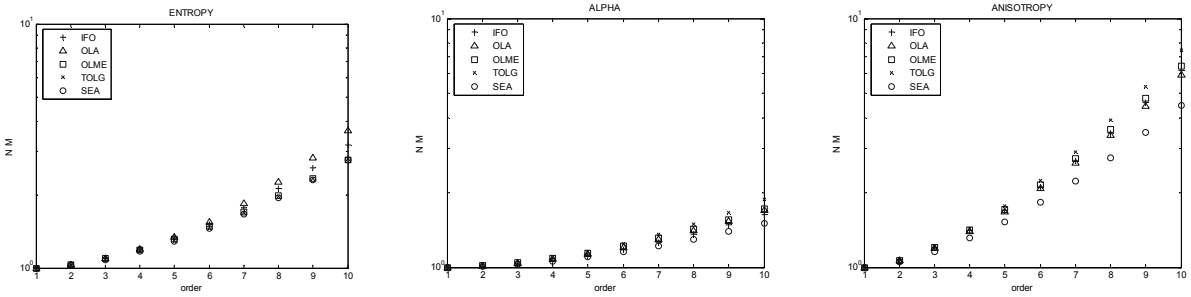

Fig. 4.9. Normalized moments of H, $\hat{\alpha}$ and A relevant to the A ROI (+), the B ROI (Δ), the C ROI (□), the D ROI (**X**) and the slick-free area (o).

TABLE 4.II
MEAN AND STD VALUES OF H, $\hat{\alpha}$ AND A
FOR A, B, C, D SLICKS AND SLICK-FREE SEA SURFACE
RELEVANTTO THE GERMAN BIGHT SAR DATA

	MEAN				
	IFO	OLA	OLME	TOLG	SEA
H	0.484	0.488	0.558	0.574	0.379
$\hat{\alpha}$	52.00	51.37	53.12	53.12	52.97
A	0.491	0.507	0.507	0.481	0.534
	STD				
	IFO	OLA	OLME	TOLG	SEA
H	0.0847	0.0846	0.0995	0.0969	0.0628
$\hat{\alpha}$	5.486	5.937	6.409	6.350	5.412
A	0.130	0.131	0.126	0.125	0.124

These plots show the values of H, $\hat{\alpha}$ and A in the 3D space and their H/α plane projections (gray clouds). The polarimetric study is focused on these four ROIs for the physical reasoning detailed in (Gade *et al.*, 1998). Visual analysis of these 3D plots show only some differences which can be better read by means of the H, $\hat{\alpha}$ and A pdfs shown in Fig. 4.8. Solid line with dots corresponds to the A ROI, the dashed line with crosses corresponds to the B ROI, the

dashed-dotted line corresponds to the C ROI, the solid line with asterisks corresponds to the D ROI and the thick solid line to the slick free area. In this case we have that H of the slick free area is distinguishable by slick covered ones although IFO180 and OLA are indistinguishable in terms of their H pdfs as OLME and TOLG. α pdfs are very similar while A pdfs are somehow different. This is also witnessed by the mean and the standard deviation values reported in Table 4.II where we find that the mean difference between the slick free area and the A or B ROIs for $H(A)$ is equal to 10%(4%) while the mean difference between the slick free area and the C or D ROIs for $H(A)$ is equal to 18%(5%). Similarly to the English Channel data, in all cases α mean values and the standard deviation values are almost identical. In this case, the use of NMs is not straightforward, see Fig. 4.9. These results are still in accordance to what found in (Fortuny-Guasch, 2003; Schuler *et al.*, 2004; Schuler and Lee, 2006). Therefore we can say that the capability to distinguish among slick covered and slick free areas is mainly based on H even at high wind regimes.

4.5 The Phase Difference Filter

In this paragraph, the filtering technique based on the standard deviation of the co-polar phase difference is presented.

Some meaningful experiments, made on SIR-C/X-SAR C-band SAR images, allows demonstrating the capability of $\sigma_{\varphi c}$ to assist oil spill detection. For each case the $\sigma_{\varphi c}$ is evaluated according to a simple and effective filter. The filtering is performed by means of a 7x7 moving window and the output is a gray scale $\sigma_{\varphi c}$ image with the same size of the input data.

The five cases considered are relevant to three oil spills and two look-alikes regarding low and moderate wind conditions. In Fig. 4.10a a cut of the SAR total power image, acquired under low wind conditions on 01-10-94 at 05:33, is shown. A dark patch relevant to an OLA spill is clearly visible. OLA produces a mono-molecular film which can be regarded as a biogenic oil look-alike (Gade *et al.*, 1998). In Fig. 4.10b the corresponding gray scale $\sigma_{\varphi c}$ image is shown. In this case the filtering result is quite homogeneous thus do not allow highlighting the presence of the OLA. Fig. 4.11a shows a cut of the SAR total power image,

relevant to an OLA, acquired under moderate wind conditions on 15-04-94 at 02:14. As in the previous case the $\sigma_{\varphi c}$ image, shown in Fig. 4.11b, do not allow to distinguish the OLA.

In Figs. 4.12-4.13 three oil spills acquired under low wind conditions are shown. Fig. 5.12a is relevant to the case shown in Fig. 4.2a. Fig. 4.13a is relevant to a cut of the SAR total power image, acquired on 11-04-94 at 10:49. In this case two oil spills, due to the presence of oil rigs, are clearly visible. The corresponding $\sigma_{\varphi c}$ images are shown in Figs. 4.12b-4.13b. Filtering results show a good sensitivity of $\sigma_{\varphi c}$ values to oil spills.

In the last case, shown in Fig. 4.14, an oil spill under moderate wind conditions is considered. Fig. 4.14a shows the total power cut relevant acquired on 01-10-94 at 08:14. As in the previous case the $\sigma_{\varphi c}$ image allows highlighting the presence of the oil spill.

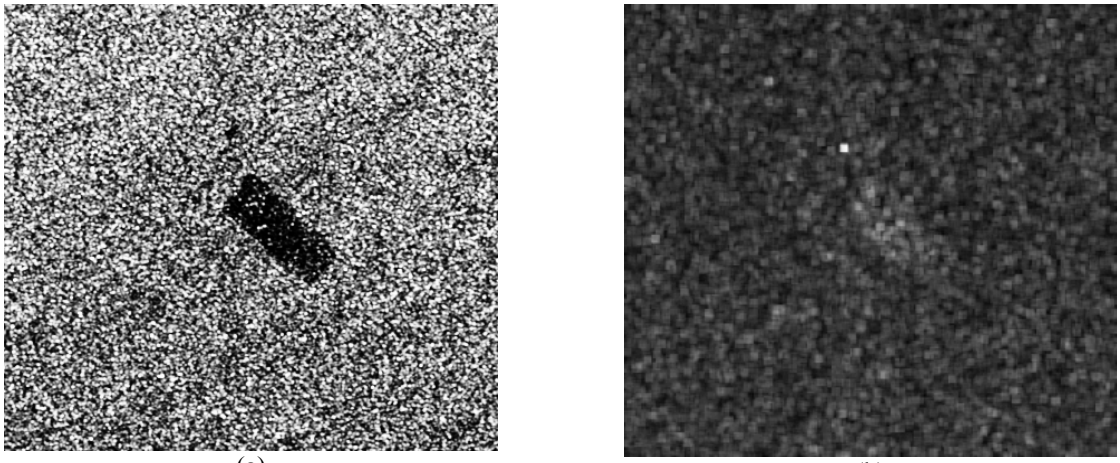

(a) (b)

Fig. 4.10: Total power (a) and standard deviation of the co-polar phase difference (b) relevant to the SIR-C image acquired on 01-10-94 at 05:33 in which a biogenic film (OLA) is present.

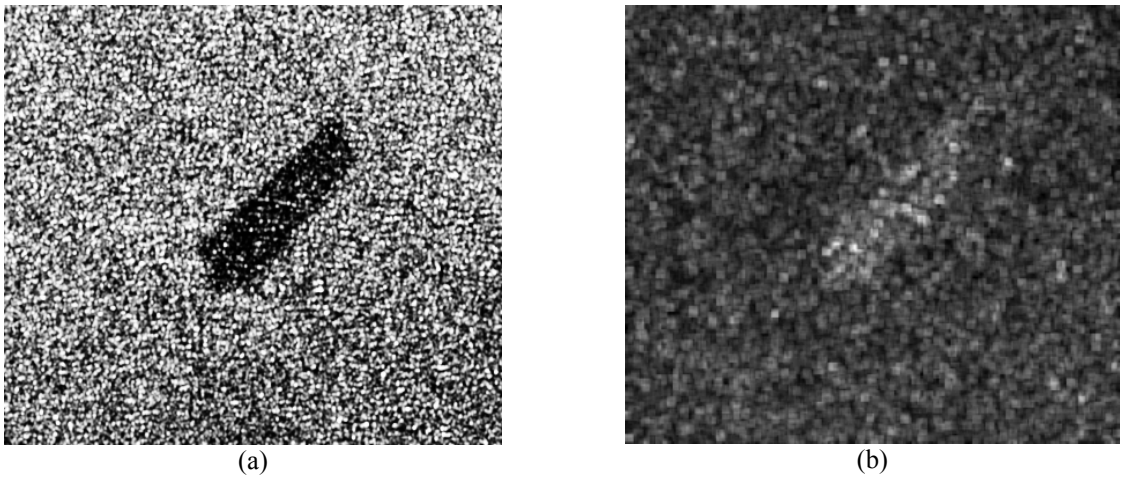

(a) (b)

Fig. 4.11: Total power (a) and standard deviation of the co-polar phase difference (b) relevant to the SIR-C image acquired on 15-04-94 at 02:14 in which a biogenic film (OLA) is present.

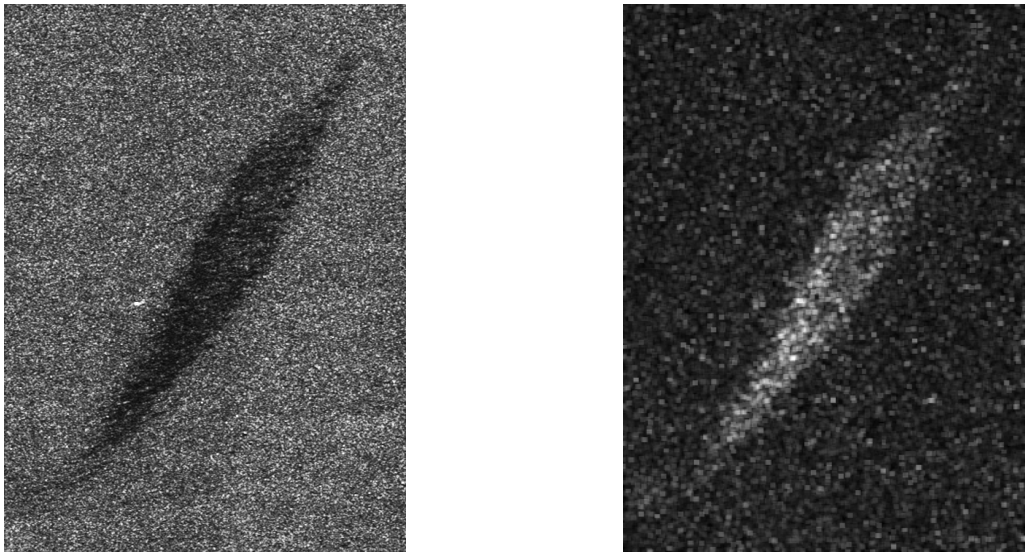

(a) (b)

Fig. 4.12: Total power (a) and standard deviation of the co-polar phase difference (b) relevant to the SIR-C image acquired on 08-10-94 at 05:57 in which an oil spill is present.

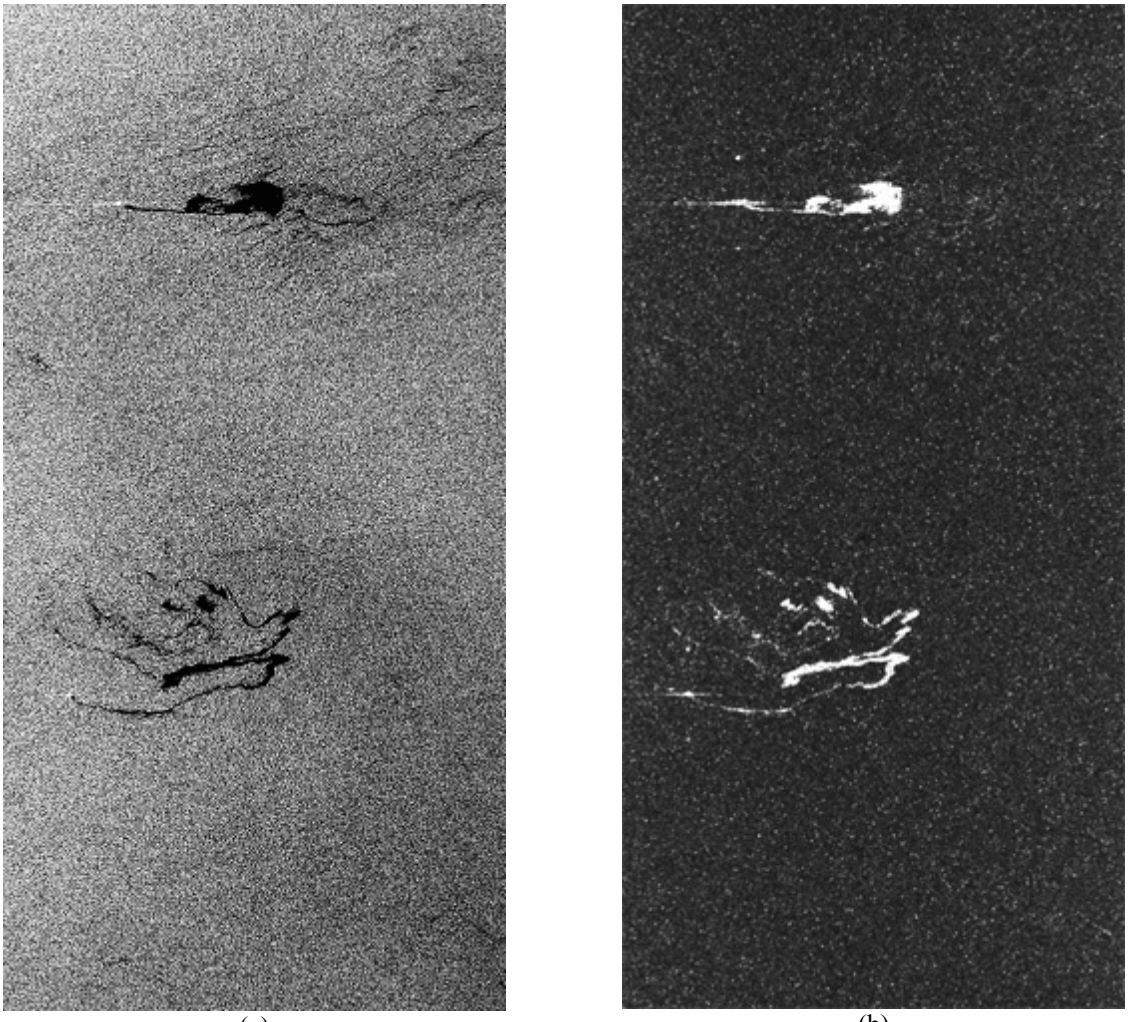

(a) (b)

Fig. 4.13:. Total power (a) and standard deviation of the co-polar phase difference (b) relevant to the SIR-C image acquired on 01-10-94 at 05:33 in which two oil spills are present.

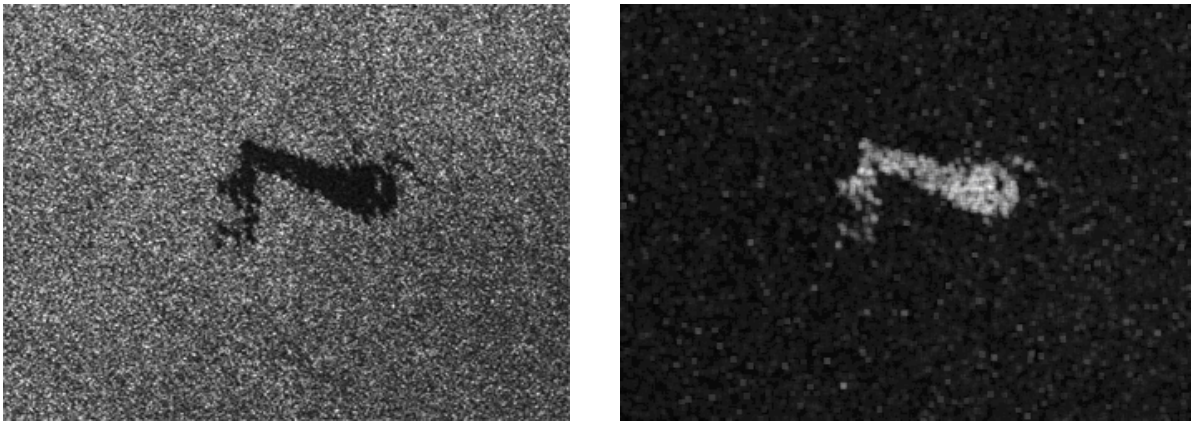

(a) (b)

Fig. 4.14: Total power (a) and standard deviation of the co-polar phase difference (b) relevant to the SIR-C image acquired on 01-10-94 at 08:14 in which an oil spill is present.

In summary, the filtering technique, based on the standard deviation of the co-polar phase difference, allows to distinguish among oil spills and biogenic look-alikes both in low and moderate wind conditions. In detail, the $\sigma_{\varphi c}$ values are larger within the oil spills than the free-sea surface while are comparable within the look-alikes.

References

Brekke C. and A. H. S. Solberg, "Oil Spill Detection by Satellite Remote Sensing," *Remote Sens. Environ*., no.95, pp.1-13, 2005.

Cloude S. R., "Group Theory and Polarization Algebra," *OPTIK*, vol. 75, no.1, pp. 26-36, 1986.

Cloude S. R. and E. Pottier, "A review of target decomposition theorems in radar polarimetry," *IEEE Trans. Geosci. Remote Sensing*, vol. 34, no.2, pp. 498-518, March 1996.

Conradsen K., A. A. Nielsen, J. Schou, and H. Skriver, "A test statistic in the complex Wishart distribution and its application to change detection in polarimetric SAR data," *IEEE Trans. Geosci. Remote Sensing*, vol. 41, no. 1, pp. 4-19, Jan. 2003.

Espedal H. A. and T. Wahl, "Satellite SAR Oil Spill Detection Using Wind History Information," *Int. J. Remote Sensing*, , vol. 20, no. 1, pp. 49-65, Jan. 1999.

Fortuny-Guasch J., "Improved oil slick detection and classification with polarimetric SAR," in *Proc. POLinSAR 2003*, ESA-ESRIN Frascati, Italy, 14-16 January 2003.

Franceschetti G. and R. Lanari, S*ynthetic Aperture Radar Processing*. Boca Raton, FL: CRC Press, 1999.

Freeman A., "SAR calibration: an overview," *IEEE Trans. Geosci. Remote Sensing*, vol. 30, no. 6, pp. 1107-1121, Nov. 1992.

Freeman A., M. Alves, B. Chapman, J. Cruz, Y. Kim, S. Shaffer, J. Sun, E. Turner, and K. Sarabandi, "SIR-C data quality and calibration results," *IEEE Trans. Geosci. Remote Sensing*, vol. 33, no. 4, pp. 848-857, July 1995.

Fukuyama A. K., G. Shigenaka, and G. R. VanBlaricom, "Oil Spill Impacts and the Biological Basis for Response Guidance: an Applied Synthesis of Research on Tree Subartic Intertidal Communities", *NOAA Tech. Memorandum NOS ORCA 125*, Seattle, Washington, March 1998.

Gade M., W. Alpers, H. Huhnerfuss, H. Masuko, and T. Kobayashi, "Imaging of biogenic and anthropogenic ocean surface films by the multifrequency/multipolarization SIR-C/X-SAR," *J. Geophys. Res.*, vol. 103, no. C9, pp. 18851- 18866, Aug. 1998.

Hajnsek I., E. Pottier, S. R. Cloude, "Inversion of Surface Parameters form Polarimetric SAR," *IEEE Trans. on Geosci. and Remote Sensing*, vol. 41, no. 4, pp. 727- 744, April 2003.

Horstmann J., Helmut Schiller, Johannes Schulz-Stellenfleth, and Susanne Lehner, "Global Wind Speed Retrieval From SAR," *IEEE Trans. Geosci. Remote Sensing*, vol. 41, no. 10, pp. 2277–2286, Oct. 2003.

Joughin I. R., D. P. Winebrenner, and D. B. Percival, "Probability Density Functions for Multilook Polarimetric Signatures," *IEEE Trans. on Geosci. and Remote Sensing*, vol.32, no.3, pp.562-574, 1994.

Kinchin A. I., *Mathematical Foundations of Information Theory*. New York, NY: Dover, 1957.

Lee J.-S., K. W. Hoppel, S. A. Mango, and A. R. Miller, "Intensity and Phase Statistics of Multilook Polarimetric and Interferometric SAR Imagery," *IEEE Trans. on Geosci. and Remote Sensing*, vol.32, no.5, pp.1017-1028, 1994.

Lombardo P. and C. J. Oliver, "Optimum detection and segmentation of oil-slicks with polarimetric SAR data," in *The Record of the IEEE 2000 International Radar Conference*, 7-12 May 2000, pp. 122-127.

Mattia F.; T.Le Toan, J.-C.Souyris, C.De Carolis, N. Floury, F. Posa, and N. G. Pasquariello, "The Effect of Surface Roughness on Multifrequency Polarimetric SAR Data," *IEEE Trans. on Geosci. and Remote Sensing*, vol.35, no.4, pp.954-966. 1997.

Migliaccio M., M. Tranfaglia, and S. A. Ermakov, "A Physical Approach for the Observation of Oil Spills in SAR Images," *IEEE J. Oceanic Eng.,* in press.

Ogilvy J.A., *Theory of Wave Scattering from Random Rough Surfaces*, IOP Publushing: Bristol, UK, 1991.

Sarabandi K., L. E. Pierce, M. C. Dobson, F. T. Ulaby, J. M. Stles, T. C. Chiu, R. De Roo, R. Hartikka, A. Zambetti, and A. Freeman, "Polarimetric calibration of SIR-C using point and distributed targets," *IEEE Trans. Geosci. Remote Sensing*, vol. 33, no. 4, pp. 858-866, July 1995.

Schou J., H. Skriver, K. Conradsen, and A. A. Nielsen, "CFAR edge detector for polarimetric SAR images," *IEEE Trans. Geosci. Remote Sensing*, vol. 34, no. 2, pp. 20-32, Jan. 2003.

Schuler D.L., J.S. Lee, D. Kasilingam, and Giuseppe Nesti, "Surface roughness and slope measurements using polarimetric SAR data," *IEEE Trans. on Geosci. and Remote Sensing*, vol. 40, no. 3, pp. 687-698, March 2002.

Schuler D.L., Lee J.S., Kasilingam D., and Pottier E., "Measurements of Ocean Wave Spectra using Polarimetric SAR," *Proc. Int. Geosci. And Remote Sensing Symposium* (IGARSS), Tolouse, France, 21-25 July 2003

Schuler D., J-S Lee, and G. De Grandi, "Spiral Eddy Detection using Surfactant Slick Patterns and Polarimetric Decomposition Techniques," *Proc. Int. Geosci. and Remote Sensing Symposium* (IGARSS), Anchorage, Alaska, 20-24 September 2004.

Schuler D.L. and J.S. Lee, "Mapping Ocean Surface Features using Biogenic Slick-Fields and Polarimetric Decomposition Techniques," *IEE Proc. Radar, Sonar and Navigation*, vol. 153, no. 3, pp. 260-270, 2006.

Solberg A. H. S., G. Storvik, R. Solberg, and E. Volden, "Automatic detection of oil spills in ERS SAR images," *IEEE Trans. Geosci. Remote Sensing*, vol. 37, no. 4, pp. 1916-1924, July 1999.

Touzi R., A. Lopès, and P. Bousquet, "A statistical and geometrical edge detector for SAR images," *IEEE Trans. Geosci. Remote Sensing*, vol. 26, no. 6, pp. 764–773, Nov. 1988.

Ulaby F.T., D. Held, and M. C. Dobson, "Relating Polarization Phase Difference of SAR Signals to Scene Properties," *IEEE Trans. on Geosci. and Remote Sensing*, vol. GE-25, no. 1, 1987.

Ulaby F.T., K. Sarabandi, and A. Nashashibi, "Statistical Properties of the Muller Matrix of Distributed Targets," *IEE Proceedings-F*, vol. 139, no. 2, 1992.

Van Zyl J. J., C. H. Papas and C. Elachi, "On the Optimum Polarization of Incoherently Reflected Waves," *IEEE Trans. Antennas Propagat.*, vol. 35, pp. 818-825, July 1987.

Internet Sites:

[Int.4.1] http://southport.jpl.nasa.gov./

Chapter 5: Feature Analysis and One-Class Pattern Classification

A new approach to perform oil spill detection from SAR images is presented. The approach deals with two issues. The first issue is related to the choice of features used to classify the dark patches obtained from the segmentation of the SAR image. A large number of candidate features that have been proposed in the literature are considered, and a feature selection algorithms to objectively select the most effective subset of features is performed. In particular, four different feature selection techniques are considered, and the results of the four algorithms are successively combined to select the subset of features. The second issue is related to the formulation of the classification problem. While classification is usually formulated as a two-class classification problem, i.e. oil spills vs. look-alikes, a one-class classification approach is here proposed, where classifiers and trained over one class only, i.e. oil spills. Performances have been assessed using a dataset extracted from a set of SAR images acquired by an airborne X band SAR system mounted on board of a Laerjet 35A, during the Galitia Mission in January-February 2003 (TELAER Consortium), after the sinking of the Prestige oil tanker. Results show that new objective feature selection analysis is able to find the most appropriate features and the one-class classification approach is to be preferred.

5.1 Introduction

A large number of semi-automatic oil spill detection procedures based on SAR images have been presented in literature (Espedal and Wahl, 1999; Kubat *et al.*, 1998; Solberg *et al.*, 1999; Del Frate *et al.*, 2000; Fiscella *et al.*, 2000; Marghany, 2001; Girard-Ardhuin *et al.*, 2005; Keramitsloglou *et al.*, 2006; Topouzelis *et al.*, 2003; Stathakis *et al.*,2006). These oil slicks detection techniques are called "semi-automatic" since a key role is played by a human expert who selects the SAR image area to be processed, and assists the interpretation phase. Human expertise allows discriminating between oil slicks and look-alikes by taking into account the location and shape of dark patches, the weather conditions, and the contrast between dark patches and the surrounding sea. Such aspects have to be incorporated into an automatic classification system in which candidate oil slicks are automatically identified and presented for manual inspection. As a consequence, a large number of images can be processed, and the effort required to human operators is reduced. All the semi-automatic techniques for oil spill detection exhibit a percentage of correct classification of oil spills ranging from 81% to 94%. It must be noted that reported results cannot be compared because they are related to different data sets, different segmentation approaches, and different feature extraction processes. It must be noted however that direct comparison of different techniques is not all straightforward since very different SAR data sets are used.

The analysis of the state-of-the-art clearly emphasizes two aspects: i) an undefined number of features are used to perform classification of dark patches as oil spill or look-alikes, and ii) classification of dark patches is always formulated in terms of a two-class classification problems, where examples of the two classes, i.e. oil spills and look-alikes, have to be provided to train the classification model.

In this chapter, the two above aspects are addressed. As far as the feature extraction phase is concerned, is here proposed a feature selection technique aimed at objectively selecting the most effective subset of features from a larger set made up of all the candidate feature that have been proposed in the literature. In addition, the oil spill classification problem is formulated as a one-class classification problem (Tax, 2001). One-class approaches are suited for those problems where reliable examples can be provided for one of the classes. In the case of the oil spill detection problem, it is easy to see that the so-called "look-alike" class is in fact made up of patterns originating from different phenomena. Thus the term "look-alike" does not denote a class of homogeneous patterns, but it is related to all dark patches that are not

related to oil spills. As a consequence, the problem can be formulated as the one of assessing if a dark patch is an oil spill or not. Oil spill examples are used to train one-class classifiers, so that a dark patch is classified as an oil spill if it fits the model, otherwise it is classified as a look-alike.

5.2 State-of-Art

In this section, the related works on feature extraction and classification in the field of oil spill detection are briefly summarized.

In (Espedal and Wahl, 1999) an algorithm for slick discrimination based on direct analysis of the SAR image (shape, size, dB-values, gradients and texture of the slick), contextual analysis (meteorological data, currents, bathymetry, platform, natural seepage, and ship lane locations), and an indirect analysis (a numerical oil drift model, and an ocean model) has been developed. Great emphasis in given to the use of wind history during the days before SAR imaging in the classification process. Three case studies are shown. No qualitative information about classification accuracy is given.

In (Kubat *et al.*, 1998) a neural network is used for the classification of dark regions detected in SAR images. All the issues related to oil spill observation, such as problem formulation, selection of evaluation measures, and performances analysis are illustrated in detail. An unspecified set of features is considered. A series of nine SAR images (141 oil spills) is used to train and test the system and the overall performance on oil spill detection is 81%.

In (1998; Solberg *et al*., 1999) an adaptive image thresholding is combined with a multi-scale pyramid approach and a clustering step to separate the oil spill from its surroundings. Classification is automatically performed, and the output is the probability of a dark area of being an oil spill. This probability is estimated by a multivariate Gaussian density function. The algorithm is combined with a prior model for the number of look-alikes, a model for the presence of slick near a bright object, and a rule-based modification of the probability density function to take into account feature combinations indicating particular scene conditions. Ten different object characteristics are identified. The leave-one-out method with 84 scenes (71 oil spills) gave a correct classification of 94% for oil spills.

In (Del Frate *et al.*, 2000) a neural network for semi-automatic detection of oil spills on SAR images, using a set of feature vectors as input is developed. A processing and analysis tool based on edge detection is applied. Once defined the region of interest (ROI) by the user, an approach based on multilayer perceptrons (MLP) neural network with two hidden layers is considered for classification. The net is trained using the back-propagation algorithm to minimize the error function, and tested on ERS-SAR images. Using the leave-one-out method with 139 oil spills, the 82% of oil spills were correctly classified.

In (Fiscella *et al.*, 2000) a stochastic classifier based on Mahalanobis statistical tests and classical compound probabilities is developed. Dark areas are automatically located, then a Mahalanobis classifier is applied on a fourteen dimensional feature vector, and the probability of a dark spot being an oil spill is estimated. The 82% of the oil spills in the test set were correctly classified by this classifier. This result was compared with a compound probability classifier, where the 91% of the oil spills in the test set were correctly classified. A training set of 80 oil spills and 43 look-alikes and a test set of 11 oil spills, 4 uncertain and 6 look-alike were used.

In (Marghany, 2001). oil slick detection based on texture analysis is used on RADARSAT data. Texture analysis is performed considering the entropy, the energy and the homogeneity values as statistical parameters to distinguish between oil and seawater. The second step involved the use of two types of algorithms, i.e. the Lee and Gamma algorithms. The Lee algorithm is used for identifying homogenous regions, and for edge detection to determine the linearity of oil movements, while the Gamma algorithm is used to determine oil spill spreading. An unspecified number of SAR data is used, and no information about classification performance is given.

In (Girard-Ardhuin *et al.*, 2005) a semi-automatic oil slick detection algorithm is proposed. The backscatter image is first calibrated and transformed into a sea-surface roughness image using an ocean-backscatter model. Then the detection step is based on a multi-scale analysis of the observed data that stresses the different shapes of the sea-surface wave spectrum on clean and polluted water based on a multi-scale method. This method is applied on a three-class problem formulation: oil, non-polluted, and an intermediate state. The classification step is pursued combining the automatically detected slicks with synergistic data, such as surface winds, sea-surface temperature, sea state and surface currents. The methodology is tested on SAR images acquired during the Prestige tanker sinking and two case studies are shown.

Results show that joint SAR and synergistic data are sufficient for oil slick classification, No qualitative information about classification accuracy is given.

In (Keramitsloglou *et al.*, 2006) an automatic procedure for the identification of possible oil spills based on a fuzzy logic classifier is developed. SAR images are land masked, filtered and thresholded so that the appropriate dark areas are extracted. Dark areas are characterized by the total number of objects identified in the image, the number of the dark objects in the vicinity of a candidate dark object, the area of the candidate dark object, the eccentricity of the object's shape and the proximity of the object to the land. Candidate oil spill objects are fuzzy classified to determine the likeness of each individual object to be an oil spill. The output consists of images and tables providing relevant information for supporting decision-making. The procedure was trained using nine SAR images and was tested independently on 26 images of the Aegean Sea, yielding an overall performance of 88%.

In (Topouzelis *et al.*, 2003) an oil spill detection method was developed based on a multi-scale segmentation technique which also creates hierarchical and neighbor relations, and a knowledge base based on oil spill features. The structured objects resulted from segmentation and speckle removal filters are then classified in "calm" (dark areas) and "rough" using a local contrast threshold, which takes into account the sea state and the results from statistical measurements of the intensity image. Each segment classified as "calm" is considered as a possible oil spill, and consequently a set of features is calculated. "Calm" objects are classified as oil spill or look-alike through a hierarchical network, which simultaneously presents the features of the objects, and fuzzy rules for classification. In this study, the features used were evaluated too. The method was tested on 141 dark areas yielding an overall performance of 82%. Texture features showed to be the most useful for classification.

In (Stathakis *et al.*,2006) a feature selection method that concurrently searches for the best feature combinations is presented. The approach is based on optimization via a genetic algorithm. The neural network, selected as the classifier, is a standard fully connected feed-forward multi-layer perceptron trained by the back-propagation algorithm. The genetic algorithm is considered to identify the best hidden layer topology too. A dataset of 24 ERS-2 full resolution SAR images, containing 90 look-alikes and 69 oil spills, is used. A set of nine features has been identified, and the classification accuracy obtained by the neural network considering this set of features was 84.8%.

In summary, although no direct comparison can be made since very different data sets are used, it can be said that an oil spill classification technique can be considered effective if the classification accuracy is at least 81%.

5.3 Features Selection

The first step in oil spill detection is the segmentation of the image in order to identify dark patches, i.e. areas that are candidate to be related to oil spills. Once a dark patch is detected, a set of features related to the dark object and its surrounding areas is computed to classify the object as an oil spill or a look-alike. The present state-of-art suggests to use features belonging to the following four classes (see Table 5.I):

- *Geometry and shape of segmented regions*. If the dark patch is a fresh oil spill released from a moving ship, an important feature is the elongatedness, which can be expressed as a ratio between the width and the length of the slick. Among the shape features, the perimeter and the area of the object are also considered.
- *Backscatter level of the spot and its surrounding*. These features are related to the gradient of the backscattering value from the background to the slick. They provided valuable information when classification by means of neural networks was used (Del Frate *et al.*, 2000). Due to the heavy effect of wind speed, the background standard deviation was also shown to be an important parameter, such as the features related to the background area surrounding the slick (Solberg *et al*., 1999; Del Frate *et al.*, 2000; Fiscella *et al.*, 2000).
- *Spot contextual features*. Spot contextual features depends on weather conditions at the moment of image acquisition (e.g., the wind speed), and on the distance from possible oil spill sources as ships or oilrigs (Migliaccio *et al.*, 2005; Espedal and Wahl, 1999; Solberg *et al*., 1999; Girard-Ardhuin *et al.*, 2005).
- *Texture.* If the pixel intensity is compared to the backscattered signal, textures provide information about the spatial correlation among neighboring pixels (Topouzelis *et al.*, 2003).

TABLE 5.I
FEATURES CONSIDERED IN OIL SPILL DETECTION PROCEDURES.

1.	Area (A)	17.	Max Slick Value
2.	Perimeter (P)	18.	Shape Index
3.	Inside Slick Radar Backscattering (μ_{obj})	19.	Compactness
4.	Inside Slick Standard Deviation (σ_{obj})	20.	Elliptic Fit
5.	Outside Slick Radar Backscattering (μ_{sce})	21.	Length of Main Line
6.	Outside Slick Standard Deviation (σ_{sce})	22.	Width
7.	Complexity ($C = P/2\sqrt{\alpha A}$)	23.	Length/Width
8.	Asymmetry	24.	Curvature Length
9.	Intensity Ratio (μ_{obj} / μ_{sce})	25.	St. Dev. Curvature
10.	Intensity St. Dev. Ratio ($\sigma_{obj} / \sigma_{sce}$)	26.	(GLCM) Homogeneity
11.	ISRI (μ_{obj} / σ_{obj})	27.	(GLCM) Contrast
12.	ISRO (μ_{sce} / σ_{sce})	28.	(GLCM) Dissimilarity
13.	ISRI/ISRO	29.	(GLCM) Entropy
14.	Max Contrast (μ_{sce} – min slick value)	30.	(GLCM) Mean
15.	Mean Contrast ($\mu_{sce} - \mu_{obj}$)	31.	(GLCM) St. Dev.
16.	Min Slick Value	32.	(GLCM) Correlation

μ_{obj}: dark patch mean value; μ_{sce}: scene mean value; σ_{obj}: dark patch std. dev.; σ_{sce}: scene patch std. dev.; (GLCM): grey level co-occurrence matrix.

5.3.1 Motivation for Features Selection

The performance of a classifier depends on the interrelationship between number of samples, number of features, and classifier complexity (Fukunaga, 1990; Duda *et al.*, 2001; Jain *et al.*, 2000). It is well-known that the probability of misclassification of a decision rule does not increase as the number of features increases, as long as the class-conditional densities are completely known (or, equivalently, the number of training samples is arbitrarily large and representative of the underlying densities). However, it has been often experienced that adding new features may degrade the performance of a classifier if the number of considered training samples is small with respect to the number of features. This phenomenon is known as the curse of dimensionality (Jain *et al.*, 2000). All the commonly used classifiers can suffer from the curse of dimensionality. In fact, an exact relationship between the probability of misclassification, the number of training samples, the number of features and the true parameters of the class-conditional densities is very difficult to be established. However, some guidelines have been suggested regarding the ratio of the sample size to the dimensionality. It is generally accepted that using at least ten times as many training samples per class as the number of features $n/d>10$, is a good practice to follow in classifier design. Accordingly, the more complex the classifier, the larger should be the ratio of sample size to dimensionality to avoid the curse of dimensionality. There are two main reasons to keep the

dimensionality of the number of features as small as possible: measurement cost and classification accuracy. A limited but qualitative feature set simplifies both the pattern representation and the classifiers implementation. Consequently, the resulting classifier will be faster and effective. Moreover, a small number of features can alleviate the curse of dimensionality especially if the number of training samples is limited. On the other hand, a reduction in the number of features may lead to a loss in the discrimination capability, and thereby decrease the accuracy of the system. In summary, the problem of feature selection can be defined as follows: given a set of d features, a subset of $m<d$ features that leads to the smallest classification error, has to be selected.

In the context of the oil spill detection problem, the use of all the 32 features shown in Table 5.I, is not a feasible proposition. In fact, the features do not have the same discrimination power and, typically, in these problems the number of training samples is very small. A simple approach of selecting just the best individual features may fail dramatically. It might be useful to consider those methods that take into account both the individual class-separation capability, and the dependencies between the features. To the best of our knowledge, this issue has not been addressed yet in the oil spill detection literature, except for seminal approach in (Stathakis *et al.*, 2006). In this paper an approach to perform a qualitative feature analysis, and an objective selection of the features is proposed.

5.3.2 Features Selection

The approach here developed to perform features selection is based on a combined use of four selection algorithms adopted in literature, namely the Forward method, the Backward method, the Branch & Bound method, and the Best Individual method (Jain *et al.*, 2000). It is worth noting that feature selection should be performed on a data set made up of examples of both classes, i.e. oil spills, and look-alikes. For each feature selection method, an objective function must be defined to measure its discriminative power. The feature selection process is stopped whether a predefined maximum number of features is selected, or the desired value of the objective function is attained.

The Forward method first considers the most discriminating feature, and then adds, the remaining features once at a time, so that the next added feature is the one that provides the largest improvement in classification performance. In other words, let Y_k be the set of features

at iteration k. Feature x^+ is added at iteration $(k + 1)$ if this addition produces the largest improvement of the objective function $J(\cdot)$, i.e. $J(Y_k + x^+) \geq J(Y_k + x)$ for all $x \neq x^+$.

The Backward method proceeds exactly in opposite way; starting from the full feature set, the feature x^- that results in the smallest decrease of the value of the objective function $J(Y_k - x^-)$ is sequentially removed.

The Branch and Bound method starts from the full feature set and removes features using a depth-first strategy. The use of the depth-first strategy is motivated by the assumption of monotonicity of the objective function, i.e.

$$J(x_{i1}) < J(x_{i1}, x_{i2}) < J(x_{i1}, x_{i2}, x_{i3}) < \ldots < J(x_{i1}, x_{i2}, x_{i3}, \ldots, x_{im}) \quad . \tag{5.1}$$

Even if the monotonicity property does not hold for the most commonly used objective functions, the Branch and Bound technique allows avoiding the exhaustive evaluation of all feature combinations.

The Best Individual method measures the inter-classes discriminative power associated to each feature individually. Thus the discriminative power of a subset of features is measured as the sum of the individual contribution of each feature.

A number of different objective functions can be used to perform feature selection such as leave-one-out nearest neighbor classification accuracy, sum of Euclidean or Mahalanobis distances, etc. It is easy to see that the choice of the selection algorithm, and the choice of the objective function affects the subset of selected features. In order to combine the results attained by different feature selection mechanisms, the following heuristic is proposed. Let k be the total number of features, and m the number of the considered feature selection techniques. For each feature a global score based on the ranking assigned by each of the considered feature selection technique is computed. Let us define the function $rank(f_i, sel_j, r)$ as

$$rank(f_i, sel_j, r) = \begin{cases} 1 & \text{if } f_i \text{ is ranked among the first } r \text{ features by } sel_j \; 1 \leq i \leq k, 1 \leq j \leq m \\ 0 & \text{otherwise} \end{cases} \tag{5.2}$$

Then, a score associated to each feature f_i is computed as:

$$score(f_i, r) = \sum_{j=1}^{m} rank(f_i, sel_j, r) \quad . \tag{5.3}$$

Successively, it is possible to order the features according to this score. It is easy to see that the highest score is assigned to those features that have been ranked among the first *r* features by all the considered selection techniques.

5.4 One-Class Classification

In this section the basic concepts related to the one-class classification approach are provided. The theoretical framework proposed in (Tax, 2001) is followed.

The problem of classification is to assign a new object to one of a set of classes that are known beforehand, the two-class problem being considered as the basic classification problem (Fukunaga, 1990). A two-class problem is formulated as follows. Let $\bar{x}$ be the *d*-dimensional feature vector associated with input objects, and let –1 and +1 be the labels assigned to the two classes ω_1 and ω_2, respectively. A function $f(\bar{x})$ has to be inferred from a training set so that an estimate of the label $y = f(\bar{x})$ is obtained, where $f : \Re^d \rightarrow \{-1,+1\}$. It is easy to see that two-class classification techniques need a training set made up of objects belonging to both data classes. In our case, the two classes are oil spills and look-alikes.

The one-class classification problem, a.k.a. outlier detection problem differs in one essential aspect from a conventional multi-class classification problem, as only examples of one class, i.e. the target class, are assumed to be available (Tax, 2001). This means that just example objects of the target class have to be used for training the classifier, and that no information about the other class of objects, i.e. the outlier class, is requested. The task is to define a model of the target class, such that it accepts as much of the target objects as possible, while it minimizes the chance of accepting outlier objects. In one-class classification problems, the target class is assumed to be well sampled, i.e. a large number of training examples are available or this class can be more easily modeled. On the other hand, outliers can be sampled very sparsely, or examples can be totally absent. In our case, the oil spills are considered as the target class, as their characteristics have been thoroughly studied, and they

can be easily reproduced in laboratory simulations. On the other hand, look-alikes are considered to be outliers, as they can be originated by a large variety of different natural phenomena, and thus they can be grouped into an undefined number of classes. In other words, look-alikes are better defined as dark objects that are not oil spills rather than a single one class characterized by common characteristics. Hence, only examples of the target class are used for training the classifier. It is worth noting that in the proposed approach for oil spill detection the available information from known outliers is used in i) the feature extraction process, and ii) the feature selection process, while it is not used for classifier training.

The one-class classification approach can be formulated as the one of fitting a mathematical model on examples from the target class, so that large numbers of target objects are accepted, while the chance of accepting outlier objects is minimized. According to (Tax, 2001), two distinct elements can be identified in all one-class classification methods. The first element is a measure of distance $d(\bar{x})$ or resemblance $p(\bar{x})$ of an object $\bar{x}$ to the target class (represented by a training set χ^{tr}). The second element is a threshold value θ related to this distance or resemblance, so that new objects are assigned to the target class if the distance to the target class is smaller than the threshold θ_d:

$$f(\bar{x}) = I(d(\bar{x}) < \theta_d) \quad , \tag{5.4}$$

or if the resemblance is larger than the threshold θ_p:

$$f(\bar{x}) = I(p(\bar{x}) < \theta_p) \quad , \tag{5.5}$$

where I is the indicator function

$$I(A) = \begin{cases} 1 \text{ if } A \text{ is true} \\ 0 \text{ otherwise} \end{cases} \quad . \tag{5.6}$$

One-class classification methods differ in the definition of $p(\bar{x})$ (or $d(\bar{x})$), in the optimization of $p(\bar{x})$ (or $d(\bar{x})$), and the choice of the threshold θ with respect to the training

set χ^{tr}. In most one-class classification methods the focus is on the optimization of the resemblance model p or distance d. The optimization of the threshold is done afterwards. Only a few one-class classification methods optimize their model $p(\bar{x})$ or $d(\bar{x})$ to an a priori defined threshold. One-class classification techniques can be roughly subdivided into three categories according to the model used to represent the target class: density methods, boundary methods, and reconstruction methods. In this study, we used a number of methods from the first two categories that proved to perform well in a number of applications (Tax, 2001). The list of classifiers with a brief description is reported in the Appendix 5.A.

The most important measure that is typically used to assess the performance of one-class classifiers is the trade-off between the fraction of the target class that is accepted f_{T+}, and the fraction of outliers that is rejected, f_{O-}.

5.5 Experimental Results

The experiments are based on SAR images acquired by Telaer consortium during the Galicia mission conducted in January-February 2003 after the Prestige oil tanker sinking, off the Galicia coasts, Spain (Telaer Data Analysis Report, 2003). The dataset has been extracted from a set of more than 40 images acquired by an airborne X band SAR system mounted on board of a Laerjet 35A. Note that full resolution SAR images are characterized by sub-meter linear resolutions (Telaer Data Analysis Report, 2003). The dataset is made up of 16 oil spills and 40 look-alikes.

Oil spills are characterized by low backscattering levels, thus suggesting the use of thresholding for dark spot segmentation. The adopted segmentation process is a bottom up region-merging technique starting with one-pixel objects. In subsequent steps, smaller image objects are merged into bigger ones. In each step, a pair of adjacent image objects is merged, so that the heterogeneity level of the new object is below a fixed heterogeneity threshold. Throughout this pair-wise clustering process, the underlying optimization procedure minimizes the heterogeneity of the resulting image objects. The process stops if the heterogeneity level of the merged regions exceeds the heterogeneity threshold defined by the human operator. The human operator can either accept the result suggested by the automatic procedure or reject it and produce a new segmented image, by changing the threshold

manually. Once the edges of the dark objects are accepted, all the features, reported in Table 5.I are computed.

Features used in oil spill classification procedures have been analyzed and quantitatively ranked in function of their effectiveness. The selection technique is based on the use of the four features selection techniques outlined in paragraph *5.3.2*. The objective functions used to perform feature selection are those provided in (Duin *et al.*, 2004), namely the leave-one-out nearest neighbor classification accuracy, the sum of Euclidean or Mahalanobis distances, and the inter/intra distance (this is a distance based on the within and between scatter matrixes, which takes into account the distances between patterns of different classes, and the distances between patterns of the same class).

The best features have been used to perform the classification of dark patches by means of two-class and one-class approaches. The dataset has been divided into two parts: a training set to train the classifiers and a test set to evaluate the performances. For the two-class approaches, to avoid problems caused by unbalanced training set, each class is represented by the same number of objects. The performance of the classification methods is evaluated using different number of features, and different training set dimensions.

5.5.1 Features selection

Due to the limited dimension of the data set, a feature space characterized by all the classical features shown in Table 5.I would be unsuitable for the classification phase. To avoid the curse of dimensionality effect a number of at least ten features have to be considered. Hence, an evaluation and a ranking of all these classical features, in function of their discrimination capability between oil spills and look-alikes, have been performed. Each combination of feature selection methods and objective function produced different subsets of "good" features. However, as only the first 20 features have been considered, often the same feature ranking has been produced by different feature selectors. Thus, Table 5.II reports the combination of feature selection methods and objective functions that produced different feature rankings. The selection algorithm counts the times that each feature is ranked in the first five, ten, fifteen and twenty positions, respectively. The four occurrences plots are shown in Figs. 5.1-5.4. These occurrences allowed producing a cumulative ranking matrix that has been used to finally assess the discrimination capability of each feature (see Table 5.III).

TABLE 5.II
SELECTION METHODS AND OBJECTIVE FUNCTIONS
THAT PRODUCED DIFFERENT FEATURE RANKINGS

Selection Method	Distance Criteria
Forward	Sum of Euclidean Distances Nearest Neighbor
Backward	Nearest Neighbor
Branch & Bound	Nearest Neighbor
Individual	Inter-Intra Nearest Neighbor

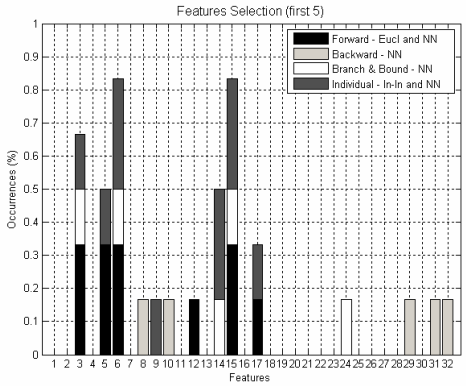

Fig. 5.1: occurrences plots which shows the occurrence that each feature is ranked in the first five by each selection procedure considered. The features with the highest occurrence value are: 6, 15.

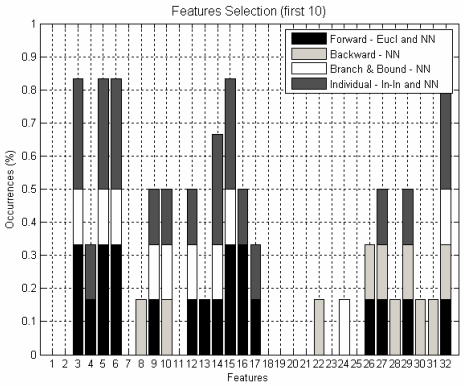

Fig. 5.2: occurrences plots which shows the occurrence that each feature is ranked in the first ten by each selection procedure considered. The features with the highest occurrence value are: 3, 5, 6, 15, 32.

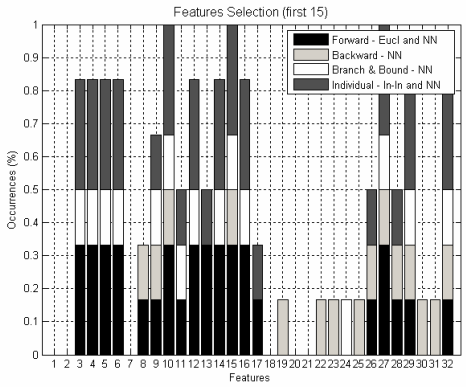

Fig. 5.3: occurrences plots which shows the occurrence that each feature is ranked in the first fifteen by each selection procedure considered. The features with the highest occurrence value are: 10, 15, 27.

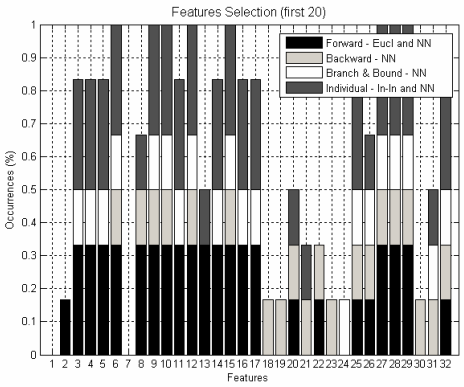

Fig. 5.4: occurrences plots which shows the occurrence that each feature is ranked in the first five by each selection procedure considered. The features with the highest occurrence value are: 6, 9, 10, 12, 15, 27,28, 29.

TABLE 5.III
THE CUMULATIVE RANKING MATRIX

Positions Considered	Good Features										
first 5			6				15				
first 10	3	5	6				15				32
first 15					10		15	27			
first 20			6	9	10	12	15	27	28	29	
Occurrences	*1*	*1*	*3*	*1*	*2*	*1*	*4*	*2*	*1*	*1*	*1*

In this case, the feature selection technique identifies eleven features which are shown in Table 5.IV in function of their discrimination capability. The feature that exhibits the higher discrimination capability is the Mean Contrast, and this result is in accordance with what experienced in (Del Frate *et al.*, 2000). This feature allows highlighting the local backscattering differences among the pixels mean value of the dark patch and the sea surface.

TABLE 5.IV
FEATURES WITH HIGH
DISCRIMINATING CAPABILITY

(15) - Mean Contrast
(6) - Outside Slick Standard Deviation
(10) - Intensity St. Dev. Ratio
(27) - (GLCM) Contrast
(3) - Inside Slick Radar Backscattering
(5) - Outside Slick Radar Backscattering
(9) - Intensity Ratio
(12) - ISRO
(28) - (GLCM) Dissimilarity
(29) - (GLCM) Entropy
(32) - (GLCM) Correlation

The second relevant feature is the Outside Slick Standard Deviation value. This value is greatly influenced by the local wind speed and was already considered in (Del Frate *et al.*, 2000) and (Fiscella *et al.*, 2000). Physically, this result show that to detect an oil spill is necessary a reasonable amount of contrast but this is not sufficient since it can be distinguished by look-alikes only is a tuning on the type of oil and wind is made as experienced in (Migliaccio *et al.*, 2005).

5.5.2 Classification

The performances of one-class classifiers are evaluated and compared to those of two-class classifiers using two experimental setups. One experimental setup is aimed at evaluating the performances when feature vectors of different dimensions are used. Selected features are chosen according to the results reported in the above experiments. The other experimental setup is aimed at evaluating the performances when training set of different sizes are used. These experiments are aimed at evaluating the effects of different features, and those of the size of the training set in oil spill detection. Usually, few training samples are available, while numerous features have been devised.

In the first experiment, once that a 2% maximum acceptable false negative error (i.e., the percentage of oil spills misclassified as look-alikes) has been fixed, the average false positive error (i.e., the percentage of look-alikes misclassified as oil spills) has been evaluated. Three one-class and two-class classification methods (Linear Programming, 1-Nearest Neighbor, and Parzen Windows (Duin *et al.*, 2004; Tax, 2006)) have been used. The average false positive error has been evaluated by considering the first feature listed in Table 5.IV, and then considering, once at a time, all the other eleven features, in the order they have been ranked by the feature selection process. In this case to train the three classifiers, a training set of seven oil spills has been considered for the one-class classifiers, and a training set of seven oil spills and seven look-alikes for the two-class classifiers. To reduce the variance of the estimated error, the average false positive error has been evaluated over one hundred cycles. For each cycle, the elements belonging from the training set and test set was complementary and randomly chosen. In Figs. 5.5-5.6 the plots of the look-alike classification average error for the three one-class and two-class classifiers are shown.

In all cases the look-alike classification average error increase sharply when the third feature (number 10 in Table 5.I) is considered. To evaluate if the ranking position of such a feature may affect the classification error, the Intensity Standard Deviation Ratio feature has been moved to the eleventh position, and the look-alike classification average error has been evaluated for one-class and two-class classifiers (see Figs. 5.7-5.8).

The new features sequence allows improving the classification accuracy, and, at a first analysis, one-class classifiers exhibit a higher classification performance with respect to the performance of two-class classifiers. Moreover, good results are achieved by considering only the first four features of the new sequence; i.e. features 15, 6, 27 and 3.

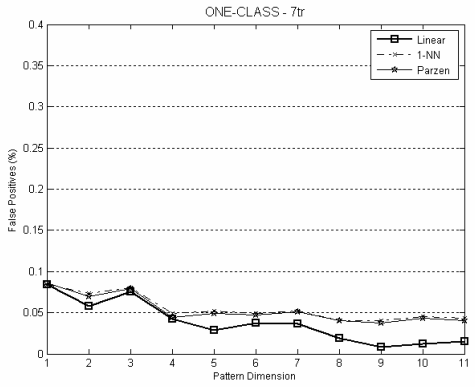

Fig. 5.5: Plot of the look-alike classification average error, once that a 2% oil spill classification max error has been fixed, for three different type of one-class methods. Features considered: 15, 6, 10, 27, 3, 5, 9, 12, 28, 29, 32.

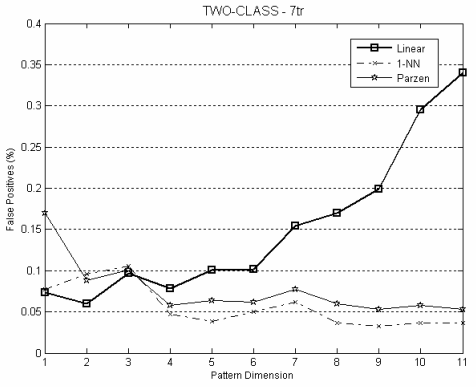

Fig. 5.6: Plot of the look-alike classification average error, once that a 2% oil spill classification max error has been fixed, for three different type of two-class methods. Features considered: 15, 6, 10, 27, 3, 5, 9, 12, 28, 29, 32.

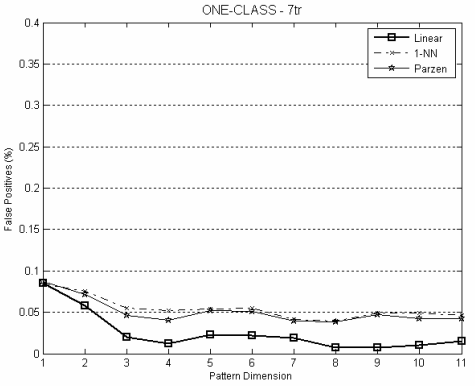

Fig. 5.7: Plot of the look-alike classification average error, once that a 2% oil spill classification max error has been fixed, for three different type of one-class methods. Features considered: 15, 6, 27, 3, 5, 9, 12, 28, 29, 32, 10.

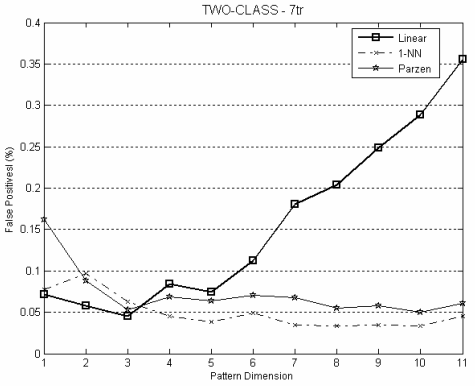

Fig. 5.8: Plot of the look-alike classification average error, once that a 2% oil spill classification max error has been fixed, for three different type of two-class methods. Features considered: 15, 6, 27, 3, 5, 9, 12, 28, 29, 32, 10.

In the second experiment, once that a 2% maximum acceptable false negative error has been fixed the average false positive error has been evaluated by varying the training set dimension. Five classification techniques, both one-class and two-class, namely Linear Programming, 1-Nearest Neighbor, Mixture of Gaussians, Parzen Windows and Support Vectors have been used (Duin *et al.*, 2004; Tax, 2006). Before proceeding further, it is important to note that is expected that classification performance will improve with the increasing of the training set size. Moreover, due to the limited data set available, it is worth noting that to a larger training set will correspond a smaller test set. Since the 2% maximum acceptable false negative error is less representative as the training set size grows, results estimated with a small training set size will be more reliable. Accordingly, results achieved

using a small number of features will be preferred in case of similar results. In this case too, the average false positive error has been evaluated over one hundred cycles. For each cycle, the elements belonging from the training set and test set was complementary and randomly chosen.

In Figs. 5.9 and 5.10 the average error plots of the considered one-class classifiers for different training set dimensions (7, 9, 10, 12), when two feature vector dimensions are considered, namely 4 and 8 features (4D, 8D), are shown. These feature dimensions are relevant according to the new ranking previously achieved.

The best performance is obtained by the simplest classification methods considered (Linear Programming method, 7 training samples, 4D), that exhibits a look-alike classification average error of about 1%. This performance estimation is considered to be more reliable than that provided by other classifier settings which exhibits a smaller look-alike classification average error because of the limited training set size and the limited feature vector dimension. The second best performance is obtained by Support Vectors method using an 8D feature vector dimension, and a training set of 7 (1.7%) and 9 (1%) training samples.

In Figs. 5.11 and 5.12 the average error plots of the considered two-class classification methods for different training set dimensions (7, 9, 10, 12), when two feature vector dimensions are considered, namely 4 and 8 features (4D, 8D), are shown. Two-class classifiers exhibit a worse classification accuracy than that of one-class classifiers. The best performance is obtained by the Support Vector Machine with a look-alike classification average error of about 3%, considering a training set of 7 training samples and a 4D feature vector.

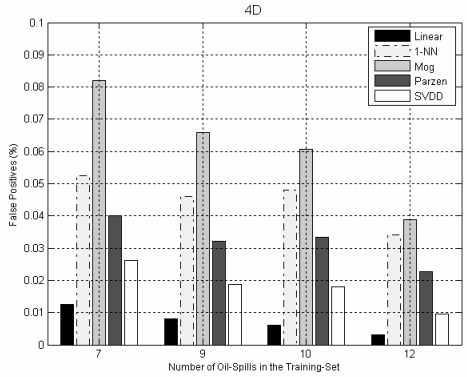

Fig. 5.9: Average error plots of the considered one-class classification methods for different training set dimensions (7tr, 9tr, 10tr, 12tr) and making use of 4 features (4D).

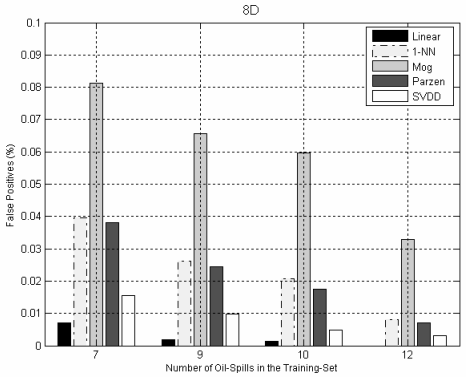

Fig. 5.10: Average error plots of the considered one-class classification methods for different training set dimensions (7tr, 9tr, 10tr, 12tr) and making use of 8 features (8D).

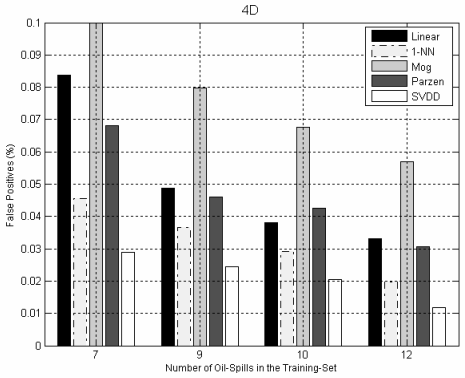

Fig. 5.11: Average error plots of the considered two-class classification methods for different training set dimensions (7tr, 9tr, 10tr, 12tr) and making use of 4 features (4D).

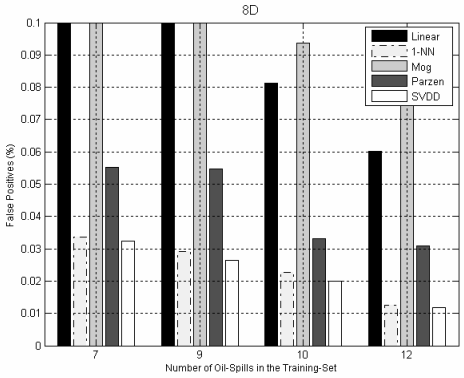

Fig. 5.12: Average error plots of the considered two-class classification methods for different training set dimensions (7tr, 9tr, 10tr, 12tr) and making use of 8 features (8D).

Thus, the reported experiments allows concluding that for a given oil spill detection problem, the more relevant feature should be carefully selected in order to represent dark objects using the minimum number of features with the highest discriminative power and that the one-class approach is effective for oil spill detection as it allows attaining high performances than those of two-class classifiers. In particular, once fixed at 2% the maximum acceptable percentage of oil spills classified as look alike, the percentage of look-alikes classified as oil spills was evaluated. In particular, once fixed at 2% the maximum acceptable percentage of oil spills classified as look alike, the percentage of look-alikes classified as oil spills was evaluated. One-class classifiers allowed attaining an error of 1%, whereas two-class classifiers attained an error of 3%. This behavior could be due to the intrinsic capability of the one-class methods to better adapt to the structure of the data which describe the oil spill features space. The highest accuracies is attained by using either the first four or the first eight best features. These features include the mean contrast between the background and the dark patch, the outside dark patch standard deviation (as the dark patch in the image depends also on the wind speed), the (GLCM) contrast, the inside slick dark patch radar backscattering, the outside slick dark patch radar backscattering, the intensity ratio, the ISRO and the (GLCM) dissimilarity. The best classification performance, for any training set and pattern dimensions, has been achieved with the Linear Programming one–class classifier. The second best classification result has been achieved with the Support Vector one–class classifier. This latter technique provided the best results among those of two-class classifiers. In addition, we also

showed how the performance of one-class and two-class classifiers is affected with different sizes of the training set.

Appendix 5.A: One-class Classification Techniques

Linear Programming data description - This data descriptor is constructed to describe target objects, which are represented in terms of distances to other objects, i.e. the so-called dissimilarity representation (Perlaska and Duin, 2005). The data descriptor can be expressed in the form

$$f(x) = \sum_i \omega_i d(x, x_i) \quad . \tag{5.A.1}$$

A linear programming procedure is employed to optimize the weights so that a few weights are non-zero.

K-Nearest Neighbor data description - In the *k*-Nearest Neighbor data description just the distance to the first *k-th* nearest neighbor is used. Slightly advanced methods use averaged distances, which works somewhat better. This method performs better with high dimensional feature spaces.

Mixture of Gaussian - The target class is modeled using a mixture of *k* Gaussians. The model looks like:

$$f(x) = \sum_{i=1}^{K} P_i \cdot \exp(-(x-\mu_i)^T \Sigma^{-1} (x-\mu_i)) \quad , \tag{5.A.2}$$

where μ_i is the mean value and Σ is the covariance matrix.

The classifier is defined as:

$$f(x) = \begin{cases} \text{target if } f(x) \geq \theta \\ \text{outlier if } f(x) < \theta \end{cases} \quad , \tag{5.A.3}$$

where θ is the threshold value.

Parzen Windows density estimator - An even more flexible density model with a Gaussian model for each one of the training objects. The model looks like:

$$f_{Parzen}(x) = \sum_{i=1}^{N} \exp(-(x - x_i)^T h^{-2} (x - x_i)) \quad . \tag{5.A.4}$$

The free parameter *h* is optimized by maximizing the likelihood on the training set using leave-one-out method. The classifier is defined in the same way of the Mixture of Gaussian case. This method performs better if a reasonable training set is available.

Support Vector data description - It basically fits a hypersphere around the target class. By introducing kernels, this inflexible model becomes much more powerful, and can give excellent results when a suitable kernel is used. It is possible to optimize the method to reject a pre-defined fraction of the target data. That means that for different rejection rates, the shape of the boundary changes.

To start, we define a model which gives a closed boundary around the data: a hypersphere. The sphere is characterized by a center *a* and radius *R* and we demand that the sphere contains all training objects χ^{tr}. When we demand that the sphere contains all training objects χ^{tr} the empirical error is set to 0. The distance from the object *z* to the center of the hypersphere *a* has to be calculated. A test object *z* is accepted when this distance $\|z - a\|$ is smaller than or equal to the radius *R*:

$$f_{SVDD}(z, a, R) = I(\| z - a \|^2 \leq R^2) \tag{5.A.5}$$

where the indicator function *I* is defined as:

$$I(A) = \begin{cases} 1 \text{ if } A \text{ is true} \\ 0 \text{ otherwise} \end{cases} \tag{5.A.6}$$

References

Del Frate F., A. Petrocchi, J. Lichtenegger, and G. Calabresi, "Neural Networks for Oil Spill Detection Using ERS-SAR Data," *IEEE Trans. Geosci. Remote Sens.*, vol. 38, no. 5, pp. 2282-2287, Sept. 2000.

Duda R., P. Hart, and D. Stork, *Pattern Classification*, Second ed., New York, NY: John Wiley & Sons, 2001.

Duin R. P. W., P. Juszczak, P. Paclik, E. Pekalska, D. de Ridder, D.M.J. Tax, *PRTools4A Matlab Toolbox for Pattern Recognition*, Delft University of Technology, The Netherlands, Feb. 2004.

Espedal H. A. and T. Wahl, "Satellite SAR Oil Spill Detection Using Wind History Information," *Int. J. Remote Sens.*, vol. 20, no.1, pp. 49-65, Jan. 1999.

Fiscella B., A. Giancaspro, F. Nirchio, P. Pavese, and P. Trivero, "Oil Spill Detection Using Marine SAR Images," *Int. J. Remote Sens.*, vol. 21, no. 18, pp.3561-3566, Dec. 2000.

Fukunaga K., *Introduction to Statistical Pattern Recognition*, Second ed., San Diego, CA: Academic Press, 1990.

Girard-Ardhuin F., G. Mercier, F. Collard, and R. Garello, "Operational Oil-Slick Characterization by SAR Imagery and Synergistic Data," *IEEE J. Oceanic Engineering*, vol. 30, no. 3, pp. 487-495, July 2005.

Jain A. K., R. P. W. Duin, J. Mao, "Statistical Pattern Recognition: A Review," *IEEE Trans. on Pattern Analysis and Machine Intelligence*, vol. 22, no. 1, pp. 4-37, Jan. 2000.

Keramitsloglou I., C. Cartalis, and C. T. Kiranoudis, "Automatic Identification of Oil Spills on Satellite Images," *Elsevier Environmental Modelling & Software*, vol. 21, no.5, pp. 640-652, May 2006.

Kubat M., R. Holte, and S. Matwin, "Machine Learning for the Detection of Oil Spills in Satellite Radar Images," *Machine Learning*, vol. 30, no. 3, pp. 195-215, June 1998.

Marghany M., "RADARSAT Automatic Algorithms for Detecting Oil Spill Pollution," *Int. J. Appl. Earth Observ. Geoinf.*, vol. 3, no. 2, pp. 191-196, 2001.

Migliaccio M., M. Tranfaglia, and S.A. Ermakov, "A Physical Approach for the Observation of Oil Spills in SAR Images*," IEEE J. Oceanic Engineering*, vol. 30, no. 3, pp. 495-507, July 2005.

Pekalska E. and R. P. W. Duin, *The Dissimilarity Representation for Pattern Recognition, Foundations and Applications*, Singapore: World Scientific Publishing, 2005.

Solberg H. S., G. Storvik, R. Solberg, and E. Volden, "Automatic Detection of Oil Spills in ERS SAR Images," *IEEE Trans. Geosci. Remote Sens.*, vol. 37, no. 4, pp. 1916-1924, July 1999.

Stathakis D., K. Topouzelis, and V. Karathanassi, "Large-scale Feature Selection Using Evolved Neural Networks," in *Proc. of SPIE*, vol. 6365, 2006.

Tax D. M. J., *One Class Classification*, Phd Thesis, Delft University of Technology, The Netherlands, June 2001.

Tax D. M. J., *Data description toolbox - dd tools 1.5.0 - A Matlab toolbox for data description, outlier and novelty detection*, Faculty EWI, Delft University of Technology, The Netherlands, Feb. 2006.

Telaer Data Analysis Report, Telaer Consortium, Feb. 2003.

Topouzelis K., V. Karathanassai, P. Pavlakis, and D. Rokos, "Oil Spill Detection: SAR Multi-Scale Segmentation & Object Features Evaluation," in *Proc. of SPIE*, vol. 4880, pp. 77-87, 2003.

Conclusions

In this thesis work a new approach to observe oil spills by means of remotely sensed measurements has been developed. The new approach is based on the use of multisensor data and physical scattering modeling.

A set of remarkable results have been obtained and they were published in peer-reviewed prominent international journals. They are hereafter summarized.

A new SAR sea surface waves simulator has been conceived, implemented and tested. The simulator, based on the velocity bunching theory, has been developed in Matlab® and uses a Graphic User Interface. It is conceived to be a simple and useful tool to well understand and describe the physical aspects governing the SAR surface waves imaging. Presented numerical simulation allowed showing the usefulness of the simulator as an appropriate tool to assist the comprehension of the SAR sea surface waves imaging process.

The mathematical problem of the oil spill detection has looked for the objective definition of the feature space and of the nature of the classification problem. First, an approach to perform a qualitatively analysis and to objectively select among the classical features,

extracted from SAR images and used in oil spill classification procedures, is proposed. The selection algorithm is based on the use of four selection algorithms considered with different objective functions to produce different rankings of the features according to their discriminative power. In order to combine such different results, the occurrence of each feature in all the selection algorithms is taken into account. The analysis of the occurrences allowed producing a cumulative ranking that has been used to finally assess the discrimination capability of each feature. Successively, the oil spill classification problem is formulated as a one-class classification problem and the best features, identified by the objective analysis, have been used to perform the classification of dark patches by means of two-class and one-class approaches. Several experiments have been carried out to compare the performances of one-class classifiers with respect to the classical two-class classifiers. Performance is evaluated by varying the number of training objects and the number of features. A number of one-class and two-class classification techniques have been used: Linear, 1-Nearest Neighbor, Mixture of Gaussians, Parzen Windows and the Support Vector. Experimental results show that the best classification performance is always achieved by one-class classification techniques.

A new a speckle model for marine Single-Look Complex SAR images has been proposed. This model allowed showing that full-resolution speckled SAR images can be effectively employed to detect dark areas and strong scatterers. Classical approaches, which are not able to process such SAR images, deal with multi-look SAR images where, at the expense of a poorer spatial resolution, the speckle is mitigated. Unfortunately, this hampers the possibility to detect small dark areas and strong scatterers which are anyway very difficult to be identified by means of usual filtering techniques. The new approach is based on the generalized K model which is able to embody very different scattering cases. Therefore, it is possible to take advantage of such SAR full-resolution SAR images and detect even small dark areas and strong scatterers. Experimental results demonstrates that GK parameters are useful and that the approach is simple and effective. As a matter of fact the approach can be envisaged as an additional tool to assist the detection of oil spills.

Finally, two studies on sea oil spills observation by means of polarimetric SAR data are accomplished. In the first approach, which uses full polarimetric data, a CFAR filter appropriately tailored for polarimetric SAR data has been first applied over marine images. It allows limiting the volume of data to be processed for classification. The polarimetric CFAR

filter is able to effectively identify the ROIs, i.e. the dark patches which may be due to oil spills. This is useful to facilitate the estimation of the morphological features associated to the ROIs. Further, it has been studied the relevance of the polarimetric features H, $\hat{\alpha}$ and A to assist oil spill classification. Experiments results showed that the main polarimetric feature is the H both for low and high wind regimes. Such a feature is able to distinguish oil free with oil covered areas and in some cases to distinguish among biogenic and anthropogenic slicks. In the second approach, a filtering technique based on the standard deviation of the co-polar phase difference has been developed and tested. Since the filter needs only HH and VV data, it can be applied also on dual-polarized SAR sensors such as the ASAR operated on board of the ENVISAT mission and the forthcoming CosmoSkyMed mission. Experimental results showed the usefulness of using $\sigma_{\varphi c}$ to assist oil spill detection and, in particular, for distinguishing among oil spills and biogenic look-alikes.

Table of Symbols

x,y	surface coordinates
$z(x,y)$	rough surface
σ^2	surface variance
$C(\cdot)$	autocorrelation function
$\boldsymbol{S}(\cdot)$	power spectrum function
$D(\cdot)$	structure function
$\theta_i \;\; \theta_s \;\; \varphi_s$	Local incidence and scattering angles
$\mathbf{E}(\cdot)$	electric field
$\hat{\mathbf{e}}_{i,s}$	unit vector of the incident, scattered field
ε_r	surface dielectric constant
k	e.m. wave number
$\boldsymbol{k}$	e.m. wave vector
λ	e.m. wave length
K	surface wave number
$\boldsymbol{K}$	surface wave vector
Λ	surface wave length
$w(\cdot,\cdot)$	illumination function
$W(\cdot,\cdot)$	Fourier transform of the illumination function
ς	vacuum intrinsic impedance
$\hat{\mathbf{n}}(\cdot)$	unit vector perpendicular to the surface
ξ, ζ	local slopes in the $\hat{\mathbf{x}}$ and $\hat{\mathbf{y}}$ directions
$\mathbf{F}(\cdot,\cdot)$	dimensionless function depending on the average Fresnel reflection coefficients over the mean plane
$\hat{\mathbf{h}}_l$, $\hat{\mathbf{v}}_l$	unit vectors of the local orthogonal and parallel polarizations
R_h, R_v	Fresnel reflection coefficients
σ^o_{pq}	normalized radar cross section
$\mathcal{A}$	area of the illuminated surface
α_{pq}	modified Fresnel reflection coefficients
$N(\cdot)$	action spectral density function
$Q(\cdot)$	energy input spectra distribution

Q_w	wind term of energy input spectra distribution
Q_{nl}	non-linear wave-wave interaction term of energy input spectra distribution
Q_d	dissipation term of energy input spectra distribution
Q_v	viscous dissipation term of energy input spectra distribution
Q_{br}	wave breaking term of energy input spectra distribution
β	wave growth rate
c_g	group velocity
c_p	phase velocity
$U(z)$	wind speed
χ	damping coefficient
$\overline{\sigma}^o_{pq}$	modulated NRCS
R^{RAR}	real aperture radar modulation transfer function
R^t	R^{RAR} tilt modulation term
R^r	R^{RAR} range bunching modulation term
R^h	R^{RAR} hydrodynamic modulation term
$u_r(\cdot)$	orbital velocity in range direction
$a_r(\cdot)$	acceleration in range direction
$I(\cdot)$	SAR image intensity
ρ_a	azimuthal resolution
$\overline{\rho}_a$	degraded azimuthal resolution
$\mathscr{e}$	degree of non-linearity
$\mathscr{a}$	Weibull scale parameter
$\mathscr{b}$	Weibull shape parameter
α	generalized K shape parameter
η	generalized K shape parameter
ν	generalized K shape parameter
$\mathbf{S}$	scattering matrix
S	element of scattering matrix
$\boldsymbol{k}_L$	lexicographic decomposition of $\mathbf{S}$
$\boldsymbol{k}_P$	Pauli decomposition of $\mathbf{S}$
$\mathbf{C}$	covariance matrix
$\mathbf{T}$	coherence matrix
$\mathbf{M}$	Mueller matrix
H	entropy parameter
$\widehat{\alpha}$	alpha angle parameter
A	anisotropy parameter
$m_{\varphi c}$	mean of the phase difference
$\sigma_{\varphi c}$	standard deviation of the phase difference
T_f	Threshold
P_{fa}	probability of false alarm
ς_W	image homogeneity parameter

Contributes

Attilio Gambardella was born and educated in Italy. He received the Laurea degree (5-year legal course of study) in Nautical Sciences from the Università degli Studi di Napoli Parthenope in 2003 and received the 2003 best Remote Sensing Thesis Award by the IEEE GRS South Italy Chapter.

He is at Università degli Studi di Cagliari, Italy as PhD student in Electronic and Computer Science Engineering. He was recipient of research contract at Engineering School "G. Latmiral" - Università degli Studi di Napoli Parthenope. He has been lecturing at Universitat Politecnica de Catalunya and Università degli Studi di Cagliari.

His main research interests deal with SAR polarimetry, electromagnetic modeling, oil spills SAR monitoring, and microwave radiometry.

Mr. Gambardella is IEEE Student member since 2003. Member of the IEEE Geoscience and Remote Sensing Society since 2003. Member of the IEEE Oceanographic Engineering Society since 2005.

Publication list:

Reviewed Journals

M. Migliaccio, A. Gambardella, M. Tranfaglia, "SAR Polarimetry to Observe Oil Spills," *IEEE Trans. Geosci. Remote Sens.*, vol.43 , no.2 , pp 506-511, 2007.

A. Gambardella, M. Migliaccio "The Truncated Singular Value Decomposition (TSVD) to Ameliorate the Spatial Resolution of Microwave Scanning Radioneters", *Atti della Fondazione "Giorgio Ronchi"*, vol.LXI, no.1, pp 5-17, 2006.

M. Migliaccio, A. Gambardella "Microwave Radiometer Spatial Resolution Enhancement", *IEEE Trans. Geosci. Remote Sens.*, vol.43, no.5, pp 1159-1169, 2005.

A. Gambardella, G. Giacinto, M. Migliaccio, A. Montali, "SAR Oil Spill Detection: Feature Analysis and One-Class Pattern Classification," *IEEE Trans. Geosci. Remote Sens.*, submitted for publication.

F. Nunziata, A. Gambardella, M. Migliaccio, "An Educational SAR Sea Surface Waves Simulator", *Int. J. Remote Sens.*, submitted for publication.

M. Migliaccio, G. Ferrara, A. Gambardella, F. Nunziata, A. Sorrentino, "Detection of Dark Areas and Strong Scatterers in Marine SLC SAR Images", *IEEE J. Oceanic Engineering*, submitted for publication.

Refereed Conferences

A. Gambardella, F. Nunziata, M. Migliaccio, "Oil Spill Observation by means of Co-polar Phase Difference", *Proc. of PolINSAR2007 Workshop*, ESA-ESRIN, Frascati, Italy, January 22-26, 2007.

A. Gambardella, A. Montali, G. Giacinto, M. Migliaccio, "Feature Analysis and Pattern Classification Techniques for Oil Spill Detection in SAR Images", *Proc. of 2006 IEEE GOLD*, Bari, Italy, December 3-4, 2006.

F. Nunziata, A. Gambardella, M. Migliaccio, "OSIS: An Ocean SAR Image Simulator", *Proc. of 2006 IEEE GOLD*, Bari, Italy, December 3-4, 2006.

A Sorrentino, M. Migliaccio, G. Ferrara, A. Gambardella, F. Nunziata, "A Stochastic Model for Detection and Observation of Dark Areas and Strong Scatterers by means of SLC SAR Images", *Proc. of 2006 IEEE GOLD*, Bari, Italy, December 3-4, 2006.

M. Migliaccio, A. Gambardella, F. Nunziata, "Oil Spill Observation by SAR: State of Arts and Future Trends", *Proc. of 9th International Marine Environmental Modelling Seminar - IMEMS2006*, Rio de Janeiro, Brazil, October 9-11, 2006.

F. Nunziata, A. Gambardella, M. Migliaccio, "SISM: Simulatore di Immagini SAR relative al Mare", *Proc. of XVI Riunione Nazionale di Elettromagnetismo*, Genova, Italy, September 18-21, 2006.

F. Nunziata, A. Gambardella, M. Migliaccio, "La Differenza di Fase Co-polare per l'Osservazione degli

Idrocarburi a Mare", *Proc. of XVI Riunione Nazionale di Elettromagnetismo*, Genova, Italy, September 18-21, 2006.

M. Migliaccio, A. Gambardella, F. Nunziata, M. Tranfaglia, "Polarimetric SAR and Oil Spill Observation", *Proc. of US/EU-Baltic Int. Symposium*, Klapeida, Lithuania, May 23-25, 2006.

M. Migliaccio, G. Ferrara, A. Gambardella, F. Nunziata, "A New Stochastic Model for Oil Spill Observation by means of Single-Look SAR Data", *Proc. of US/EU-Baltic Int. Symposium*, Klapeida, Lithuania, May 23-25, 2006.

M. Migliaccio, A. Gambardella, M. Tranfaglia, "Oil Spill Observation by means of Polarimetric SAR data", *Proc. of SEASAR2006 Workshop*, ESA-ESRIN, Frascati, Italy, January 23-26, 2006.

M. Migliaccio, G. Ferrara, A. Gambardella, D. Aiello, "The K-generalized Model to Characterize Marine Features in SAR images: First Results", *Proc. of SEASAR2006 Workshop*, ESA-ESRIN, Frascati, Italy, January 23-26, 2006.

A. Montali, G. Giacinto, M. Migliaccio, A. Gambardella, "Supervised Pattern Classification Techniques for Oil Spill Classification in SAR Images: Preliminary Results", *Proc. of SEASAR2006 Workshop*, ESA-ESRIN, Frascati, Italy, January 23-26, 2006.

M. Migliaccio, A. Gambardella, D. Theis, "Spatial Resolution Enhancement of Microwave Scanning Radiometers Data", *Proc. of IEEE Oceans05Europe Conference*, Brest, France, June 21-25, 2005.

A. Gambardella, M. Migliaccio "Uno Studio sul Miglioramento della Risoluzione Spaziale dei Radiometri a Scansione", *Proc. of XV Riunione Nazionale di Elettromagnetismo*, Cagliari, Italy, September 13-17, 2004.

A.Gambardella, M. Migliaccio "Microwave Scanning Radiometer Spatial Resolution Enhancement", *Proc. of 2004 IEEE GOLD*, Napoli, Italy, May 13-14, 2004.

A. Gambardella, M. Migliaccio "Estimates of Brightness Temperatures From Scanning Radiometer Data by Means of the Backus-Gilbert and TSVD Procedures", *Proc. of 8th Specialist Meeting on Microwave Radiometry and Remote Sensing, Rome*, Italy, February 24-27, 2004.

M. Migliaccio, A. Gambardella "Microwave Radiometer Spatial Resolution Enhancement", *Proc. of Tyrrhenian International Workshop on Remote Sensing*, Elba Island, Italy, Sept. 15-18, 2003.

M. Migliaccio, A. Gambardella "TSVD Spatial Resolution Enhancement of Microwave Radiometer Data: a Sensivity Study", *Proc. of IEEE IGARSS'03*, Toulouse, France, July 21-25, 2003.